Mathematical modelling of interacting fibre structures and non–woven materials

Christian Neßler

I dedicate this work to my beloved wife Katie.

Declaration

I hereby declare that, except where specific reference is made to the work of others, the contents of this dissertation are original and have not been submitted in whole or in part for consideration for any other degree or qualification in this, or any other university. This dissertation is my own work and contains nothing which is the outcome of work done in collaboration with others, except as specified in the text and Acknowledgements.

Christian Neßler

Acknowledgements

I am deeply grateful to my family, both in the UK and in Germany, for their love, support and guidance. I thank my parents–in–law, Robert and Katherine, for their proof–reading. My very special thanks to my brother Sebastian, his wife Julia, and my mother Sigrid, who have always supported, encouraged and believed in me.

Last but not least, I would like to express my deepest appreciation to my wife Katie. She supported me throughout my whole PhD studies, believed in me and motivated me. She was and is always a great source of inspiration.

Abstract

Non–woven materials consist of many thousands of fibres laid down on a conveyor belt under the influence of a turbulent air stream. To improve industrial processes for the production of non–woven materials, we develop and explore novel mathematical fibre and material models.

In Part I of this thesis we improve existing mathematical models describing the fibres on the belt in the meltspinning process. In contrast to existing models, we include the fibre–fibre interaction caused by the fibres' thickness which prevents the intersection of the fibres and, hence, results in a more accurate mathematical description. We start from a microscopic characterisation, where each fibre is described by a stochastic functional differential equation and include the interaction along the whole fibre path, which is described by a delay term. As many fibres are required for the production of a non–woven material, we consider the corresponding mean–field equation, which describes the evolution of the fibre distribution with respect to fibre position and orientation. To analyse the particular case of large turbulences in the air stream, we develop the diffusion approximation which yields a distribution describing the fibre position. Considering the convergence to equilibrium on an analytical level, as well as performing numerical experiments, gives an insight into the influence of the novel interaction term in the equations.

In Part II of this thesis we model the industrial airlay process, which is a production method whereby many short fibres build a three–dimensional non–woven material. We focus on the development of a material model based on original fibre properties, machine data and micro computer tomography. A possible linking of these models to other simulation tools, for example virtual tensile tests, is discussed.

The models and methods presented in this thesis promise to further the field in mathematical modelling and computational simulation of non–woven materials.

Journal articles

The following articles, which were published in peer–reviewed journals, were used in this thesis:

GRAMSCH, S., A. KLAR, G. LEUGERING, N. MARHEINEKE, C. NESSLER, C. STROHMEYER, and R. WEGENER (2016) Aerodynamic web forming: process simulation and material properties in: *Journal of Mathematics in Industry*, **6**:13, 1–23 (see pp. 81, 83, 103, 104, 115)

KLAR, A., C. NESSLER, and C. STROHMEYER (2016) Construction of virtual non-wovens in: *Progress in Industrial Mathematics at ECMI 2014* ed. by G. RUSSO, V. CAPASSO, G. NICOSIA, and V. ROMANO Springer International Publishing (see pp. 81, 115)

Furthermore, the following preprint has been submitted and accepted:

BORSCHE, R., A. KLAR, C. NESSLER, A. ROTH, and O. TSE (submitted) A Retarded Mean-Field Approach for Interacting Fiber Structures in: *SIAM Journal on Multiscale Modeling and Simulation*, http://arxiv.org/abs/1501.06465 (see pp. 51, 54)

Contents

II   Airlay fabrics

Interacting fibres

1 The meltspinning process

In this chapter we give a short introduction to the industrial meltspinning process. In particular, we review existing mathematical models of several different aspects of this process, along with their results. We end by outlining the structure for the remainder of this part. We note that preliminary results of this part were partially presented in Nessler *(2013).*

1.1 The production process

Meltspinning is a method used for the production of non–woven fleece materials, used in numerous industrial settings, for example as filter or insulating materials. During the production the melt, which is stored in a polymer distributor, runs through narrow nozzles. The nozzle forms single fibres which get stretched and tangled due to forces exerted by a turbulent air stream. Finally, the fibres lay down on a belt and build the material structure. Due to the complexity of this production process, different aspects of the process have been separately examined and mathematically modelled. A good overview of the general modelling hierarchy is given in Klar, Marheineke, *et al.* (2009). In Leithäuser and Fessler (2012), Leithäuser, Fessler, and Pinnau (2012), and Leithäuser, Pinnau, *et al.* (accepted) shape optimisation was performed to improve the basin shape and resultant flow geometries to realise a given wall shear stress and thus prevent or reduce stagnant zones. In Marheineke and Wegener (2006) and Marheineke and Wegener (2007) further mathematical models were developed to describe the fibre movement in the air, before hitting the belt, and include several physical effects, for example the influence of a turbulent air stream and gravitation. These complex models describing the fibre movement are computationally expensive and, thus, only a limited number of fibres can be feasibly simulated. However, real materials consist of thousands of fibres. Therefore, surrogate models for the fibre lay down, as in the case of the one we will develop in this thesis, have become essential. These models cover the basic physical effects, but nevertheless are computationally cheap and easy to solve, see Götz *et al.* (2007), Klar, Marheineke, *et al.* (2009), Maringer *et al.* (2010), Klar *et al.* (2012a), and Klar *et al.* (2012b). Using a combination of these mathematical models and numerical simulations it has been possible to improve the production process and the

resulting material, including the material strength (HIETEL *et al.*, 2008). However, further improvements in the production process are possible, and can be aided by an improvement of the mathematical models and the numerical methods used.

1.2 Structure

The remainder of this part is structured as follows. In Chapter 2 we give an overview of existing surrogate fibre models. Then, in Chapter 3, we present a new surrogate model for the fibre lay down which includes the fibre thickness and the resulting fibre interactions. Afterwards, in Chapter 4, we consider macroscopic equations derived from the microscopic interacting fibre model presented in Chapter 3 and analyse the case of many long fibres both analytically and numerically. To conclude, in Chapter 5, we summarise our results and present an outlook on possible future work in this field.

2   Surrogate fibre models

In this chapter we give an overview of existing surrogate models for fibre lay down and their connections. In particular, we focus on the mathematical models that we will use and extend in this thesis. We concentrate on the intuitive microscopic description and also show connections to macroscopic descriptions and known theoretical results when it is meaningful and of interest. We start with the original two–dimensional model by GÖTZ *et al. (2007) and describe extensions to three and arbitrary dimensions (*MARINGER *et al., 2010;* KLAR *et al., 2012a;* MARINGER, *2013). Furthermore, we review smooth extensions of the models (*HERTY *et al., 2009;* KLAR *et al., 2012b).*

2.1   Two–dimensional models

We start by explaining the two–dimensional model by GÖTZ *et al.* (2007), exemplary in all its details, which is the basis for all the other models and results presented in this chapter. We then move on to extensions of the model including belt movement (BONILLA *et al.*, 2007) as well as smooth models (HERTY *et al.*, 2009; KLAR *et al.*, 2012b). This should give the reader an insight into the underlying construction of the model and related fields of interest.

2.1.1   The basic model

The two–dimensional model presented in GÖTZ *et al.* (2007) is the basic surrogate model describing the lay down behaviour of long fibres produced by meltspinning. The main idea of the surrogate model is to describe the resulting image of the fibres on the conveyor belt accurately, but including only basic physical effects. These are the fibre coiling and the influence of the turbulent air stream. The advantage of surrogate models over models aiming to describe complicated physical phenomena is the short simulation time which allows for the numerical simulation of thousands of fibres. Computer simulations based on such surrogate models can yield important information about the homogeneity or weight distribution of the resulting material (KLAR, MARHEINEKE, *et al.*, 2009; BOCK *et al.*, 2014).

In the basic two–dimensional surrogate model by GÖTZ *et al.* (2007) each single fibre is represented as an object without thickness and independent of all the other fibres in the

non–woven material. Thus, any interaction between the fibres is ignored. Each individual fibre is described by its centreline. Mathematically this is an arc–length parametrised curve for the fibre position x with α representing the deviation angle of the fibre orientation from the Euclidean basis vector e_1

$$\begin{aligned} x &: \mathbb{R}_+ \to \mathbb{R}^2, \\ \alpha &: \mathbb{R}_+ \to [0, 2\pi), \end{aligned} \tag{2.1}$$

where

$$\mathbb{R}_+ = \left\{ x \in \mathbb{R} \,\middle|\, x \geq 0 \right\}.$$

Without loss of generality it is assumed that the mathematical origin coincides with the nozzle position and the Euclidean basis vector e_1 with the orientation of the conveyor belt. The Euclidean basis vector e_2 is orthogonal to e_1. The model for the fibre image consists of the following second order stochastic differential equation (SDE)

$$\begin{aligned} \mathrm{d}x_t &= v(\alpha_t)\mathrm{d}t, \\ \mathrm{d}\alpha_t &= \underbrace{-\nabla V(x_t) \cdot v^\perp(\alpha_t)\mathrm{d}t}_{\text{deterministic force}} + \underbrace{A\mathrm{d}W_t}_{\text{stochastic force}}. \end{aligned} \tag{2.2}$$

As the fibre curve described by the evolution of Equation (2.2) is arc–length parametrised, t is the arc–length parameter. The classical interpretation of t in dynamical systems literature is *time*, and so we will also sometimes use this interpretation. With $x_{t,i}$, $i \in \{1,2\}$, we denote the single components of x_t at time t. The orientation vector $v(\alpha)$ in Equation (2.2) is defined as

$$v(\alpha) := (\cos\alpha, \sin\alpha)^T \in \mathbb{S}^1,$$

where $\mathbb{S}^1 \subset \mathbb{R}^2$ denotes the unit circle

$$\mathbb{S}^1 = \left\{ v \in \mathbb{R}^2 \,\middle|\, \|v\|^2 = 1 \right\},$$

and $\|\cdot\|$ denotes the Euclidean norm. By

$$v^\perp(\alpha) = \frac{\mathrm{d}v}{\mathrm{d}\alpha} = (-\sin\alpha, \cos\alpha)^T,$$

we denote the orthonormal unit vector to $v(\alpha)$. Furthermore, $V : \mathbb{R}^2 \to \mathbb{R}$, in Equation (2.2) denotes a function which can be interpreted as an external potential. The standard choice

for V (KLAR, MARHEINEKE, *et al.*, 2009; GÖTZ *et al.*, 2007) is

$$V(x) = \frac{1}{2} \left(\frac{x_1^2}{\sigma_1^2} + \frac{x_2^2}{\sigma_2^2} \right),$$

or in compact form

$$V(x) = \frac{1}{2} x^T \Sigma^{-1} x,$$

where Σ is the covariance matrix of the process

$$\Sigma = \text{diag} \left\{ \sigma_1^2, \sigma_2^2 \right\},$$

and $\sigma_i > 0$, $i = 1, 2$, are the *throwing ranges*. These describe the deviation of the fibre position from the nozzle position. Thus, the term $-\nabla V(x_t) \cdot v^\perp(\alpha_t)$ in Equation (2.2) is responsible for describing an orientation change of the fibre orthogonal to the current fibre orientation. This motion, which is due to the external potential V, is also called *coiling*, and so V is sometimes called the *coiling potential*. If the throwing ranges are small, the fibres are more likely to return back to the origin. Without loss of generality in the following we assume that $\sigma_1 = \sigma_2 = 1$. The parameter $A \in \mathbb{R}_+$ in Equation (2.2) is the *noise amplitude* of the process and mimics, together with the one–dimensional Brownian motion $(W_t)_{t \geq 0}$, the effect of the turbulent airflow on the fibre lay down. The notation used in Equation (2.2) implies Itô integration. For a comprehensive introduction to stochastic differential equations, we refer the reader to ØKSENDAL (2003), GARD (1988), EVANS (2013), and ARNOLD (1973). In addition, the system has to be equipped with initial conditions $(x_0, \alpha_0) \in \mathbb{R}^2 \times [0, 2\pi)$.

We note that the solutions of Equation (2.2) are random variables. Thus, we interpret each realisation of Equation (2.2) as an independent single fibre.

In Figure 2.1 we can see the effect of the noise amplitude A on the fibre curves x with length $t = 100$. Each subplot shows two realisations of fibre curves, one in blue and one in red. Both realisations are based on Equation (2.2) where the difference lies in the choice of the initial conditions. Figure 2.1(a), in particular, shows the deterministic case, $A = 0$, which results in a regular and symmetric fibre structure. As A increases there is a loss of this regularity. When the noise is small, in Figure 2.1(b), the deterministic structure can still be seen, but as A increases further, as shown in Figures 2.1(c) and 2.1(d), it is no longer visible. Overall we see that for increasing values of A the fibre image becomes more chaotic.
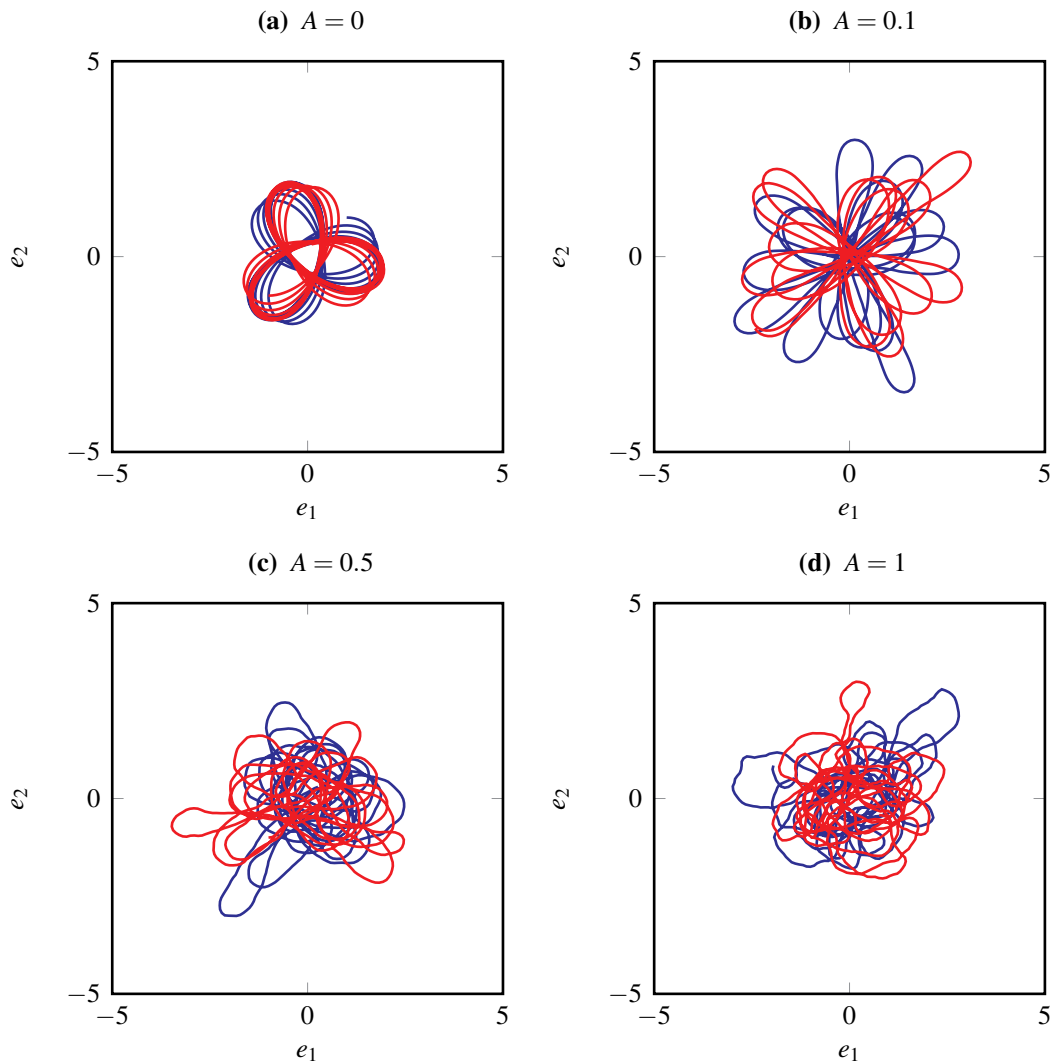
Figure 2.1 – Two independent fibres, solutions of Equation (2.2), with length $t = 100$ and for different noise amplitudes A. The blue and red lines represent single fibres with the initial positions $x_0 = (1,1)^T$ and $x_0 = (-1,-1)^T$ respectively. The initial orientation $\alpha_0 = 0$ is the same for both fibres in all the figures.

2.1.2 The Fokker–Planck equation

When investigating statistical properties of the process, it is sometimes better to consider the associated Fokker–Planck equation instead of the SDE description given by Equation (2.2). The Fokker–Planck equation is a partial differential equation (PDE) and describes the evolution of the (probability–) density $f = f(t, x, \alpha)$, which in our case can be interpreted as the probability of finding a fibre point with arc–length t, position x and orientation α. Also called the *Kolmogoroff forward equation*, the Fokker–Planck equation can be rigorously derived from Equation (2.2). For details we refer the reader to ØKSENDAL (2003), RISKEN (1996), ARNOLD (1973), and GARD (1988). The Fokker–Planck equation corresponding to Equation (2.2) with respect to the Lebesgue measure dx on $\mathbb{R}^2$ and dα

on $[0, 2\pi)$ is given by

$$\partial_t f + v \cdot \nabla_x f - \partial_\alpha \nabla_x V(x) \cdot v^\perp(\alpha) f = \frac{A^2}{2} \partial_{\alpha\alpha} f, \qquad (2.3)$$

with an initial condition $f_0(x, \alpha) = f(0, x, \alpha)$. Furthermore, as f describes a (probability–) density, the normalisation

$$\int_{\mathbb{R}^2} \int_0^{2\pi} f(t, x, \alpha) \, \mathrm{d}\alpha \, \mathrm{d}x = 1,$$

for all $t \geq 0$ is required.

Sometimes the phase space density f itself, depending on position and orientation, may not be of particular interest. What may be more useful, rather, is the probability density for the space coordinate $\rho = \rho(t, x)$, defined by

$$\rho(t, x) = \int_0^{2\pi} f(t, x, \alpha) \, \mathrm{d}\alpha.$$

As f is normalised it follows that the same must be true for ρ

$$\int_{\mathbb{R}^2} \rho(t, x) \, \mathrm{d}x = \int_{\mathbb{R}^2} \int_0^{2\pi} f(t, x, \alpha) \, \mathrm{d}\alpha \, \mathrm{d}x = 1.$$

While the phase space density f gives information on the distribution of α as well as x, the space density ρ only contains information about the position x. The stationary solution of Equation (2.3) yields information about the fibre distribution when the fibres are very long. It is given by

$$f_\infty(x, \alpha) := \lim_{t \to +\infty} f(t, x, \alpha) = \frac{\exp(-V(x))}{\int_{\mathbb{R}^2} \int_0^{2\pi} \exp(-V(x)) \mathrm{d}\alpha \, \mathrm{d}x}, \qquad (2.4)$$

and is independent of the orientation angle α. This implies that all orientations $\alpha \in [0, 2\pi)$ have the same probability at the stationary state. In particular, Equation (2.4) yields the spatial stationary solution

$$\rho_\infty(x) := \lim_{t \to +\infty} \rho(t, x) = \frac{\exp(-V(x))}{\int_{\mathbb{R}^2} \exp(-V(x)) \, \mathrm{d}x}. \qquad (2.5)$$

One can derive simplified equations for ρ which are easier to analyse than the Fokker–Planck equation Equation (2.3) for f, but nevertheless give important insights into the fibre dynamics and their spatial distribution. Considering Equation (2.3) in polar coordinates

for the position x and using the method of multiple time scales in the case of large noise A the reduced first order equation

$$\partial_t \rho = \frac{1}{A^2} \nabla \cdot (\nabla V \rho) + \frac{1}{A^2} \Delta \rho, \tag{2.6}$$

was derived in BONILLA *et al.* (2007). This equation also called the *diffusion approximation* or *hydrodynamic limit*. The stationary solution of Equation (2.6) coincides with the spatial stationary solution of Equation (2.3) given by Equation (2.5). The actual convergence and speed of convergence of the solutions of Equation (2.3) to the stationary state given by Equation (2.5), depending on the model parameters in Equation (2.2) or Equation (2.3), were analysed in GROTHAUS and KLAR (2008), KOLB *et al.* (2012), DOLBEAULT *et al.* (2013), GROTHAUS and STILGENBAUER (2014), and GROTHAUS and STILGENBAUER (2015).

2.1.3   A model with belt movement

The belt movement and the transport of the laid down material plays an important role in the industrial process. A strategy for including this effect in the model given by Equation (2.2) was first hinted at by GÖTZ *et al.* (2007) before being developed further and analysed by BONILLA *et al.* (2007). The basic idea was to introduce a reference curve $\gamma : \mathbb{R}_+ \to \mathbb{R}^2$ which describes the belt movement. The surrogate model with the reference curve is given by

$$
\begin{aligned}
\mathrm{d}\eta_t &= v(\alpha_t)\mathrm{d}t, \\
\mathrm{d}\alpha_t &= -\left(\nabla V(\eta_t - \gamma_t) \cdot v^\perp(\alpha_t) \right) \mathrm{d}t + A\mathrm{d}W_t,
\end{aligned}
\tag{2.7}
$$

where $\eta : \mathbb{R}_+ \to \mathbb{R}^2$ denotes the actual fibre curve. For example, in the meltspinning process, the reference curve can be defined by

$$\gamma_t = -t\psi e_1, \tag{2.8}$$

where $\psi = v_{\mathrm{belt}}/v_{\mathrm{prod}}$ is the ratio of the belt speed v_{belt} and production speed v_{prod}. For $\psi = v_{\mathrm{belt}} = 0$ and, thus, $\gamma = 0$ we obtain the original model given by Equation (2.2) without the reference curve. Writing $x = \eta - \gamma$ allows us to consider the deviation of η from the reference curve γ. Substitution into Equation (2.7) yields

$$
\begin{aligned}
\mathrm{d}x_t &= v_t\mathrm{d}t - \mathrm{d}\gamma_t, \\
\mathrm{d}\alpha_t &= -\left(\nabla V(x_t) \cdot v^\perp(\alpha_t) \right) \mathrm{d}t + A\mathrm{d}W_t.
\end{aligned}
\tag{2.9}
$$

There is a clear difference between the models given by Equations (2.7) and (2.9) and the standard model described in Equation (2.2); in Equations (2.7) and (2.9) the fibre path follows the reference curve instead of being forced in the direction of the origin. Therefore, a stationary state for the model including belt movement cannot in general be expected.

The effect of the belt movement described by Equation (2.8) on the fibre curves is shown in Figure 2.2. In Figure 2.2(a) we can see two fibres when the belt is not moving. Figure 2.2(b) shows x, the deviation from the reference curve described by Equation (2.9), whereas Figure 2.2(c) shows the actual fibre curve η described by Equation (2.7) with $\psi = 0.1$. We obtain a more stretched image when we include belt movement, Figure 2.2(c), as compared to the case of a belt at rest, Figure 2.2(a).

The Fokker–Planck equation for the phase space density $f = f(t,x,\alpha)$ corresponding to Equation (2.7) with respect to the Lebesgue measure $\mathrm{d}x\,\mathrm{d}\alpha$ on $\mathbb{R}^2 \times [0,2\pi)$, is given by

$$\partial_t f + (v + \psi e_1) \cdot \nabla_x f - \partial_\alpha \nabla_x V(x) \cdot v^\perp(\alpha) f = \frac{A^2}{2} \partial_{\alpha\alpha} f. \tag{2.10}$$

To gain some information about the long–time behaviour of Equation (2.7), for large noise amplitudes A, BONILLA *et al.* (2007) derived a reduced model for the space density ρ. This was achieved by considering the Fokker–Planck equation (2.10) and using the Chapman–Enskog method (CERCIGNANI, 1990; BONILLA, 2000). The resulting reduced equation is

$$\partial_t \rho = \frac{1}{A^2} \nabla \cdot \left(\nabla V \rho - A^2 \psi e_1 \rho \right) + \frac{1}{A^2} \Delta \rho, \tag{2.11}$$

and its stationary state is given by

$$\rho_\infty(x) = \frac{\exp\left(-V(x) + A^2 \psi x_1\right)}{\displaystyle\int_{\mathbb{R}^2} \exp\left(-V(x) + A^2 \psi x_1\right)\,\mathrm{d}x}. \tag{2.12}$$

In contrast to the case without belt movement, the stationary solution given by Equation (2.12) depends on the noise amplitude A. When $\psi = 0$, Equation (2.11) coincides with Equation (2.6) as well as the stationary states given by Equations (2.5) and (2.12). The convergence to equilibrium, Equation (2.12), for the reduced model given by Equation (2.11), including convergence rates, has been analysed by BONILLA *et al.* (2007).

The long–time behaviour of the full model, Equation (2.7), has been analysed by KOLB *et al.* (2012) using stochastic methods and recently by BOUIN *et al.* (2016) using hypercoercivity methods from functional analysis. The latter result includes explicit rates for the speed of convergence depending on the initial conditions, the external potential and, in particular, the belt speed. In both publications it was found that convergence to a non–explicit stationary
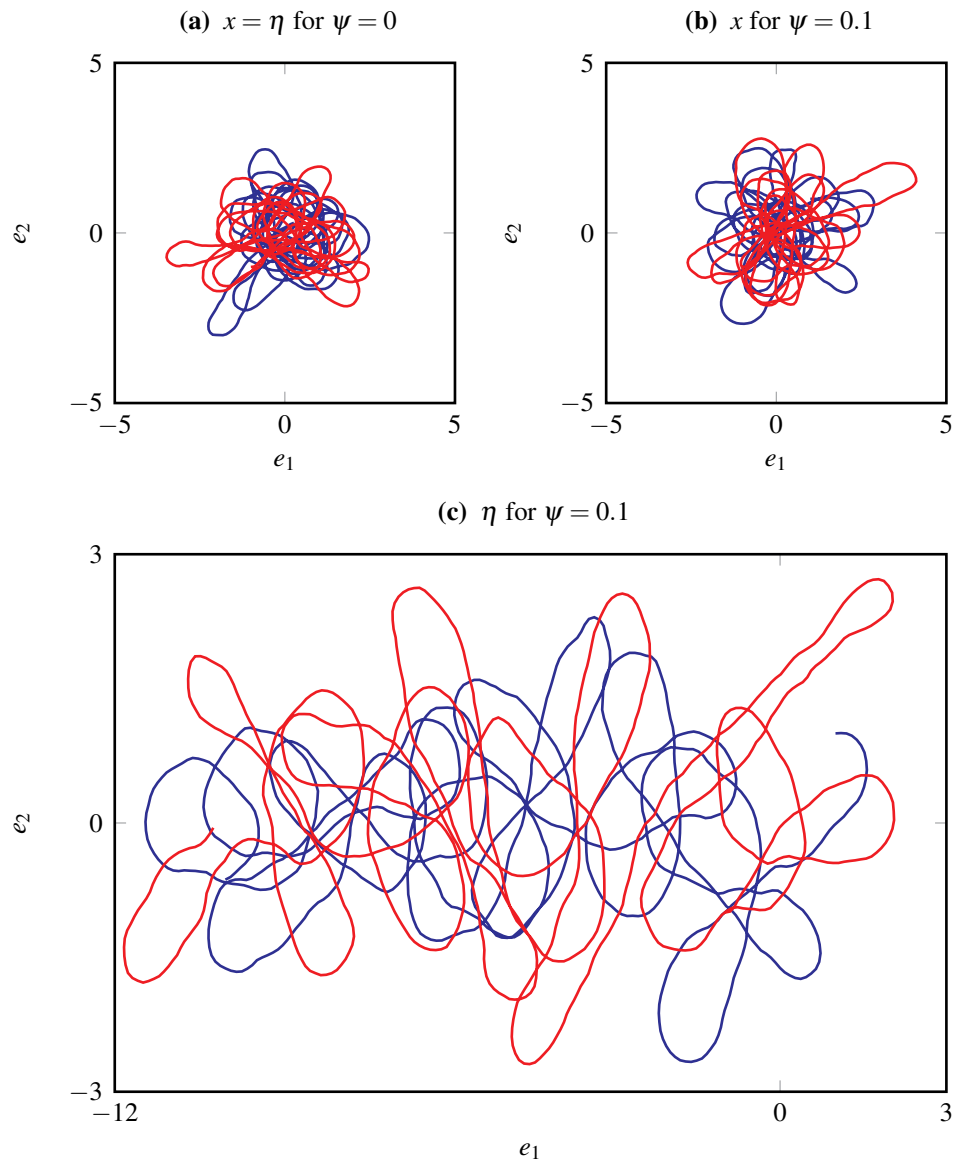
Figure 2.2 – Independent fibres with length $t = 100$ and noise $A = 0.5$, where the belt movement is described by Equation (2.8) with ψ given. Figure 2.2(a) shows solutions of Equation (2.2) without belt movement. Figure 2.2(b) shows two independent solutions of Equation (2.9), the deviation of two fibre curves from the reference curve γ. Figure 2.2(c) shows two fibre curves, solutions of Equation (2.7), experiencing belt movement. The initial positions are $\eta_0 = x_0 = (1,1)^T$ and $\eta_0 = x_0 = (-1,-1)^T$ for the blue and red lines respectively. The initial orientation $\alpha_0 = 0$ is the same for both fibres in all the figures.

state is only given up to a maximal value of ψ, the ratio of belt and production speed. In contrast to these findings, the reduced model given by Equation (2.11) always attains the stationary state given by Equation (2.12).

We note that the belt movement may be incorporated in the remainder of the models described in this chapter by performing the same steps as outlined in this section.

2.1.4 Smooth models

In reality the fibres are smoother than the models already presented suggest. Due to the fact that the Brownian motion is not differentiable, the smoothness of a solution of Equation (2.2) or Equations (2.7) and (2.9) is limited. A higher order of differentiability may be achieved by replacing the non–differentiable Wiener process $(W_t)_{t \geq 0}$ by a differentiable one, namely an *Ornstein-Uhlenbeck process* (JØRGENSEN, 1978; KLAR *et al.*, 2012b; MARINGER, 2013). The one–dimensional Ornstein–Uhlenbeck process is given by

$$\mathrm{d}\kappa_t = -\lambda \kappa_t \mathrm{d}t + \mu \mathrm{d}W_t. \tag{2.13}$$

The parameters λ and μ with $\lambda, \mu > 0$ can be interpreted as the *inverse stiffness* and the diffusion coefficient respectively. Replacing the Brownian motion $(W_t)_{t \geq 0}$ in Equation (2.2) by the Ornstein–Uhlenbeck process given by Equation (2.13) leads to the following smooth fibre model in two dimensions (KLAR *et al.*, 2012b)

$$\begin{aligned}
\mathrm{d}x_t &= v(\alpha_t)\mathrm{d}t, \\
\mathrm{d}\alpha_t &= -\left(\nabla V(x_t) \cdot v^\perp(\alpha_t) \right) \mathrm{d}t + \kappa_t \mathrm{d}t, \\
\mathrm{d}\kappa_t &= -\lambda \kappa_t \mathrm{d}t + \mu \mathrm{d}W_t,
\end{aligned} \tag{2.14}$$

with initial conditions $x_0 \in \mathbb{R}^2, \alpha_0 \in [0, 2\pi)$ and $\kappa_0 \in \mathbb{R}$. The function κ can be interpreted as the fibre curvature. In the *white noise limit*, i.e. the limit $\lambda \to +\infty$ for a fixed ratio μ/λ, one recovers the basic non–smooth model described by Equation (2.2). This corresponds to the case of low stiffness, $1/\lambda \to 0$, and further details may be found in KLAR *et al.* (2012b).

In Figure 2.3 we demonstrate the effect of different choices for μ and λ on the fibre lay down, where $\mu/\lambda = 1$ is kept constant and only the parameter λ is varied. As λ increases, we observe a more chaotic image as we get closer to the white noise limit. The Fokker–Planck equation corresponding to Equation (2.14) for the phase space density $f = f(t, x, \alpha, \kappa)$ with respect to the Lebesgue measure $\mathrm{d}x \, \mathrm{d}\alpha \, \mathrm{d}\kappa$ on $\mathbb{R}^2 \times [0, 2\pi) \times \mathbb{R}$ is
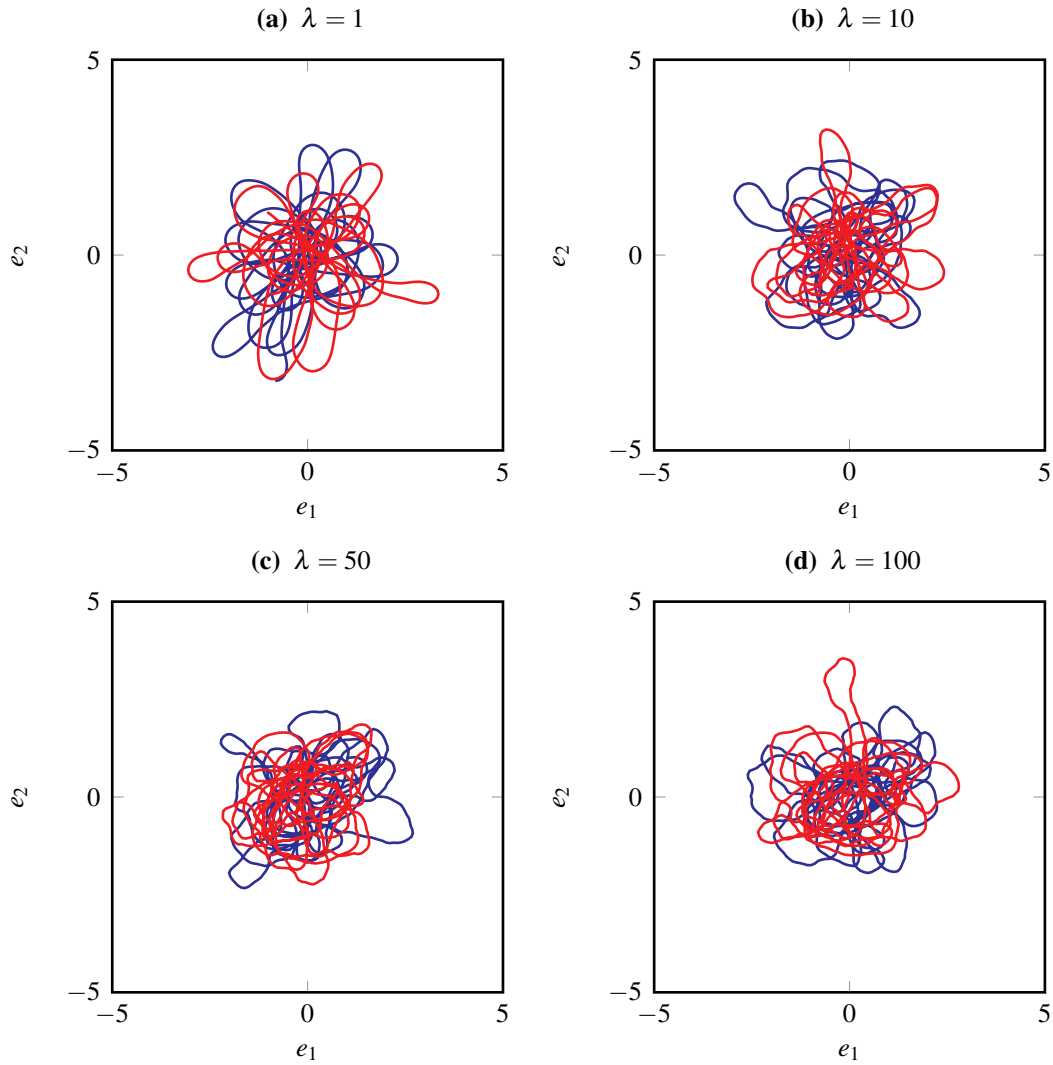
Figure 2.3 – Effect of the inverse stiffness on the image of the fibres given by Equation (2.14), with $\mu/\lambda = 1$, varying values of λ and length $t = 100$. The blue and red lines represent single fibres with the initial positions $x_0 = (1,1)^T$ and $x_0 = (-1,-1)^T$ respectively. The initial orientation $\alpha_0 = 0$ and curvature $\kappa_0 = 0$ is the same for both fibres in all the figures.

given by

$$\partial_t f = -v(\alpha) \cdot \nabla_x \cdot \partial_\alpha \left(v^\perp(\alpha) f \right) - \kappa \partial_\alpha f + \lambda \partial_\kappa (\kappa f) + \frac{1}{2}\mu \partial_{\kappa\kappa} f, \qquad (2.15)$$

where the normalisation

$$\int_{\mathbb{R}^2} \int_0^{2\pi} \int_{\mathbb{R}} f(t,x,\alpha,\kappa) \mathrm{d}\kappa \, \mathrm{d}\alpha \, \mathrm{d}x = 1,$$

is required. The stationary solution of Equation (2.15) is given by

$$f_\infty(x, \alpha, \kappa) = \frac{\exp\left(-V(x)\right) \exp\left(-\dfrac{\lambda \kappa^2}{\mu^2}\right)}{\displaystyle\int_{\mathbb{R}^2} \int_0^{2\pi} \int_{\mathbb{R}} \exp\left(-V(x)\right) \exp\left(-\dfrac{\lambda \kappa^2}{\mu^2}\right) \mathrm{d}\kappa \, \mathrm{d}\alpha \, \mathrm{d}x}. \tag{2.16}$$

As in Section 2.1.2 we see that the stationary solution is independent of α. Furthermore, integrating f_∞ with respect to $\mathrm{d}\kappa$ and $\mathrm{d}\alpha$ gives

$$\rho_\infty(x) = \frac{\exp(-V(x))}{\displaystyle\int_{\mathbb{R}^2} \exp(-V(x)) \, \mathrm{d}x},$$

which coincides with the stationary space density given by Equation (2.5) in the non–smooth case.

The model given by Equation (2.14) was not the first smooth model for fibre lay down. In HERTY *et al.* (2009) a model which is similar to the one given by Equation (2.14) was presented. To compare both descriptions, in MARINGER (2013) an alternative formulation of Equation (2.14) was found. Applying the Itô formula (ØKSENDAL, 2003) to $\hat{\kappa} :=$ $-\nabla V(x) \cdot v^\perp(\alpha) + \kappa$, in combination with Equation (2.14), results in

$$\mathrm{d}x_t = v(\alpha_t)\mathrm{d}t,$$
$$\mathrm{d}\alpha_t = \hat{\kappa}_t \mathrm{d}t, \tag{2.17}$$
$$\mathrm{d}\hat{\kappa}_t = \left(\nabla V(x_t) \cdot v(\alpha_t)\right) \hat{\kappa}_t \mathrm{d}t - \lambda \left(\hat{\kappa}_t + \nabla V(x_t) \cdot v^\perp(\alpha_t)\right) \mathrm{d}t + \mu \mathrm{d}W_t.$$

Compared to Equation (2.17), the term $\left(\nabla V(x_t) \cdot v(\alpha_t)\right) \hat{\kappa}_t \mathrm{d}t$ is missing in HERTY *et al.* (2009) and this results in the loss of an explicit stationary state.

2.2   The basic model in three dimensions

As we have seen so far, two–dimensional models have been established and analysed, including the effect of the belt movement (see Section 2.1.3), and have also been extended to models with a higher order of differentiability (see Section 2.1.4). These simplified models already contain many properties of the real process we aim to describe like coiling, the influence of a turbulent air stream and the belt movement. However, as real non–woven materials have a three–dimensional structure, the extension of the two–dimensional models described in Section 2.1 to three dimensions can yield further detail. A formulation in three dimensions is not directly obvious. KLAR *et al.* (2012a), MARINGER (2013), and STILGENBAUER (2014) first found a formulation in arbitrary space dimensions $d \geq 2$ and

then formulated a new model for three dimensions.

2.2.1   The basic model in arbitrary dimensions

The basic two–dimensional model given by Equation (2.2) (KLAR *et al.*, 2012a; MARINGER, 2013; STILGENBAUER, 2014) can be formulated with respect to x and v instead of x and α. The application of Itô formula to the orientation vector $v(\alpha)$, in combination with Equation (2.2), leads to (KLAR *et al.*, 2012a)

$$
\begin{aligned}
\mathrm{d}x_t &= v_t \mathrm{d}t, \\
\mathrm{d}v_t &= (I - v_t \otimes v_t) \circ (-\nabla V(x_t)\mathrm{d}t + A\mathrm{d}W_t).
\end{aligned}
\tag{2.18}
$$

Here Stratonovich integration, indicated by the symbol $\circ$, is used rather than Itô integration. Furthermore, I denotes the identity matrix and $\otimes$ the tensor product of two vectors. In Equation (2.18), $(W_t)_{t\geq 0}$ denotes a two–dimensional Brownian motion. In the following we only indicate the dimension of the Brownian motion when needed to prevent confusion. We note that $I - v \otimes v$ is a projection on the tangent plane at v

$$
\mathrm{T}_v\mathbb{S}^1 = \left\{ N \in \mathbb{R}^2 \big| N \cdot v = 0 \right\},
$$

which guarantees $v_t \in \mathbb{S}^1$ in the evolution of Equation (2.18).

In the formulation given by Equation (2.18) the two–dimensional nature of the description is no longer obvious. This gave rise to the development of a model for fibre lay down in arbitrary dimensions $d \geq 2$. Before stating the fibre equations in arbitrary dimensions, we first introduce the d–dimensional state space $\mathbb{M}^d = \mathbb{R}^d \times \mathbb{S}^{d-1}$, with the unit sphere $\mathbb{S}^{d-1} \subset \mathbb{R}^d$

$$
\mathbb{S}^{d-1} = \left\{ v \in \mathbb{R}^d \big| \|v\|^2 = 1 \right\}.
$$

Introducing a factor $1/(d-1)$ in Equation (2.18) yields

$$
\begin{aligned}
\mathrm{d}x_t &= v_t \mathrm{d}t, \\
\mathrm{d}v_t &= (I - v_t \otimes v_t) \circ \left(-\frac{1}{d-1}\nabla V(x_t)\mathrm{d}t + A\mathrm{d}W_t \right),
\end{aligned}
\tag{2.19}
$$

where $(W_t)_{t\geq 0}$ denotes a d–dimensional Brownian motion, $(x,v) \in \mathbb{M}^d$, and V is the natural d–dimensional extension of the external potential

$$
V(x) = \frac{1}{2}x^T \Sigma^{-1} x,
$$

with

$$\Sigma = \mathrm{diag}\left\{\sigma_1^2, \ldots, \sigma_d^2\right\}.$$

As in the two–dimensional case, Section 2.1, without loss of generality in the following we will assume that $\sigma_1 = \cdots = \sigma_d = 1$. Sometimes it is more convenient to use the Itô formulation of Equation (2.19) which is given by

$$\begin{aligned}
\mathrm{d}x_t &= v_t \mathrm{d}t, \\
\mathrm{d}v_t &= -(I - v_t \otimes v_t)\frac{1}{d-1}\nabla V(x_t)\mathrm{d}t - \frac{d-1}{2}A^2 v_t \mathrm{d}t + A(I - v_t \otimes v_t)\mathrm{d}W_t.
\end{aligned}$$
(2.20)

We note that in the case of arbitrary dimensions, Equations (2.19) and (2.20), the expression $I - v \otimes v$ is a projection on the tangent plane

$$T_v \mathbb{S}^{d-1} = \left\{N \in \mathbb{R}^d \,\middle|\, N \cdot v = 0\right\}.$$

Furthermore, Equations (2.19) and (2.20) have to be equipped with an initial condition $(x_0, v_0) \in \mathbb{M}^d$.

2.2.2   The basic three–dimensional model

Starting from the basic model in arbitrary dimensions, Equation (2.19), one can retrieve the three–dimensional model by setting $d = 3$. Choosing two linear independent vectors n_1, n_2 spanning the two–dimensional tangent plane at v

$$T_v \mathbb{S}^2 = \mathrm{span}\left\{n_1, n_2\right\},$$

the following identity for the projection on the tangent plane at v holds:

$$I - v \otimes v = n_1 \otimes n_1 + n_2 \otimes n_2.$$

Substitution into Equation (2.19) gives

$$\begin{aligned}
\mathrm{d}x_t &= v_t \mathrm{d}t, \\
\mathrm{d}v_t &= (n_1 \otimes n_1 + n_2 \otimes n_2) \circ \left(-\frac{1}{2}\nabla V(x_t)\mathrm{d}t + A\mathrm{d}W_t\right).
\end{aligned}$$
(2.21)

Sometimes it is useful to have a representation of Equation (2.21) in local coordinates of the orientation vector v. This is done by introducing the angles $\alpha \in [0, 2\pi)$ and $\theta \in [0, \pi)$, which describe the deviation of v from e_1 and the deviation angle of v from the Euclidean

basis vector e_3 respectively, along with the following parametrisation

$$v(\alpha,\theta) = \begin{pmatrix} \cos\alpha\sin\theta \\ \sin\alpha\sin\theta \\ \cos\theta \end{pmatrix}, \quad n_1(\alpha) = \begin{pmatrix} -\sin\alpha \\ \cos\alpha \\ 0 \end{pmatrix}, \quad n_2(\alpha,\theta) = \begin{pmatrix} \cos\alpha\cos\theta \\ \sin\alpha\cos\theta \\ -\sin\theta \end{pmatrix}.$$

Here n_1 and n_2 describe the normal and binormal to v respectively. Note that this choice for n_1 and n_2 guarantees that

$$T_v\mathbb{S}^2 = \mathrm{span}\{n_1,n_2\}.$$

With the application of Itô calculus to v in combination with Equation (2.21), a representation in local coordinates is given by

$$\mathrm{d}x_t = v(\alpha_t,\theta_t)\mathrm{d}t,$$
$$\sin\theta_t\mathrm{d}\alpha_t = -\frac{1}{2}\nabla V(x_t)\cdot n_1(\alpha_t)\mathrm{d}t + A\mathrm{d}W_{t,1}, \tag{2.22}$$
$$\mathrm{d}\theta_t = -\frac{1}{2}\nabla V(x_t)\cdot n_2(\alpha_t,\theta_t)\mathrm{d}t + \frac{1}{2}A^2\cot\theta_t\mathrm{d}t + A\mathrm{d}W_{t,2}.$$

Here $(W_{t,1})_{t\geq 0}$ and $(W_{t,2})_{t\geq 0}$ denote one–dimensional and independent Brownian motions. Figure 2.4 illustrates the influence of A on the fibres. As in the two–dimensional case, we can see that the regular structure in Figure 2.4(a) becomes irregular and chaotic as A increases. The corresponding Fokker–Planck equation for $f = f(t,x,\alpha,\theta)$ with respect to the Lebesgue measure $\mathrm{d}x$ on $\mathbb{R}^3$ and the spherical measure $\mathrm{d}v = \mathrm{d}v(\alpha,\theta) = \mathrm{d}\alpha\,\mathrm{d}\theta$ is given by

$$\partial_t f + v(\alpha,\theta)\cdot\nabla_x f - \frac{1}{2}\frac{1}{\sin\theta}\nabla_x V(x)\cdot\partial_\alpha\left(n_1(\alpha)f\right) - \frac{1}{2}\nabla_x V(x)\cdot\partial_\theta\left(n_2(\alpha,\theta)f\right)$$
$$= -\frac{1}{2}A^2\partial_\theta\left(\cot\theta f\right) + \frac{1}{2}\frac{A^2}{\sin^2\theta}\partial_{\alpha\alpha}f + \frac{1}{2}A^2\partial_{\theta\theta}f. \tag{2.23}$$

The stationary solution is given by

$$f_\infty(x,\alpha,\theta) = \frac{\sin\theta\exp\left(-V(x)\right)}{\displaystyle\int_{\mathbb{R}^3}\int_0^{2\pi}\int_0^\pi \sin\theta\exp\left(-V(x)\right)\,\mathrm{d}\theta\,\mathrm{d}\alpha\,\mathrm{d}x}. \tag{2.24}$$

Note that f_∞ is independent of α. Furthermore, f_∞ factorises in a component depending on θ and x respectively. Considering the angular component $\sin\theta$, one can see that this describes a uniform distribution on $\mathbb{S}^2$ with respect to the measure $\mathrm{d}v$. In particular, the external potential V does not influence the orientation distribution. Integrating

Figure 2.4 – Two independent fibres, solutions of Equation (2.22), with length $t = 100$ and varying noise amplitude A. The blue and red lines represent single fibres with the initial positions $x_0 = (1, 1, 0)^T$ and $x_0 = (-1, -1, 0)^T$ respectively. The initial orientation $(\alpha_0, \theta_0) = (0, \pi/2)$ is the same for both fibres in all the figures.

Equation (2.24) with respect to $d\nu(\alpha, \theta)$ results in the stationary space density

$$\rho_\infty(x) = \frac{\exp(-V(x))}{\displaystyle\int_{\mathbb{R}^3} \exp(-V(x)) \ dx}, \tag{2.25}$$

which is structurally identical to the stationary solution given by Equation (2.5) for two dimensions.

2.2.3 The anisotropic model

We have seen that, based on the model in arbitrary dimension given by Equation (2.19), a three–dimensional version similar to the two–dimensional one given by Equation (2.2)

can be formulated. This model has a uniform stationary distribution with respect to the orientation angles α and θ. However, the orientation distribution of fibres in real non–woven materials is not isotropic. They have a preferred orientation parallel to the belt. To overcome this shortcoming in the three–dimensional model given by Equation (2.22), the *anisotropic* model was developed (KLAR *et al.*, 2012a). It aims to model the resulting non–woven material with a realistic thickness and typical orientation distribution. Starting from the isotropic three–dimensional model in spherical coordinates, Equation (2.22), the idea is to scale the influence of the normal $n_1(\alpha)$ and the binormal $n_2(\alpha, \theta)$ by introducing a parameter $B \in [0, 1]$. The resulting model is (KLAR *et al.*, 2012a)

$$
\begin{aligned}
\mathrm{d}x_t &= v(\alpha_t, \theta_t)\mathrm{d}t, \\
\sin\theta_t \mathrm{d}\alpha_t &= -\frac{1}{B+1}\nabla V(x_t) \cdot n_1(\alpha_t)\mathrm{d}t + A\mathrm{d}W_{t,1}, \\
\mathrm{d}\theta_t &= -\frac{B}{B+1}\nabla V(x_t) \cdot n_2(\alpha_t, \theta_t)\mathrm{d}t + \frac{1}{2}A^2\cot\theta_t\mathrm{d}t + \sqrt{B}A\mathrm{d}W_{t,2}.
\end{aligned}
\tag{2.26}
$$

Equation (2.26) reverts to the isotropic case given by Equation (2.22) with $d = 3$ when $B = 1$ and with the initial conditions $x_0 \in \mathbb{R}^3$, $\alpha \in [0, 2\pi)$ and $\theta \in [0, \pi)$. However, when $B = 0$, we require that Equation (2.26) reverts to the two–dimensional model given by Equation (2.2). Therefore, it is necessary that the third component of x vanishes, $x_{t,3} = 0$, and that $\theta_t = \pi/2$ for all t. When we set $B = 0$ in Equation (2.26), the terms $-\frac{B}{B+1}\nabla V(x_t) \cdot n_2(\alpha_t, \theta_t)\mathrm{d}t$ and $\sqrt{B}A\mathrm{d}W_{t,2}$ vanish. Recalling that the third component of the orientation vector is $v_3(\alpha, \theta) = \cos\theta$, we obtain the following set of ODEs independent of all the other quantities

$$
\begin{aligned}
\mathrm{d}x_{t,3} &= \cos\theta_t \mathrm{d}t, \\
\mathrm{d}\theta_t &= \frac{1}{2}A^2\cot\theta_t\mathrm{d}t,
\end{aligned}
$$

which has the explicit solution

$$
\begin{aligned}
\theta_t &= \arccos\left(\exp\left(-\frac{1}{2}A^2 t\right)\cos\theta_0\right), \\
x_{t,3} &= x_{0,3} + \frac{2}{A^2}\cos\theta_0 - \frac{2}{A^2}\exp\left(-\frac{1}{2}A^2 t\right)\cos\theta_0.
\end{aligned}
$$

This is only possible with the initial conditions $\theta_0 = \pi/2$ and $x_{0,3} = 0$.

In Figure 2.5 we can see the influence of the parameter B on the fibre curves for $A = 0.5$. We observe that the fibres have a more anisotropic angular distribution for decreasing B. In the extreme case $B = 0$, we obtain a purely two–dimensional image for the fibre positions with constant $\theta = \pi/2$. We see that the anisotropic model given by Equation (2.26) yields the

(a) $B = 1$
(b) $B = 10^{-2}$
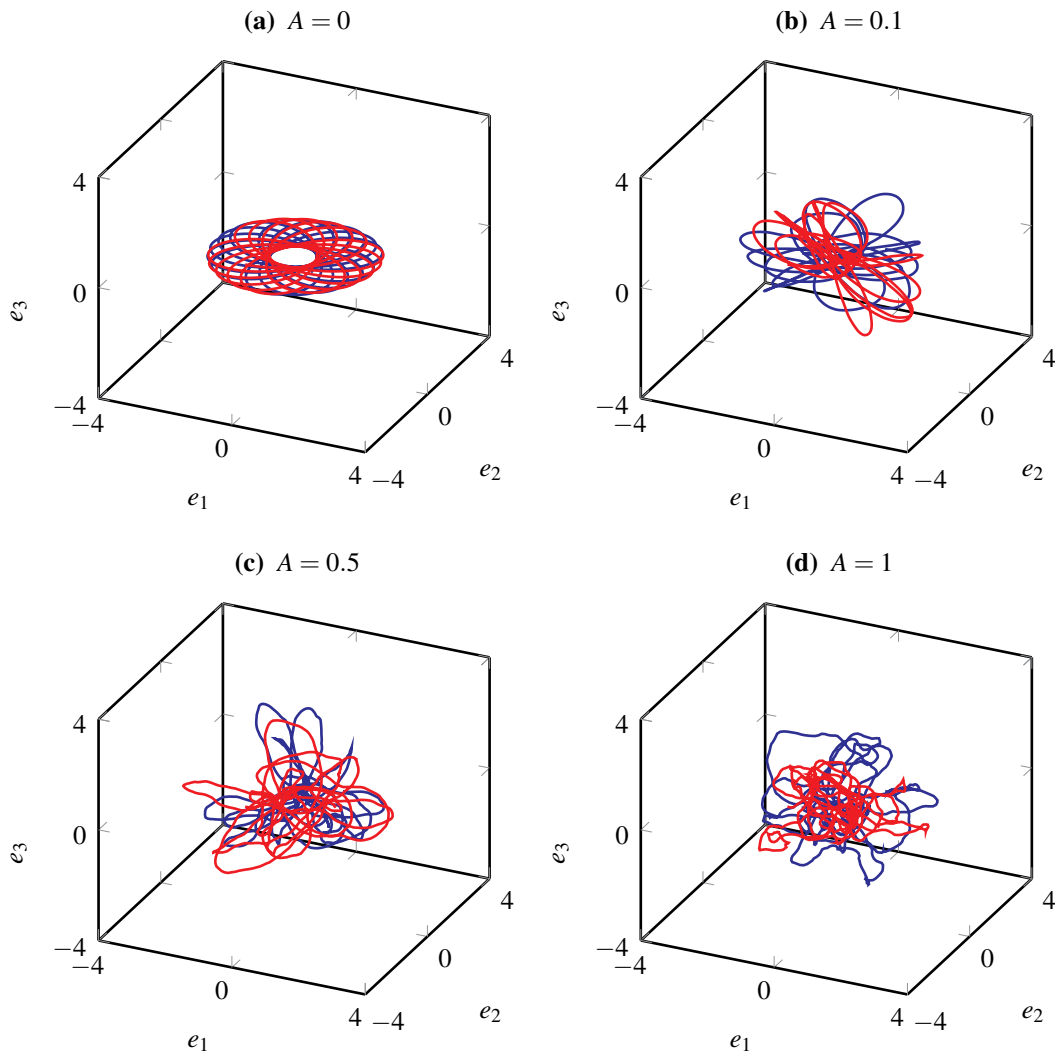**(c)** $B = 10^{-3}$
(d) $B = 0$
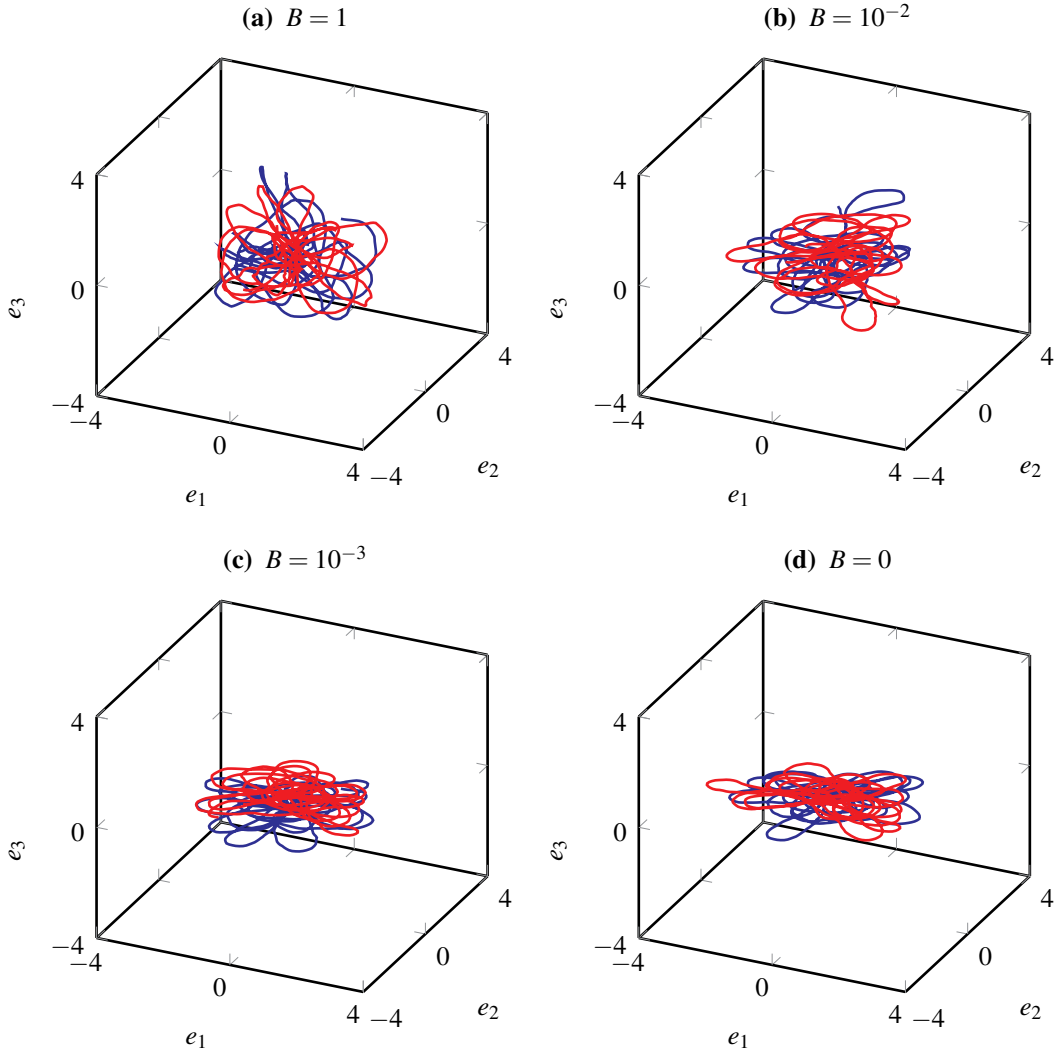
Figure 2.5 – Two independent fibres, solutions of Equation (2.26), with length $t = 100$ and fixed noise amplitude $A = 0.5$. The blue and red lines represent single fibres with the initial positions $x_0 = (1,1,0)^T$ and $x_0 = (-1,-1,0)^T$ respectively. The initial orientation $(\alpha_0, \theta_0) = (0, \pi/2)$ is the same for both fibres in all the figures.

correct behaviour for the extremal cases $B = 0$ and $B = 1$. As B decreases (top left to bottom right) we observe an increasingly two–dimensional distribution. In order to get a better understanding of the influence of B on the fibre orientation distribution, we consider the Fokker–Planck equation for $f = f(t, x, \alpha, \theta)$ corresponding to Equation (2.26) with respect to the Lebesgue measure dx on $\mathbb{R}^3$ and the spherical measure $d\nu = d\nu(\alpha, \theta) = d\alpha \, d\theta$ on $[0, 2\pi) \times [0, \pi)$ given by (KLAR *et al.*, 2012a)

$$\partial_t f + v(\alpha, \theta) \cdot \nabla_x f - \frac{1}{B+1} \frac{1}{\sin \theta} \nabla_x V(x) \cdot \partial_\alpha (n_1(\alpha) f) - \frac{B}{B+1} \nabla_x V(x) \cdot \partial_\theta (n_2(\alpha, \theta) f)$$

$$= -\frac{1}{2} A^2 \partial_\theta (\cot \theta \, f) + \frac{1}{2} \frac{A^2}{\sin^2 \theta} \partial_{\alpha\alpha} f + \frac{1}{2} A^2 B \partial_{\theta\theta} f. \quad (2.27)$$
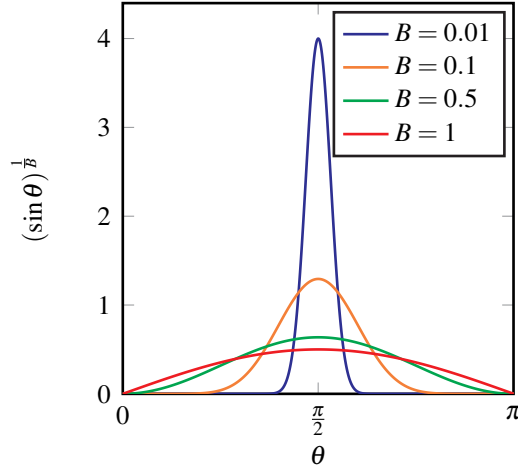
Figure 2.6 – Angular distribution $(\sin\theta)^{\frac{1}{B}}$ for different values of *B*.

Its stationary solution is

$$f_\infty(x,\alpha,\theta) = \frac{(\sin\theta)^{\frac{1}{B}}\exp(-V(x))}{\displaystyle\int_{\mathbb{R}^3}\int_0^\pi\int_0^{2\pi}(\sin\theta)^{\frac{1}{B}}\exp(-V(x))\,\mathrm{d}\theta\,\mathrm{d}\alpha\,\mathrm{d}x},\qquad(2.28)$$

for $B > 0$. Integrating Equation (2.28) with respect to dv results in the stationary space density ρ_∞ which is identical to Equation (2.25). We see that f_∞, as in the isotropic case in Equation (2.24), is independent of α and factorises in terms containing θ and x. Furthermore, one can see that the anisotropic parameter *B* has an influence on the angular distribution of f_∞. The term $(\sin\theta)^{\frac{1}{B}}$ is symmetric around $\pi/2$ and obtains its maximum at $\pi/2$ for all $0 < B \leq 1$. As expected, when $B = 1$ the stationary solutions given by Equations (2.24) and (2.28) are identical. In the other extreme case $B \to 0$ one obtains

$$(\sin\theta)^{\frac{1}{B}} \xrightarrow{B\to 0} \delta_{\frac{\pi}{2}}(\theta),$$

where $\delta_{\frac{\pi}{2}}$ is the Dirac delta distribution on $[0,\pi)$ centred at $\pi/2$ (MARINGER, 2013). In Figure 2.6 we can see how the density $(\sin\theta)^{\frac{1}{B}}$ behaves on the interval $[0,\pi]$ for different values of *B*. One can see that the variance of $(\sin\theta)^{\frac{1}{B}}$ is monotonically increasing with respect to *B*, whereas the expectation is constant. As in two spatial dimensions, Section 2.1, a reduced model for the space density ρ can be derived (KLAR *et al.*, 2012a) and is given by

$$\partial_t\rho - \frac{1}{A^2(1+2B)}\nabla_x\cdot D(\nabla_x\rho + \nabla_x V(x)\rho) = 0,\qquad(2.29)$$

where

$$D = \text{diag}\left\{1, 1, \frac{2B}{1+B}\right\} \in \mathbb{R}^{3\times 3},$$

is a diagonal matrix. The stationary solution of Equation (2.29) is identical to the stationary space density of Equation (2.23) and Equation (2.27). This result emphasises the fact that, although the parameter B does not have an influence on the stationary spatial distribution, it does have an effect on the evolution of the space density.

2.3 The smooth model in three dimensions

As we have seen for the two–dimensional case described in Section 2.1, smooth extensions to Equation (2.2) are possible and can play a relevant role in the fibre lay down model to achieve a higher order of regularity. This is also the case for a three–dimensional model (KLAR *et al.*, 2012b; MARINGER, 2013). However, as it is the case for the basic model, a three–dimensional smooth formulation is not directly obvious. Thus, we first summarise the results for arbitrary dimensions $d \geq 2$ before we state the smooth model in three dimensions.

2.3.1 The smooth model in arbitrary dimensions

As in the basic case described in Section 2.1.1, the smooth model in two dimensions given by Equation (2.14) has a similar formulation in arbitrary dimensions (KLAR *et al.*, 2012b; MARINGER, 2013).

By introducing $N := v^{\perp}\kappa$ the two–dimensional description from Section 2.1.4 using Itô calculus for $v \in \mathbb{S}^1$ and $N \in \mathrm{T}_v\mathbb{S}^1$ can be written as (KLAR *et al.*, 2012b; MARINGER, 2013)

$$
\begin{aligned}
\mathrm{d}x_t &= v_t\mathrm{d}t, \\
\mathrm{d}v_t &= -\left(I - v_t \otimes v_t\right)\nabla V(x_t)\mathrm{d}t + N_t\mathrm{d}t, \\
\mathrm{d}N_t &= \left(v_t \otimes N_t\right)\nabla V(x_t)\mathrm{d}t - |N_t|^2 v_t\mathrm{d}t - \lambda N_t\mathrm{d}t + \mu\left(I - v_t \otimes v_t\right)\mathrm{d}W_t.
\end{aligned}
\tag{2.30}
$$

The initial conditions are given by $x_0 \in \mathbb{R}^2$ and $(v_0, N_0) \in \mathbb{TS}^1$, where

$$\mathbb{TS}^1 := \left\{(v, N) \in \mathbb{R}^2 \times \mathbb{R}^2 \,\middle|\, \|v\|^2 = 1, v \cdot N = 0\right\},$$

is the tangent bundle of the sphere $\mathbb{S}^1$. The evolution of the process given by Equation (2.30) guarantees that $(v_t, N_t) \in \mathbb{TS}^1$. These equations inherit, as in the basic case Section 2.1.1, a space dimension–independent description for $d \geq 2$. Introducing an additional factor

$1/(d-1)$, the smooth model in arbitrary dimensions $d \geq 2$ is given by

$$
\begin{aligned}
\mathrm{d}x_t &= v_t \mathrm{d}t, \\
\mathrm{d}v_t &= -(I - v_t \otimes v_t) \nabla \frac{1}{d-1} V(x_t) \mathrm{d}t + N_t \mathrm{d}t, \\
\mathrm{d}N_t &= (v_t \otimes N_t) \nabla \frac{1}{d-1} V(x_t) \mathrm{d}t - |N_t|^2 v_t \mathrm{d}t - \lambda N_t \mathrm{d}t + \mu (I - v_t \otimes v_t) \mathrm{d}W_t,
\end{aligned}
$$

(2.31)

where $x \in \mathbb{R}^d$ and $(v, N) \in \mathbb{TS}^{d-1}$, with the tangent bundle

$$
\mathbb{TS}^{d-1} := \left\{ (v, N) \in \mathbb{R}^d \times \mathbb{R}^d \,\middle|\, \|v\|^2 = 1, v \cdot N = 0 \right\}.
$$

2.3.2   The smooth isotropic model

In general, one obtains the three–dimensional smooth model by setting $d = 3$ in Equation (2.31). In addition, one can reformulate the equation in spherical coordinates as is done in Section 2.2.2. As N is orthogonal to v and n_1, n_2 span the tangential plane at v, it is possible to write $N(\alpha, \theta) = \kappa_1 n_1(\alpha) + \kappa_2 n_2(\alpha, \theta)$, where $\kappa_1, \kappa_2 \in \mathbb{R}$. The application of Itô calculus to N and v in combination with Equation (2.31) leads to a description in local coordinates (KLAR *et al.*, 2012b)

$$
\begin{aligned}
\mathrm{d}x_t &= v(\alpha_t, \theta_t) \mathrm{d}t, \\
\sin \theta_t \mathrm{d}\alpha_t &= -\frac{1}{2} \left(\nabla V(x_t) \cdot n_1(\alpha_t) \right) \mathrm{d}t + \kappa_{t,1} \mathrm{d}t, \\
\mathrm{d}\theta_t &= -\frac{1}{2} \left(\nabla V(x_t) \cdot n_2(\alpha_t, \theta_t) \right) \mathrm{d}t + \kappa_{t,2} \mathrm{d}t, \\
\mathrm{d}\kappa_{t,1} &= \frac{1}{2} \left(\nabla V(x_t) \cdot n_1(\alpha_t) \right) \kappa_{2,t} \cot \theta_t \mathrm{d}t - \lambda \kappa_{t,1} \mathrm{d}t - \kappa_{t,1} \kappa_{t,2} \cot \theta_t \mathrm{d}t + \mu \mathrm{d}W_{t,1}, \\
\mathrm{d}\kappa_{t,2} &= -\frac{1}{2} \left(\nabla V(x_t) \cdot n_2(\alpha_t) \right) \kappa_{t,1} \cot \theta_t \mathrm{d}t - \lambda \kappa_{t,2} \mathrm{d}t + \kappa_{t,1}^2 \cot \theta_t \mathrm{d}t + \mu \mathrm{d}W_{t,2}.
\end{aligned}
$$

(2.32)

As in the two–dimensional case Section 2.1.4, we can take the white noise limit for $\lambda \to +\infty$ and constant ratio μ/λ. For details, see KLAR *et al.* (2012b).

Figure 2.7 shows the influence of the parameters μ and λ on the solutions of Equation (2.32). Whereas Figures 2.7(a) and 2.7(c) show fibres for the ratio $\mu/\lambda = 1$, Figures 2.7(b) and 2.7(d) show results for $\mu/\lambda = 1/10$.

The corresponding Fokker–Planck equation for $f = f(t, x, \alpha, \theta, \kappa_1, \kappa_2)$ with respect to the

(a) $\mu = 1, \lambda = 1$

(b) $\mu = 1, \lambda = 10$

(c) $\mu = 2, \lambda = 2$

(d) $\mu = 2, \lambda = 20$
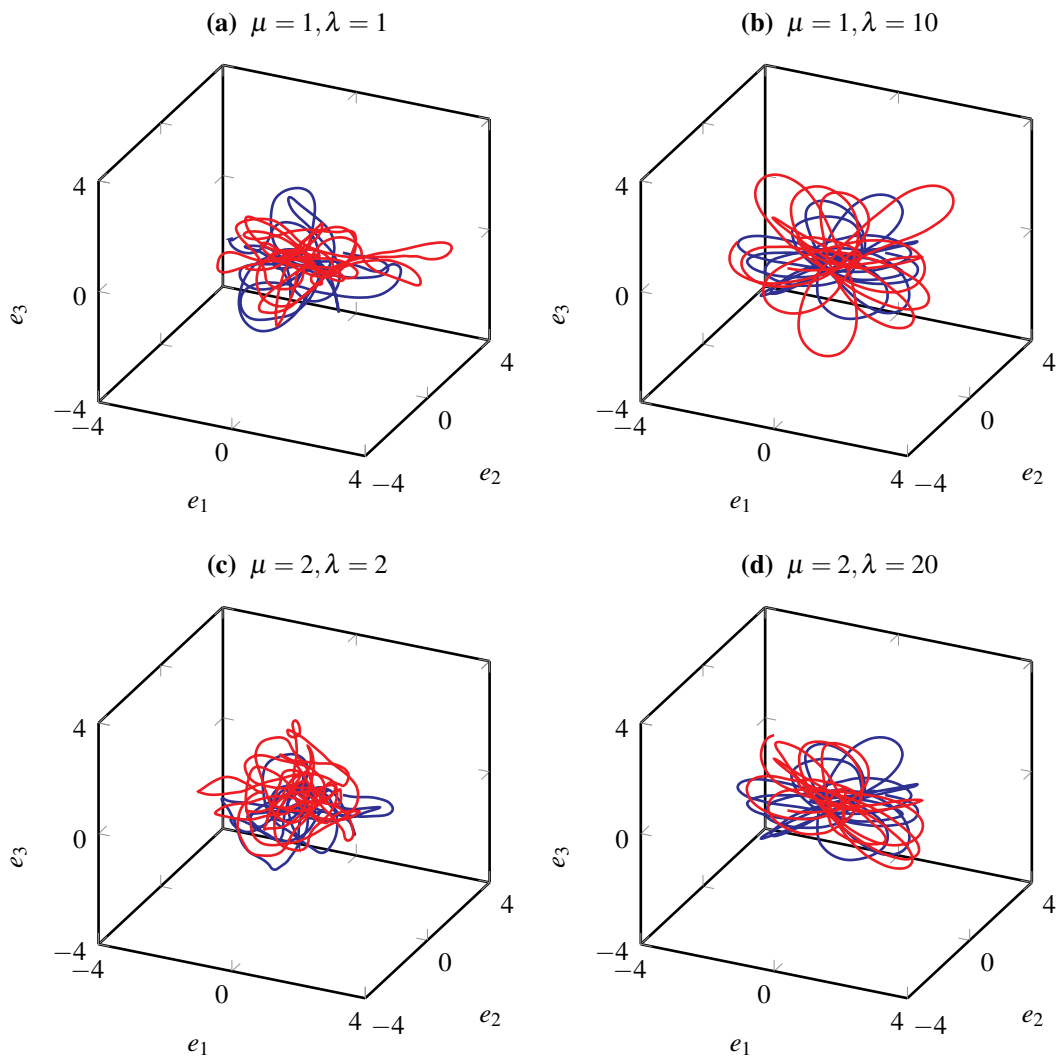
Figure 2.7 – Two independent fibres, solutions of Equation (2.32), with length $t = 100$ and varying parameters μ and λ. The blue and red lines represent single fibres with the initial positions $x_0 = (1, 1, 0)^T$ and $x_0 = (-1, -1, 0)^T$ respectively. The initial orientation and curvature, $(\alpha_0, \theta_0) = (0, \pi/2)$ and $(\kappa_{0,1}, \kappa_{0,2}) = (0, 0)$ respectively, are the same for both fibres in all the figures.

Lebesgue measure is given by

$$
\begin{aligned}
\partial_t f = & - v(\alpha, \theta) \cdot \nabla_x f + \frac{1}{\sin \theta} \frac{1}{2} \nabla_x V(x) \cdot \partial_\alpha (n_1(\alpha) f) + \frac{1}{2} \nabla_x V(x) \cdot \partial_\theta (n_2(\alpha, \theta) f) \\
& - \frac{1}{2} (\nabla_x V(x) \cdot n_1(\alpha)) \kappa_2 \cot \theta \partial_{\kappa_1} f + \frac{1}{2} (\nabla_x V(x) \cdot n_1(\alpha)) \kappa_1 \cot \theta \partial_{\kappa_2} f \\
& - \frac{1}{\sin \theta} \kappa_1 \partial_\alpha f - \kappa_2 \partial_\theta f + \lambda \partial_{\kappa_1} (\kappa_1 f) + \kappa_2 \cot \theta \partial_{\kappa_1} (\kappa_1 f) + \lambda \partial_{\kappa_2} (\kappa_2 f) \\
& - \kappa_1^2 \cot \theta \partial_{\kappa_2} f + \frac{1}{2} \mu^2 \partial_{\kappa_1 \kappa_1} f + \frac{1}{2} \mu^2 \partial_{\kappa_2 \kappa_2} f.
\end{aligned}
$$

The respective stationary solution is

$$
f_\infty(x, \alpha, \theta, \kappa_1, \kappa_2) =
$$

$$
\frac{\sin \theta \exp(-V(x)) \exp\left(-\frac{\lambda \kappa_1^2}{\mu^2}\right) \exp\left(-\frac{\lambda \kappa_2^2}{\mu^2}\right)}{\int_{\mathbb{R}^3} \int_0^{2\pi} \int_0^\pi \int_\mathbb{R} \int_\mathbb{R} \sin \theta \exp(-V(x)) \exp\left(-\frac{\lambda \kappa_1^2}{\mu^2}\right) \exp\left(-\frac{\lambda \kappa_2^2}{\mu^2}\right) \, d\kappa_2 \, d\kappa_1 \, d\theta \, d\alpha \, dx},
$$

$$
\tag{2.33}
$$

which is as previously independent of α.

2.3.3 The smooth anisotropic model

So far we have reviewed the smooth model in three dimensions, including a formulation in local coordinates. As in the derivation of the basic anisotropic model described in Section 2.2.3, one can introduce an additional scaling $B \in [0, 1]$ of the normal n_1 and binormal n_2 to achieve a desired angular distribution. The modification of Equation (2.32) in this manner yields (KLAR *et al.*, 2012b)

$$
\begin{aligned}
dx_t &= v(\alpha_t, \theta_t) dt, \\
\sin \theta_t d\alpha_t &= -\frac{1}{B+1} (\nabla V(x_t) \cdot n_1(\alpha_t)) \, dt + \kappa_{t,1} dt, \\
d\theta_t &= -\frac{B}{B+1} (\nabla V(x_t) \cdot n_2(\alpha_t, \theta_t)) \, dt + B \kappa_{t,2} dt, \\
d\kappa_{t,1} &= \frac{1}{B+1} (\nabla V(x_t) \cdot n_1(\alpha_t)) \kappa_{t,2} \cot \theta_t dt - \lambda \kappa_{t,1} dt - \kappa_{t,1} \kappa_{t,2} \cot \theta_t dt + \mu dW_{t,1}, \\
d\kappa_{t,2} &= -\frac{1}{B+1} (\nabla V(x_t) \cdot n_2(\alpha_t, \theta_t)) \kappa_{t,1} \cot \theta_t dt - B \lambda \kappa_{t,2} dt + \kappa_{t,1}^2 \cot \theta_t dt + \sqrt{B} \mu dW_{t,2}.
\end{aligned}
$$

$$
\tag{2.34}
$$

Figure 2.8 shows the effect of the parameter B on the fibres. As in the non–smooth case, Section 2.2.3, one observes an angular distribution concentrating towards $\theta = \pi/2$ for decreasing B.

(a) $B = 1$

(b) $B = 10^{-2}$

(c) $B = 10^{-3}$

(d) $B = 0$
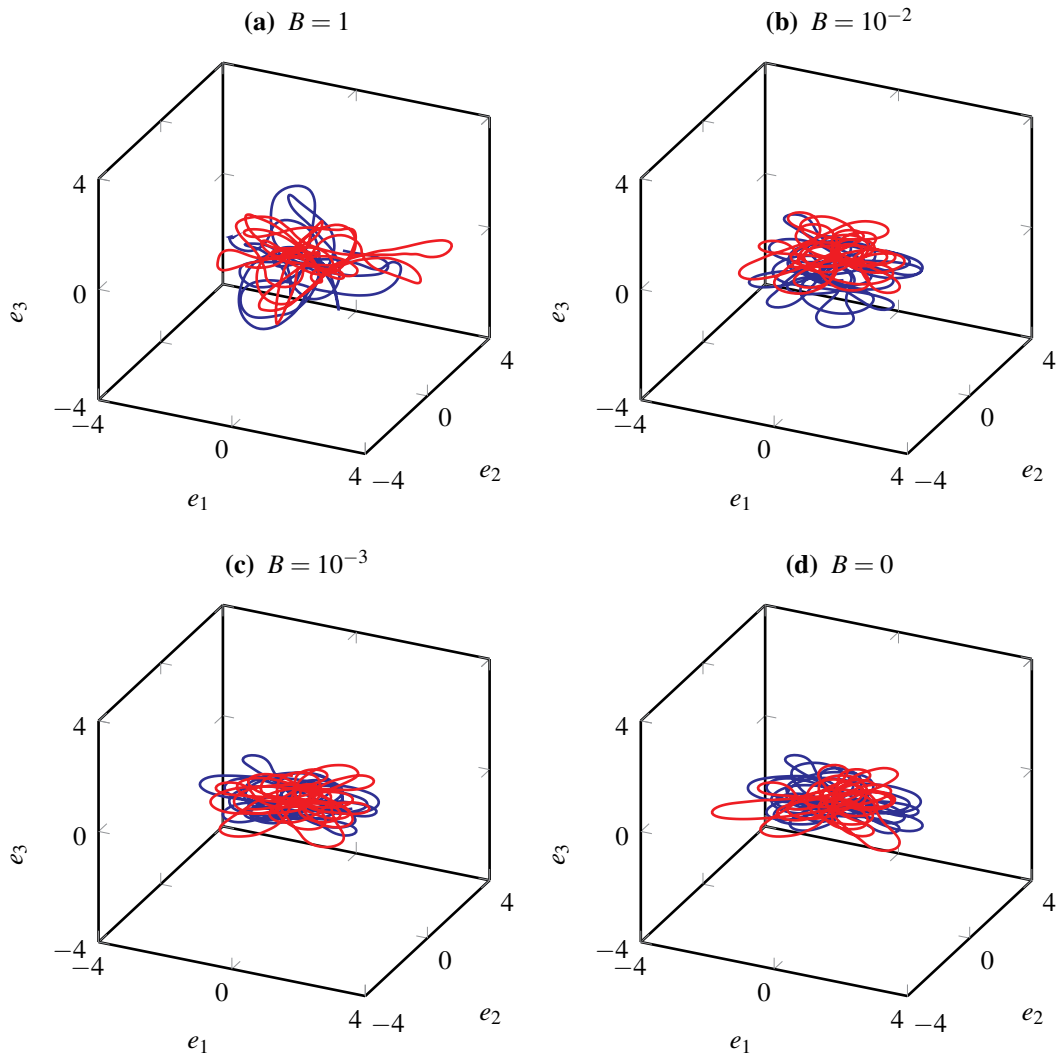
Figure 2.8 – Two independent fibres, solutions of Equation (2.34), which demonstrate the effect of decreasing values of B. For all simulations we used fix values $\lambda = 1$ and $\mu = 1$. The blue and red lines represent single fibres with the initial positions $x_0 = (1, 1, 0)^T$ and $x_0 = (-1, -1, 0)^T$ respectively. The initial orientation and curvature, $(\alpha_0, \theta_0) = (0, \pi/2)$ and $(\kappa_{0,1}, \kappa_{0,2}) = (0, 0)$ respectively, are the same for both fibres in all the figures.

As in the non–smooth case, Section 2.2.3, setting $B = 1$ results in the isotropic smooth three–dimensional model described by Equation (2.32). Setting $B = 0$, $x_{0,3} = 0$, $\kappa_{0,2} = 0$ and $\theta_0 = \pi/2$ leads to the two–dimensional smooth model described by Equation (2.14) (MARINGER, 2013). As in the two–dimensional case, Section 2.1.4, taking the white noise limit, $\lambda \to \infty$ for fixed ratio μ/λ, gives the non–smooth model, Equation (2.26) (KLAR *et al.*, 2012b).

The corresponding Fokker–Planck equation for $f = f(t, x, \alpha, \theta, \kappa_1, \kappa_2)$ with respect to the Lebesgue measure $d\kappa_2\, d\kappa_1\, d\alpha\, d\theta\, dx$ on $\mathbb{R} \times \mathbb{R} \times [0, \pi) \times [0, 2\pi) \times \mathbb{R}^2$ is given by

$$
\begin{aligned}
\partial_t f = {}& -v(\alpha, \theta) \cdot \nabla_x f + \frac{1}{\sin\theta} \frac{1}{B+1} \nabla_x V(x) \cdot \partial_\alpha \left(n_1(\alpha) f \right) + \frac{B}{B+1} \nabla_x V(x) \cdot \partial_\theta \left(n_2(\alpha, \theta) f \right) \\
& - \frac{1}{B+1} \left(\nabla_x V(x) \cdot n_1(\alpha) \right) \kappa_2 \cot\theta \partial_{\kappa_1} f + \frac{1}{B+1} \left(\nabla_x V(x) \cdot n_1(\alpha) \right) \kappa_1 \cot\theta \partial_{\kappa_2} f \\
& - \frac{1}{\sin\theta} \kappa_1 \partial_\alpha f - B\kappa_2 \partial_\theta f + \lambda \partial_{\kappa_1} \left(\kappa_1 f \right) + \kappa_2 \cot\theta \partial_{\kappa_1} \left(\kappa_1 f \right) + B\lambda \partial_{\kappa_2} \left(\kappa_2 f \right) \\
& - \kappa_1^2 \cot\theta \partial_{\kappa_2} f + \frac{1}{2} \mu^2 \partial_{\kappa_1 \kappa_1} f + \frac{1}{2} B\mu^2 \partial_{\kappa_2 \kappa_2} f. \quad (2.35)
\end{aligned}
$$

The respective stationary solution is (KLAR *et al.*, 2012b)

$$
\begin{aligned}
&f_\infty(x, \alpha, \theta, \kappa_1, \kappa_2) = \\
&\frac{(\sin\theta)^{\frac{1}{B}} \exp\left(-V(x)\right) \exp\left(-\dfrac{\lambda \kappa_1^2}{\mu^2}\right) \exp\left(-\dfrac{\lambda \kappa_2^2}{\mu^2}\right)}{\displaystyle\int_{\mathbb{R}^3} \int_0^{2\pi} \int_0^\pi \int_{\mathbb{R}} \int_{\mathbb{R}} (\sin\theta)^{\frac{1}{B}} \exp\left(-V(x)\right) \exp\left(-\dfrac{\lambda \kappa_1^2}{\mu^2}\right) \exp\left(-\dfrac{\lambda \kappa_2^2}{\mu^2}\right) \, d\kappa_2\, d\kappa_1\, d\theta\, d\alpha\, dx}.
\end{aligned}
$$

$$(2.36)$$

As in the non–smooth anisotropic case, Section 2.2.3, the influence of B on the angular distribution can be seen. Integration with respect to $d\kappa_1$ and $d\kappa_2$, as in Section 2.3.2, gives

$$
\int_{\mathbb{R}} \int_{\mathbb{R}} f_\infty(x, \alpha, \theta, \kappa_1, \kappa_2)\, d\kappa_2\, d\kappa_1 = \frac{(\sin\theta)^{\frac{1}{B}} \exp\left(-V(x)\right)}{\displaystyle\int_0^\pi \int_0^{2\pi} \int_{\mathbb{R}^3} (\sin\theta)^{\frac{1}{B}} \exp\left(-V(x)\right) d\theta\, d\alpha\, dx},
$$

which is identical to the stationary solution of Equation (2.27) in the non–smooth case.

2.4 Summary

In this chapter we have presented an overview of several existing surrogate models for fibre lay down and their connections. We have seen that the basic two–dimensional model described in GÖTZ *et al.* (2007) served as a basis for numerous extensions including

models in higher dimensions, models including an anisotropic angular distribution and smooth versions. These equations have given rise to a multitude of research questions, including that of the convergence to equilibrium. In contrast to the models presented in this chapter, in the following we will introduce a novel model in which the fibre thickness and, thus, interaction between fibres, is no longer neglected.

3

Interacting fibre models

As we have seen in Chapter 2, the existing surrogate models for fibre lay down already describe numerous realistic properties of the physical material. These include coiling due to a coiling potential, the influence of the turbulent airflow, modelled by stochasticity, as well the anisotropic fibre orientation represented by an anisotropic parameter. However, an important property of the real fibres, namely the thickness of the fibres, has not yet been included in the models. So far each fibre has only been represented by a one–dimensional curve in space which actually describes the fibre's centreline. In this chapter we extend the existing surrogate models for fibre lay down to include the thickness of the fibres and the interaction between the fibres.

3.1 The basic two–dimensional model

We derive a model for $N \in \mathbb{N}$ interacting fibres. As in Chapter 2, we describe each fibre by its centreline. In particular, we assume that all the fibres come from the same nozzle and, thus, the origin of our system again represents the nozzle position. In contrast to Chapter 2, we include the effects caused by the thickness of each fibre. This is done by describing the interactions between the fibres at their boundaries. Thus, the equations for the individual fibres are no longer independent. To distinguish between the fibres we introduce an index i for each fibre and denote the fibre position and orientation angle by

$$
\begin{aligned}
x^i &: \mathbb{R}_+ \to \mathbb{R}^2, \\
\alpha^i &: \mathbb{R}_+ \to [0, 2\pi),
\end{aligned}
\tag{3.1}
$$

for $i \in \{1, \ldots, N\}$, respectively. To include the fibre thickness and, thus, the influence of the fibres on each other, we introduce an additional force term. We assume that each fibre is rotationally symmetric around its centreline and that all the fibre cross sections have the same radius denoted by R. When modelling a hard core interaction between two fibres, one would expect a resulting force if the distance between two points on the fibre centrelines is $2R$. The result would be a change in the orientation and, thus, the non–intersection of the fibres. In contrast to the classical case for interacting particles (CERCIGNANI, 1990), we do not simply wish to include the effect of single particles on each other but also to describe

the interaction along the whole fibre curves. Thus, to achieve a meaningful description, we have to include all the fibre paths. We assume that the interaction force is caused by an interaction potential $U : \mathbb{R}^2 \to \mathbb{R}$ depending on the distance of one fibre relative to another. Thus, by extending the basic two–dimensional model given by Equation (2.2), a model for each fibre i is

$$
\mathrm{d}x_t^i = v(\alpha_t^i)\mathrm{d}t,
$$

$$
\mathrm{d}\alpha_t^i = -\nabla V(x_t^i) \cdot v^{\perp}(\alpha_t^i)\mathrm{d}t - \left(\sum_{j=1}^{N} \int_0^t \nabla U(x_t^i - x_s^j)\mathrm{d}s \right) \cdot v^{\perp}(\alpha_t^i)\mathrm{d}t + A\mathrm{d}W_t^i, \tag{3.2}
$$

where the Brownian motions $\left(W_t^i\right)_{t \geq 0}$, $i \in \{1,\dots,N\}$, are assumed to be independent. The sum in Equation (3.2) does not exclude the term $j = i$, as is normally the case for interacting particle systems. In GOLSE (2012) the particular conceptional difficulties of self–interactions in classical electrodynamics were discussed. As we will see in the upcoming sections, an appropriate choice for the interaction potential U prevents both the self–intersection of a fibre and the intersection with other fibres.

Models for interacting particles with time lag with a similar structure to Equation (3.2) have been developed for several applications. The majority of these investigations, in contrast to our model, considered single time lags. In SUN *et al.* (2014) directional switching in a self–propelled particle model with delayed interactions was investigated. In both LIU and WU (2014) and ERBAN *et al.* (2016) the Cucker–Smale model describing the behaviour of a group of fish or birds (CUCKER and SMALE, 2007) with delay was examined. In contrast to LIU and WU (2014), in ERBAN *et al.* (2016) additional noise was considered. A mathematical model for turning delays in swarm robotics was examined in TAYLOR-KING *et al.* (2015). It was found that the predictions from the model with additional delay matched the results from experiments better than in the case without delay. In GOLSE (2012) a regularised Vlasov–Maxwell equation and its derivation from a particle system was performed. This system, as in our case, consists of N coupled integro–differential equations with delay.

3.1.1   The interaction potential

The choice of the interaction potential can have a huge effect on the dynamics of the solution. For a good choice of U we require several properties on U to be fulfilled. The first one is that U decays for large distances

$$
\|U(x)\| \to 0, \text{ as } \|x\| \to \infty.
$$

This guarantees that fibre interactions happen locally. Furthermore, it is required that U depends on the fibre radius R. In addition, as we consider the relative distance of two fibre points for the strength of the interaction, we require the potential U to be symmetric. Even taking these restrictions into account, a large number of options for the potential U exist. We concentrate on a hard core interaction of the fibres which is described by

$$U(x) = c_U \mathscr{H} \left(2R - \|x\| \right),\tag{3.3}$$

where $\mathscr{H}$ is the Heaviside function given by

$$\mathscr{H}(y) = \begin{cases} 0, & \text{for } y < 0, \\ 1/2, & \text{for } y = 0, \\ 1, & \text{for } y > 0. \end{cases}$$

The constant $c_U \geq 0$ accounts for the strength of the interaction force in comparison to the external force caused by V and the Brownian motion. For $c_U = 0$ no interaction takes place. As a consequence, the system described by Equation (3.2) decouples for the individual fibres, as for all the models described in Chapter 2. The gradient of the interaction potential in Equation (3.3) is a Dirac delta distribution at $2R$. This guarantees an intermediate change of the fibre orientation as soon as two fibres come into contact. However, real fibres resulting from the meltspinning process are not rigid bodies but have some degree of flexibility. To allow for this flexibility we use a continuously differentiable function which approximates the interaction potential from Equation (3.3). This is

$$U(x) = c_U \frac{1}{1 + \exp\left(-k \left(1 - \frac{\|x\|^2}{(2R)^2} \right) \right)},\tag{3.4}$$

which is a smooth parameter–dependent potential which coincides with Equation (3.3) for $k \to \infty$. For finite values of k we obtain potentials where the edges are smeared out. As a result, this interaction potential, in contrast to the one defined by Equation (3.3), does not have a compact support for $k < \infty$ and, therefore, implies a change in the fibre orientation even if the fibre distance is larger than $2R$. The gradient of the potential in Equation (3.4) is given by

$$\nabla U(x) = -c_U \frac{2k}{(2R)^2} \frac{x}{\left(\exp\left(\frac{H(x)}{2} \right) + \exp\left(\frac{-H(x)}{2} \right) \right)^2},$$
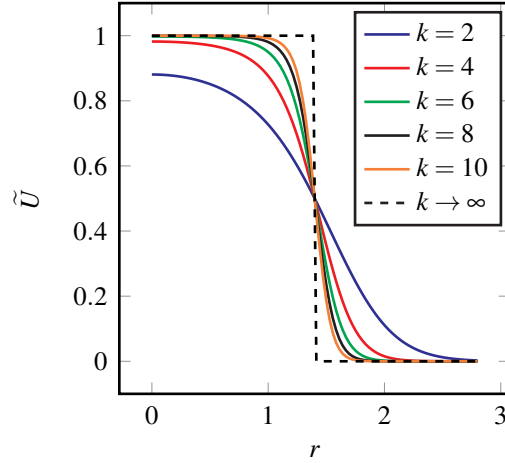
Figure 3.1 – Scalar interaction potential $\widetilde{U}$ given by Equation (3.5) for different values of k. In addition, the dashed line indicates the limit case $k \to \infty$. For all plots we used $R = 0.7$.

where

$$H(x) = k \left(1 - \frac{\|x\|^2}{(2R)^2} \right).$$

In contrast to the gradient of the hard core potential given by Equation (3.3), the gradient of the smooth version, Equation (3.4), is finite for $k < \infty$. Due to the radial symmetry of U given by Equation (3.4), we introduce the scalar version of the interaction potential

$$\widetilde{U} : \mathbb{R} \to \mathbb{R}, \quad \widetilde{U}(r) = c_U \frac{1}{1 + \exp\left(-k \left(1 - \frac{r^2}{(2R)^2} \right) \right)}, \tag{3.5}$$

where $\widetilde{U}(r) = U(\|x\|)$ for $\|x\| = r$. In Figure 3.1 we see the effect of different values of k on the scalar interaction potential $\widetilde{U}$ given by Equation (3.5) along with the limit $k \to \infty$. The larger the value of k, the better Equation (3.4) approximates the hard core potential, Equation (3.3).

3.2 The influence of model parameters

In order to demonstrate the influence of parameter variations on the fibre positions, we now present illustrative solutions of Equation (3.2) using the smoothed Heaviside interaction potential in Equation (3.4) and the standard coiling potential $V = \frac{1}{2}\|x\|^2$. These parameters are the smoothness parameter k, the fibre radius R and the weight for the interaction strength c_U appearing in the interaction potential U, as well as the noise amplitude A. To investigate the different effects for different parameters, we concentrate on a single fibre described by Equation (3.2) with $N = 1$. For all the simulations we use the standard
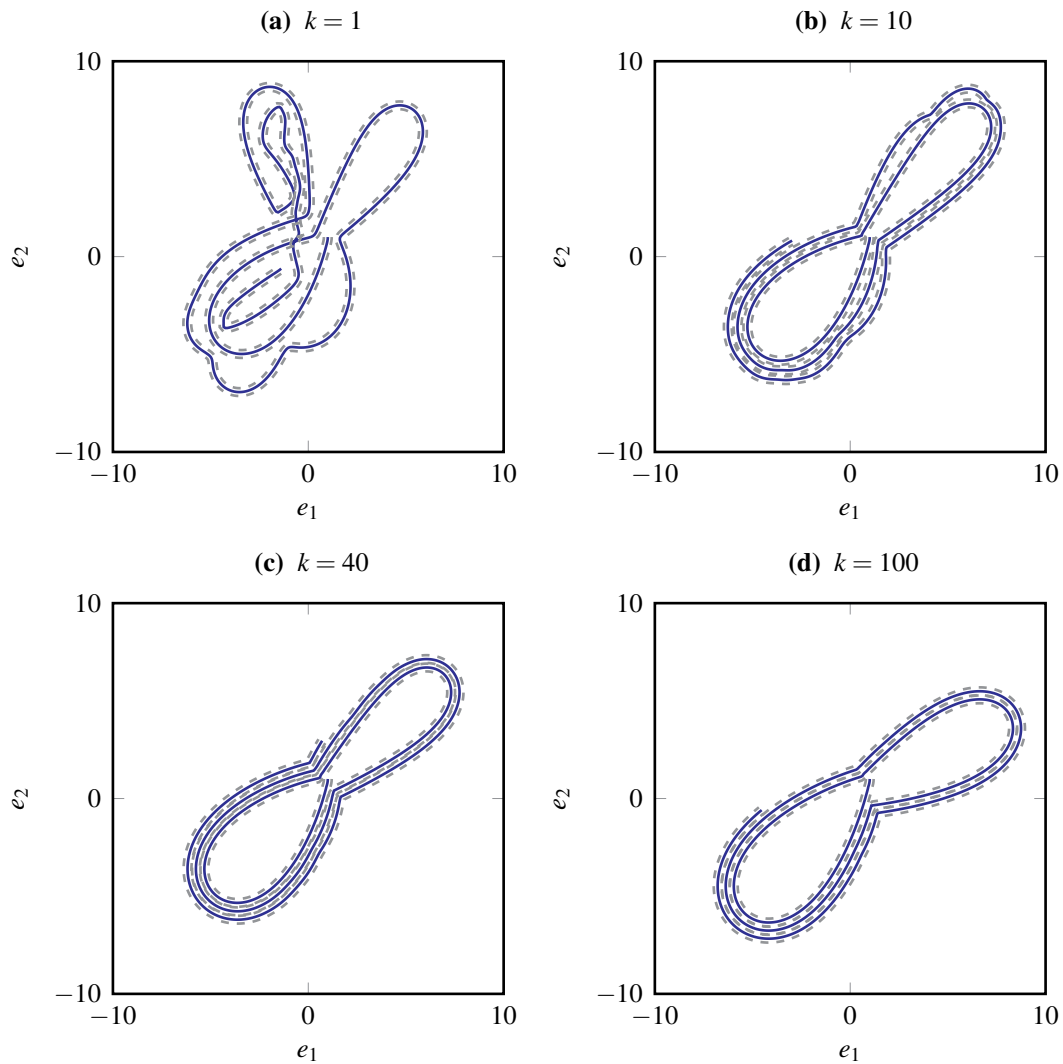
Figure 3.2 – Fibre curves for increasing values of k. The solid blue line indicates the fibre centre line, whereas the dashed lines represent the fibre boundaries. The initial position and orientation are $x_0^1 = (1,1)^T$ and $\alpha_0^1 = 3\pi/2$ respectively. The parameters used for these figures are $A = 0, c_U = 50, R = 0.2, t = 100$.

Euler–Maruyama method (ØKSENDAL, 2003) with constant step size $\Delta t = 0.01$. For more sophisticated methods, see KLOEDEN and PLATEN (1999).

3.2.1 The influence of the smoothness parameter

Figure 3.2 shows the effect of the smoothing parameter k, which appears in the interaction potential, on the solution of Equation (3.2). All other parameters are fixed. In particular, we choose $A = 0$. In all of the figures the continuous lines represent the fibre centre line and the dashed lines represent the fibre boundary, with the shortest distance to the centre line being the fibre radius R, which appears in the interaction potential U given by Equation (3.4). Figure 3.2(a) shows the result for $k = 1$. Comparing the result to the case

without interaction and noise, see Figure 2.1(a), we see that the interaction potential shows some effect on the fibre curve as the regular structure is lost. However, the interaction is not strong enough to prevent self–intersection. Continuing to Figure 3.2(b), we observe that the choice of $k = 10$ is large enough to prevent any obvious self–intersections. The fibre image is as expected. Although the effect of the coiling potential V is to force the fibre back to the origin, the portion of the fibre already laid down prevents this and the fibre movement continues along its own historical trajectory. Following the fibre curve from its initial position, we see that the interaction almost exactly happens where it is supposed to be, namely at the fibre boundary. However, a slight overlap of the fibre boundaries is observed. This effect can be seen by looking closely at the dashed lines representing the fibre boundary. Figures 3.2(c) and 3.2(d), where $k = 40$ and $k = 100$ respectively, show the same qualitative behaviour for the fibre position and for $k = 100$ we see that the fibre boundaries almost perfectly match.

3.2.2 The influence of the fibre radius

Figure 3.3 shows the fibre solution to Equation (3.2) for varying fibre radius R with all other parameters fixed. In particular, we choose $A = 0$. As R increases we observe an increase in the size of the domain occupied by the fibre, with a decrease in the number of loops but no qualitative change in the shape of the fibre.

3.2.3 The influence of the interaction strength

Now we demonstrate the effect of increasing c_U, the parameter describing the interaction strength, on the solution of Equation (3.2) with all the other parameters fixed. In particular, we choose $A = 0$. Results are shown in Figure 3.4, and it is obvious that changing the size of c_U has a big effect on the fibre shape. In Figure 3.4(a), with $c_U = 1$, we see that the fibre self–intersects in many places. This implies that when c_U is small, intersections cannot be prevented. However, the interaction potential obviously has an effect on the fibre movement, which can be seen by comparing the latter figure to Figure 2.1(a) in the case without interaction and $A = 0$. The fibre in Figure 3.4(b), with $c_U = 10$, has no self-intersections. In Figure 3.4(c), where $c_U = 30$, the overall domain occupied by the fibre increases and the shape changes when compared to Figure 3.4(b). The domain occupied by the fibre increases even more for $c_U = 50$ as the influence of the external potential V becomes even smaller.

3.2.4 The influence of noise

To investigate the effect of noise on the fibre shape, we now examine solutions of Equation (3.2), shown in Figure 3.5, for varying A. All other parameters remain fixed. For

Figure 3.3 – Fibre curves with different radii R. The solid line indicates the fibre centre line, whereas the dashed lines indicate the fibre boundary. The initial position and orientation are $x_0^1 = (1,1)^T$ and $\alpha_0^1 = 3\pi/2$ respectively. The parameters used for these figures are $A = 0$, $k = 100$, $c_U = 50$, $t = 100$.
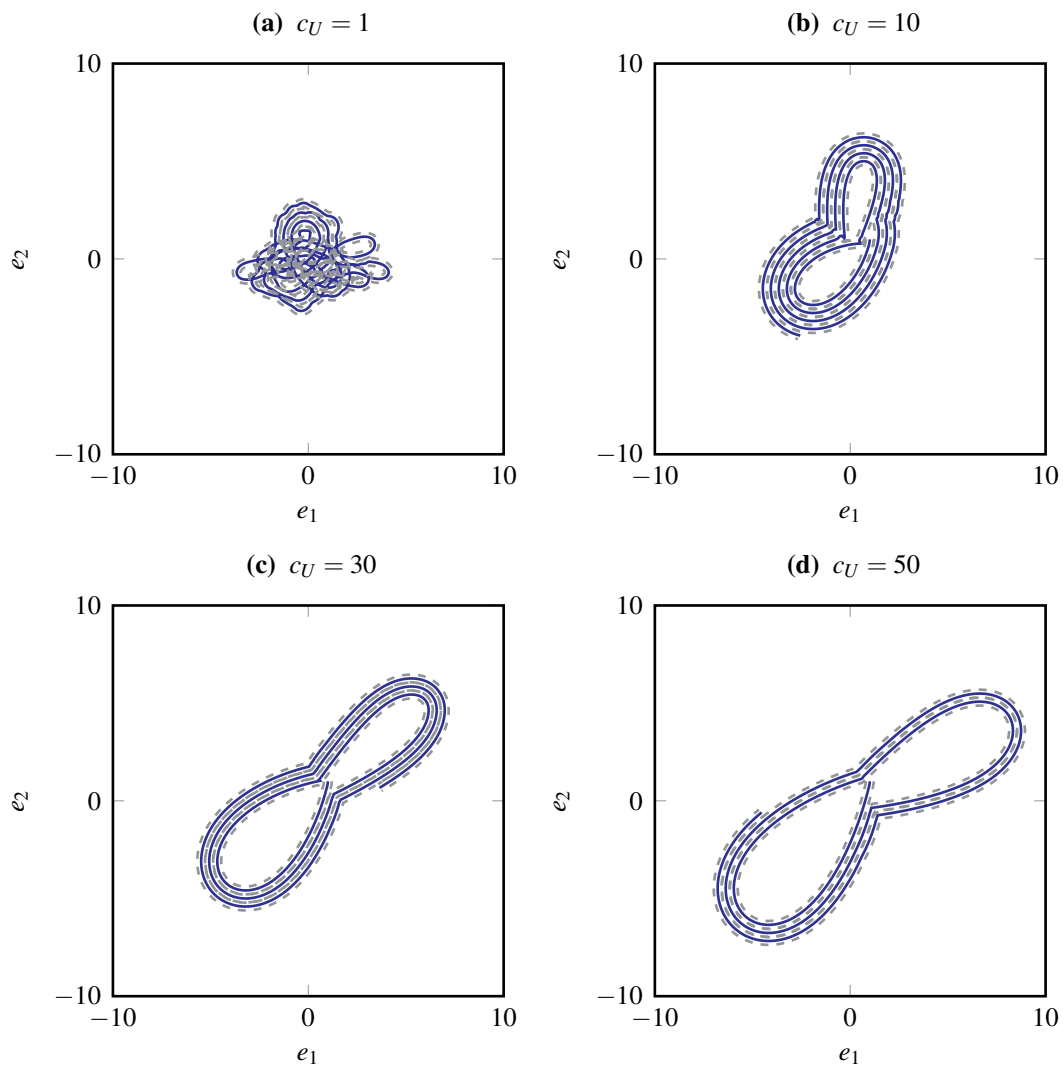
Figure 3.4 – Fibre curves for different values c_U. The initial position and orientation are $x_0^1 = (1,1)^T$ and $\alpha_0^1 = 3\pi/2$ respectively. The other parameters used for these figures are $A = 0, k = 100, R = 0.2, t = 100$.
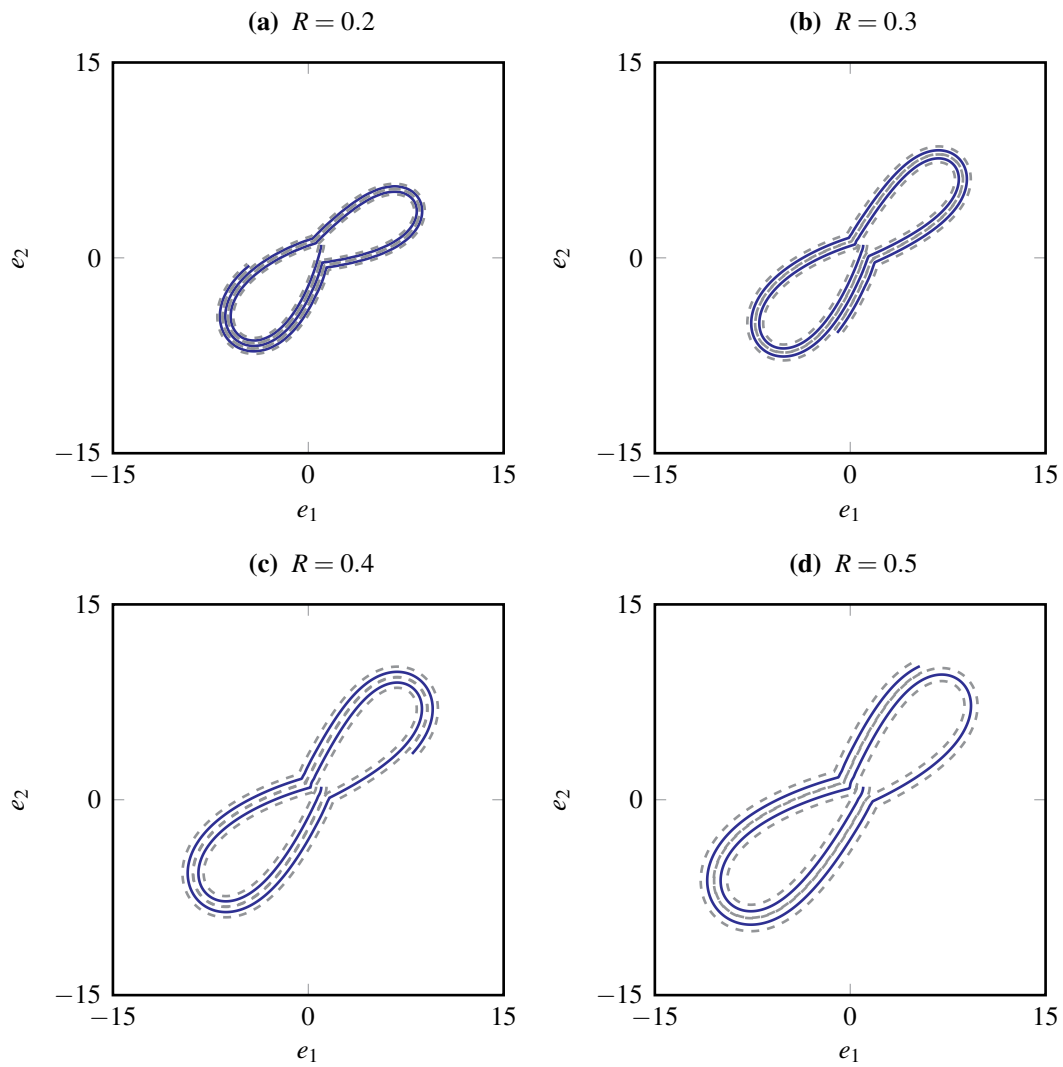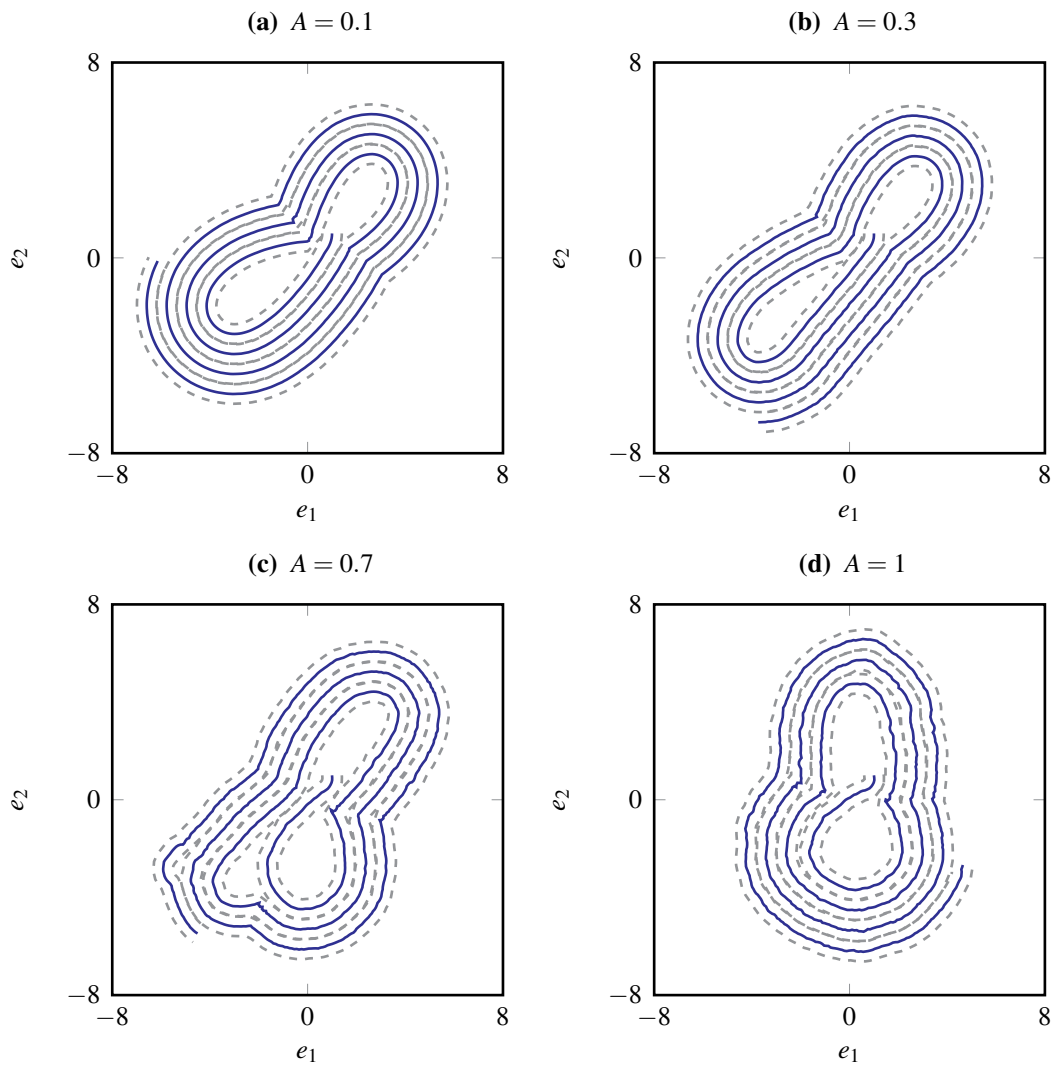
Figure 3.5 – Fibre curves for different values A. The solid blue line indicates the fibre centre line, whereas the dashed lines indicate the fibre boundaries. The initial position and orientation are $x_0^1 = (1,1)^T$ and $\alpha_0^1 = 3\pi/2$ respectively. The parameters used for these figures are $k = 100, c_U = 10, R = 0.4, t = 100$.

all the numerical simulations we use the same random numbers in the Euler–Maruyama scheme.

Comparing Figures 3.5(a) and 3.5(b) it is interesting to see that the increase in noise has hardly any effect on the fibre image. However, for even larger values of A, see Figures 3.5(c) and 3.5(d), a marked change in the fibre image compared may be observed, when compared to Figures 3.5(a) and 3.5(b). Firstly, the orientation of the fibre changes from clockwise in Figures 3.5(a) and 3.5(b) to counter–clockwise in Figures 3.5(c) and 3.5(d). This effect can be explained by small variations in the orientation angle at the beginning of the simulation due to the stochastic effects. Secondly, the fibre curves in Figures 3.5(c) and 3.5(d) do not look very smooth compared to Figures 3.5(a) and 3.5(b), as expected for large noise amplitudes A.

We have seen that the model strongly depends on the various parameters and that for strong enough interaction c_U and large enough k, it is possible to prevent fibre intersections.

3.3   Extensions of the two–dimensional model

In Section 3.1 we have seen that it is possible to include the thickness of the fibres in the standard two–dimensional model given by Equation (2.2) which results in a large system of coupled stochastic differential equations with time lag described by Equation (3.2). First numerical experiments in Section 3.2 have illustrated that the required non–intersection can be achieved with the correct choice of model parameters and the fibre thickness can be represented appropriately. In this section we show how the belt movement can be incorporated into the model.

3.3.1   A model with belt movement

As in Chapter 2, in the case without interaction, the belt movement plays an important role for a realistic description of the fibre lay down. To include the effect of the belt movement, we consider, as in the case without interaction, a reference curve γ. Here we assume that all the fibres have the same production speed and, thus, we can use the same reference curve throughout. As we want the fibre curve to follow the reference curve γ, we modify the basic fibre model with interaction given by Equation (3.2) and consider the following equations

$$\mathrm{d}\eta_t^i = v(\alpha_t^i)\mathrm{d}t,$$

$$\mathrm{d}\alpha_t^i = -\left(\nabla V(\eta_t^i - \gamma_t) + \left(\sum_{j=1}^{N}\int_0^t \nabla U(x_t^i - x_s^j)\mathrm{d}s\right)\cdot v^\perp(\alpha_t^i)\right)\mathrm{d}t + A\mathrm{d}W_t^i. \tag{3.6}$$

The actual position of fibre i is denoted by η^i. We see that the interaction term remains unchanged when compared to the case without belt movement. To consider the deviation of the actual fibre positions from the reference curve, we consider $x^i = \eta^i - \gamma$. The corresponding equations are then given by

$$
\begin{aligned}
\mathrm{d}x_t^i &= v(\alpha_t^i)\mathrm{d}t - \mathrm{d}\gamma_t, \\
\mathrm{d}\alpha_t^i &= -\left(\nabla V(x_t^i) + \left(\sum_{j=1}^{N}\int_0^t \nabla U(x_t^i - x_s^j + \gamma_t - \gamma_s)\mathrm{d}s\right)\cdot v^\perp(\alpha_t^i)\right)\mathrm{d}t + A\mathrm{d}W_t^i.
\end{aligned}
\tag{3.7}
$$

We note that the reference curve γ with its complete history also appears in the interaction term.

To examine the effect of the belt movement on the fibre shape, in Figure 3.6 we present illustrative results with $N = 2$ and the belt function as defined by Equation (2.8) with varying speed ratios ψ. As the ratio of belt to production speed ψ increases, the effect of the belt movement dominates that of the coiling potential V and the fibres become stretched out and less coiled. In all cases we can see that due to the interaction potential U the fibres do not intersect.

3.3.2 The delay length

In the previous section we have seen that including the fibre interaction over the whole length of the fibres can be achieved by introducing an interaction potential and delay integral over the full history. However, the full length of the fibre will not always influence the portion of the fibre currently being laid down. Only the material in the immediate vicinity of the lay down area, which has not already been transported away by the belt, needs to be considered. This can also be seen in Figures 3.6(c) and 3.6(d) where the fibres are stretched out rather than tightly coiled due to the dominating effect of the belt movement. Therefore, a legitimate assumption is to include only a fixed length of the fibre history to include all interactions. Thus, we introduce a finite delay length $H > 0$ on which fibre interactions are relevant. However, when the first fibre material is produced and laid down on the belt, all of the current fibre material plays a role for interactions and, therefore, should be considered. This can be realised by introducing a delay function h_H depending on H which is defined by

$$
h_H(t) = \begin{cases} t, & \text{for } t \leq H, \\ H, & \text{for } t > H. \end{cases}
\tag{3.8}
$$
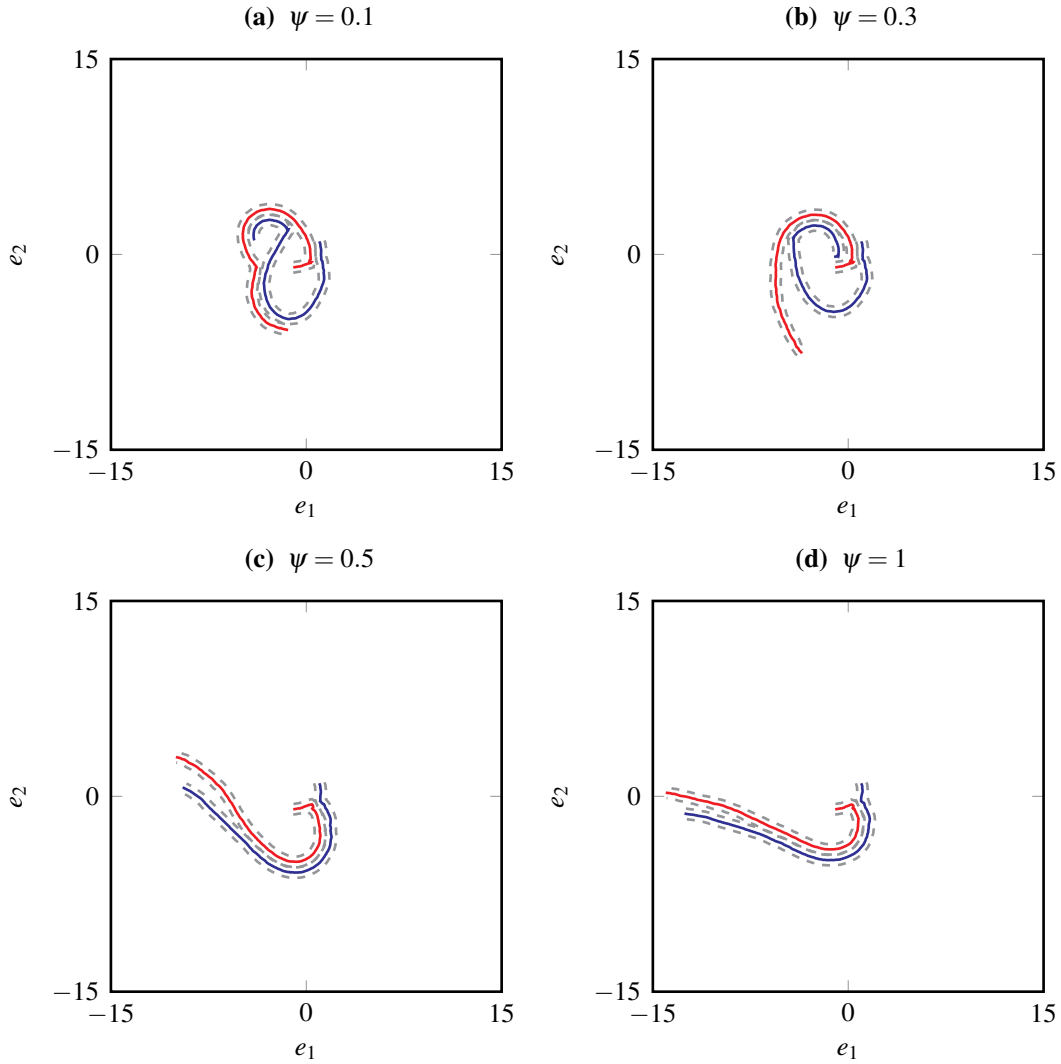
Figure 3.6 – Two interacting fibres with belt movement, solutions of Equation (3.7), with length $t = 100$ and for different speed ratios ψ for the reference curve γ defined by Equation (2.8). The solid blue and red lines represent the centre lines of two single fibres, whereas the dashed lines represent the fibres boundary. The initial positions are $x_0^1 = (1,1)^T$ and $x_0^2 = (-1,-1)^T$ respectively. The initial orientations are $\alpha_0^1 = 3\pi/2$ and $\alpha_0^2 = 0$. The parameters used for these figures are $A = 1, k = 100, c_U = 20, R = 0.4, t = 20$.

Then, the model described by Equation (3.6) changes to

$$d\eta_t^i = v(\alpha_t^i)dt,$$

$$d\alpha_t^i = -\left(\nabla V(\eta_t^i - \gamma_t) + \left(\sum_{j=1}^{N}\int_{t-h_H(t)}^{t}\nabla U(x_t^i - x_s^j)ds\right)\cdot v^\perp(\alpha_t^i)\right)dt + A dW_t^i, \quad (3.9)$$

or for the relative fibre position x^i

$$dx_t^i = v(\alpha_t^i)dt - d\gamma_t,$$

$$d\alpha_t^i = -\left(\nabla V(x_t^i) + \left(\sum_{j=1}^{N}\int_{t-h_H(t)}^{t}\nabla U(x_t^i - x_s^j + \gamma_t - \gamma_s)ds\right)\cdot v^\perp(\alpha_t^i)\right)dt + A dW_t^i.$$

$$(3.10)$$

As $H \to \infty$ we obtain the full interaction case again, Equations (3.6) and (3.7).

We motivated the introduction of a finite delay length by the belt movement. Nevertheless, it can also be interesting to see how the delay length influences the fibre behaviour in the basic model without belt movement given by Equation (3.2). Thus, we also consider the basic model for interacting fibres with finite delay given by

$$dx_t^i = v(\alpha_t^i)dt,$$

$$d\alpha_t^i = -\nabla V(x_t^i)\cdot v^\perp(\alpha_t^i)dt - \left(\sum_{j=1}^{N}\int_{t-h_H(t)}^{t}\nabla U(x_t^i - x_s^j)ds\right)\cdot v^\perp(\alpha_t^i)dt + A dW_t^i. \quad (3.11)$$

This formulation is a generalisation of Equation (3.2) and both models coincide for $H \to \infty$.

3.4   Models in higher dimensions

In Chapter 2 we have seen that multiple extensions of the models without interaction in two space dimensions exist. In particular, we discussed three–dimensional models and models with an anisotropic orientation distribution. We now apply the strategy presented in Section 3.1 to these model extensions and include the fibre thickness. Afterwards, we present illustrative examples.

3.4.1   The basic model in arbitrary dimensions

It is possible to derive a formulation in arbitrary dimension $d \geq 2$ with interaction, as done for the case without interaction in Chapter 2. We denote the position and orientation of the

i–th fibre, $i \in \{1, \ldots, N\}$, by

$$x^i : \mathbb{R}_+ \to \mathbb{R}^d,$$
$$v^i : \mathbb{R}_+ \to \mathbb{S}^{d-1}, \tag{3.12}$$

and, in addition, use the d–dimensional versions for the potentials $V : \mathbb{R}^d \to \mathbb{R}$, $U : \mathbb{R}^d \to \mathbb{R}$. Then, we describe the fibre paths by the following system of coupled stochastic differential delay equations

$$\mathrm{d}x_t^i = v_t^i \mathrm{d}t,$$

$$\mathrm{d}v_t^i = \left(I - v_t^i \otimes v_t^i\right) \circ \left(-\frac{1}{d-1}\nabla V(x_t^i)\mathrm{d}t - \frac{1}{d-1}\left(\sum_{j=1}^{N} \int_{t-h_H(t)}^{t} \nabla U(x_t^i - x_s^j)\mathrm{d}s\right)\mathrm{d}t + A\mathrm{d}W_t^i\right),$$

$$\tag{3.13}$$

where $\left(W_t^i\right)_{t \geq 0}$ denote independent d–dimensional Brownian motions and $(x^i, v^i) \in \mathbb{M}^d$. Sometimes it is more convenient to use the Itô formulation of Equation (3.13) which is

$$\mathrm{d}x_t^i = v_t^i \mathrm{d}t,$$

$$\mathrm{d}v_t^i = -\left(I - v_t^i \otimes v_t^i\right)\left(\frac{1}{d-1}\nabla V(x_t^i)\mathrm{d}t + \frac{1}{d-1}\left(\sum_{j=1}^{N} \int_{t-h_H(t)}^{t} \nabla U(x_t^i - x_s^j)\mathrm{d}s\right)\right) \tag{3.14}$$

$$-\frac{d-1}{2}A^2 v_t^i \mathrm{d}t + A\left(I - v_t^i \otimes v_t^i\right)\mathrm{d}W_t^i.$$

For $d = 2$ we retrieve the two–dimensional interacting fibre model described by Equation (3.2), but now with the variables (x^i, v^i) with the orientation vector instead of (x^i, α^i) with the orientation angle.

For $d = 3$ we have the interacting fibre model for three space dimensions. In Figure 3.7 we can see example solutions of Equation (3.14) for $N = 2$ in three dimensions with varying noise A. In all the four cases we can see that interaction takes place.

3.4.2   The anisotropic model

The cases of particular interest in terms of applications are $d = 2$ and $d = 3$. The former describes planar lay down and the latter isotropic lay down in all three space directions. As in the case without interaction in Chapter 2, it would be interesting to include the anisotropic behaviour in the angular distribution. To achieve this we consider the anisotropic model without interaction, Equation (2.26), for each fibre and, following the same strategy as in the isotropic case with interaction, we add the interaction term to the external potential

(a) $A = 0$

(b) $A = 0.1$

(c) $A = 0.5$

(d) $A = 1$

Figure 3.7 – Two interacting fibres, solutions of Equation (3.14) for $d = 3$, with length $t = 100$ and for different noise amplitudes A. The blue and red lines represent single fibres with the initial positions $x_0^1 = (-6, 0, 0)^T$ and $x_0^2 = (0, -0.1, -1)^T$ and initial orientations $v_0^1 = (1, 0, 0)^T$ and $v_0^2 = (0, 0, 1)^T$ respectively. The parameters used for these figures are $k = 100, c_U = 10, R = 0.4$.

which leads to

$$
\mathrm{d}x_t^i = v_t^i \mathrm{d}t,
$$

$$
\sin \theta_t^i \mathrm{d}\alpha_t^i = -\frac{1}{B+1} \left(\nabla V(x_t^i) + \left(\sum_{j=1}^N \int_{t-h_H(t)}^t \nabla U(x_t^i - x_s^j) \mathrm{d}s \right) \right) \cdot n_{1,t}^i \mathrm{d}t + A \mathrm{d}W_{t,1}^i,
$$

$$
\mathrm{d}\theta_t^i = -\frac{B}{B+1} \left(\nabla V(x_t^i) + \left(\sum_{j=1}^N \int_{t-h_H(t)}^t \nabla U(x_t^i - x_s^j) \mathrm{d}s \right) \right) \cdot n_{2,t}^i \mathrm{d}t,
$$

$$
+ \frac{1}{2} A^2 \cot \theta_t^i \mathrm{d}t + \sqrt{B} A \mathrm{d}W_{t,2}^i.
$$

$$(3.15)$$

where $v^i = v(\alpha^i, \theta^i)$, $n_1^i = n_1(\alpha^i, \theta^i)$ and $n_2^i = n_2(\alpha^i, \theta^i)$. Here $\left(W_{t,1}^i \right)_{t \geq 0}$ and $\left(W_{t,2}^i \right)_{t \geq 0}$ are independent one–dimensional Brownian motions. The system inherits the geometrical properties of the non–interacting case in the small B limit, see Section 2.2.3. This can be seen easily when setting $B = 0$ and denoting the third component of the fibre position x^i by $x_{\cdot,3}^i$ which leads to

$$x_{t,3}^i = \cos \theta_t^i \mathrm{d}t,$$
$$\theta_t^i = \frac{1}{2} A^2 \cot \theta_t^i,$$

for all $i \in \{1, \ldots, N\}$ independently. As for the case without interaction, we obtain the explicit solution

$$\theta_t^i = \arccos \left(\exp \left(-\frac{1}{2} A^2 t \right) \cos \theta_0^i \right),$$
$$x_{t,3}^i = x_{0,3}^i + \frac{2}{A^2} \exp \left(-\frac{1}{2} A^2 t \right) \cos \theta_0^i.$$

To recover a two–dimensional solution, we make the choice for the initial conditions of $\theta_0^i = \frac{\pi}{2}$. This yields $\theta_t^i = \frac{\pi}{2}$ and $x_{t,3}^i = x_{0,3}^i$. In Figure 3.8 we give examples for solutions of Equation (3.15) for $N = 2$ using different B. For $B \to 0$ we can see that the fibre images become more planar. Nevertheless, intersection is avoided.

3.5 Summary

In this chapter we have introduced a novel model for fibre lay down which includes the effects of the fibre thickness. This is achieved by including interactions between the fibres and can, in suitable parameter regimes, prevent unphysical intersections of the fibres. We have shown how to incorporate the interaction into several of the SDE models presented in Chapter 2 by introducing interaction potentials along the whole of the fibre length. To represent the movement of a belt, we extended this approach to only include a finite delay length for the fibre interaction. Furthermore, we were able to include the effect of fibre thickness in the anisotropic fibre model as well. To sum up, we achieved an extension of the model hierarchy which allows for a more detailed description due to the interaction introduced.

In the next chapter we will discuss macroscopic equations for interacting fibres based on the SDE models presented in this chapter and discuss the characteristic behaviour for many long interacting fibres.
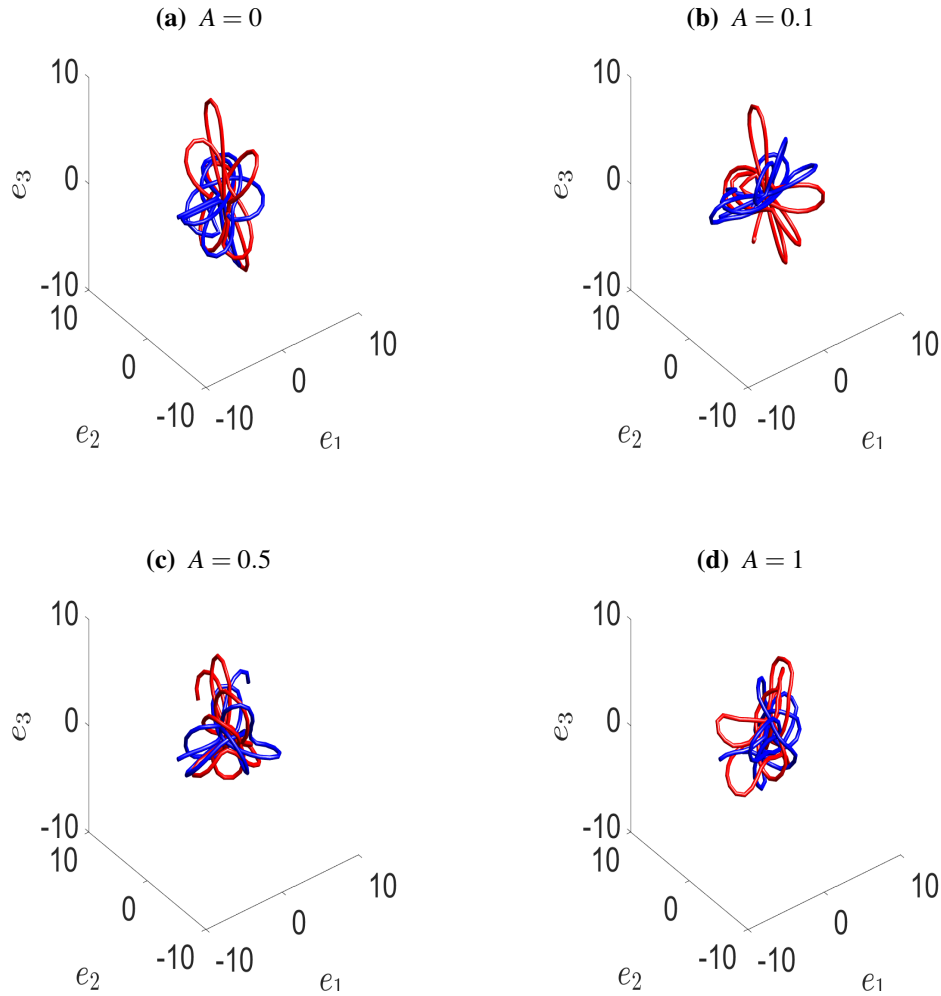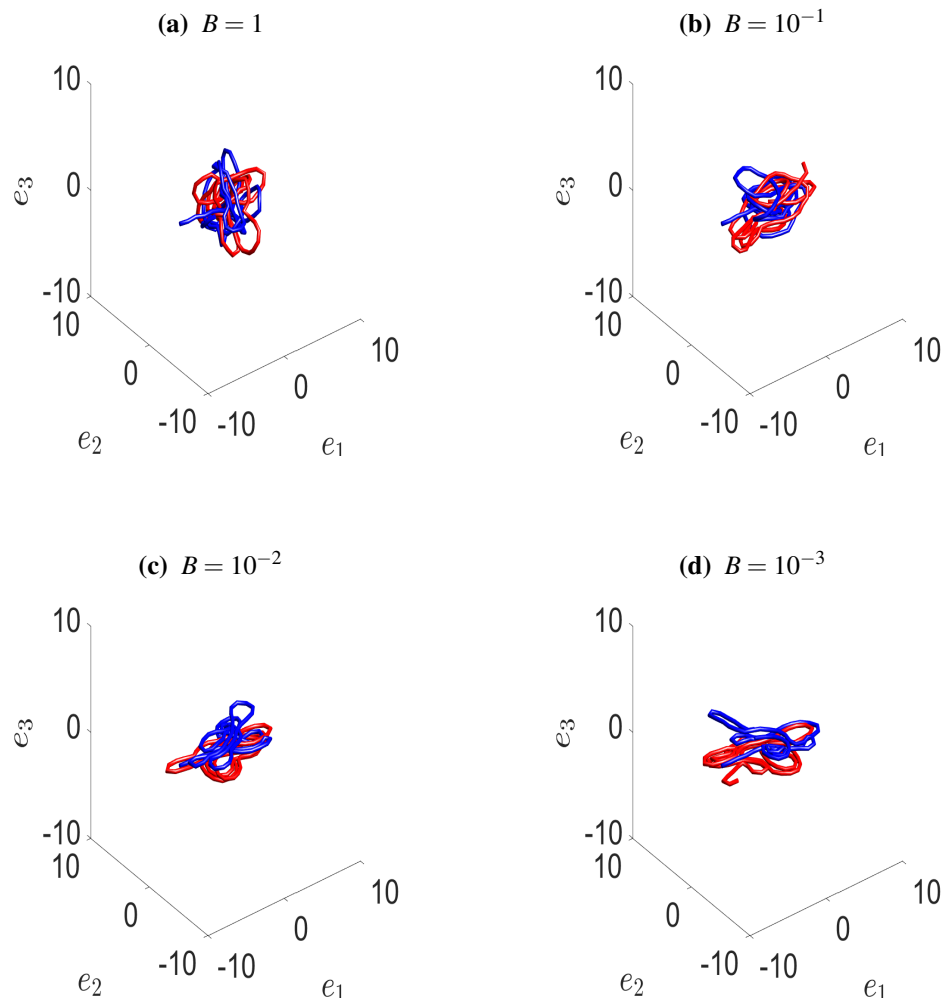
Figure 3.8 – Two interacting fibres, solutions of Equation (3.15), with length $t = 100$ and for different anisotropy parameters B. The blue and red lines represent single fibres with the initial positions $x_0^1 = (-6, 0, 0)^T$ and $x_0^2 = (0, -0.1, -1)^T$ and initial orientations $v_0^1 = (1, 0, 0)^T$ and $v_0^2 = (0, 0, 1)^T$ respectively. The fibre radius R used for the numerical simulations is the same as the one used in the interaction potential. The parameters used for these figures are $A = 1, k = 100, c_U = 5, R = 0.4$.

4   The long–time behaviour

In many physical systems the long–time behaviour plays an important role. In particular, an analysis of the stationary states and the convergence to these states can give an insight into the dynamics of the system and its dependence on the modelling parameters. The convergence to a stationary state plays a particularly important role for us as the long–time behaviour corresponds to the case of very long fibres, as is the case in the industrial production process.

We begin by describing a macroscopic equation for many interacting fibres, before we derive a diffusion approximation. Then, we analyse the convergence to equilibrium from an analytical point of view. Finally, we solve the diffusion approximation numerically to give a further insight into the long–time behaviour of the system and its dependence on the various modelling parameters involved. In particular, we show how the interaction term and the delay influence the fibre distribution and the convergence to an equilibrium state.

4.1   Macroscopic equations

As many fibres are necessary for the production of a non–woven material, the limit $N \to \infty$ is of particular interest for us. Before we can begin to give a statistical description of the fibre position and orientation for many long fibres, we have to adapt the isotropic model given by Equation (3.14) slightly. By scaling the interaction term with the number of fibres N, we guarantee that the interaction term is kept to order one for arbitrary N. This scaling is known as the *weak–coupling scaling*. For more details, see BRAUN and HEPP (1977), DOBRUSHIN (1979), SPOHN (1991), GOLSE (2003), J. A. CARRILLO, D'ORSOGNA, *et al.* (2009), BOLLEY, GUILLIN, *et al.* (2010), and GOLSE (2016). In a similar manner we also scale the time integral by a factor $1/h_H(t)$. This keeps the interaction part to order one for increasing t. Both scalings together allow for the analysis of the case of many long

fibres. Overall, the scaled interacting fibre system is given by

$$
\mathrm{d}x_t^i = v_t^i \mathrm{d}t,
$$

$$
\mathrm{d}v_t^i = -\left(I - v_t^i \otimes v_t^i\right)\left(\frac{1}{d-1}\nabla V(x_t^i)\mathrm{d}t + \frac{1}{d-1}\left(\frac{1}{N}\sum_{j=1}^{N}\frac{1}{h_H(t)}\int_{t-h_H(t)}^{t}\nabla U(x_t^i - x_s^j)\mathrm{d}s\right)\right)
$$

$$
- \frac{d-1}{2}A^2 v_t^i \mathrm{d}t + A\left(I - v_t^i \otimes v_t^i\right)\mathrm{d}W_t^i.
$$

$$(4.1)$$

Taking the limit $H \to 0$ leads to a non–retarded system with endpoint interaction

$$
\mathrm{d}x_t^i = v_t^i \mathrm{d}t,
$$

$$
\mathrm{d}v_t^i = -\left(I - v_t^i \otimes v_t^i\right)\left(\frac{1}{d-1}\nabla V(x_t^i)\mathrm{d}t + \frac{1}{d-1}\left(\frac{1}{N}\sum_{j=1}^{N}\nabla U(x_t^i - x_t^j)\right)\right)
$$

$$
- \frac{d-1}{2}A^2 v_t^i \mathrm{d}t + A\left(I - v_t^i \otimes v_t^i\right)\mathrm{d}W_t^i.
$$

$$(4.2)$$

In contrast, as $H \to \infty$, we have $h_H(t) = t$ and, therefore, obtain the scaled retarded system on the whole fibre length

$$
\mathrm{d}x_t^i = v_t^i \mathrm{d}t,
$$

$$
\mathrm{d}v_t^i = -\left(I - v_t^i \otimes v_t^i\right)\left(\frac{1}{d-1}\nabla V(x_t^i)\mathrm{d}t + \frac{1}{d-1}\left(\frac{1}{N}\sum_{j=1}^{N}\frac{1}{t}\int_{0}^{t}\nabla U(x_t^i - x_s^j)\mathrm{d}s\right)\right)
$$

$$
- \frac{d-1}{2}A^2 v_t^i \mathrm{d}t + A\left(I - v_t^i \otimes v_t^i\right)\mathrm{d}W_t^i.
$$

$$(4.3)$$

4.1.1   The mean–field equation

The system in Equation (4.1) describes the single fibre paths in detail. However, this description has several disadvantages. Firstly, the long–time behaviour of the system is not immediately clear and numerical simulations become cumbersome and inefficient for large N. Secondly, in our case with delay, it is also necessary to compute the interactions along a part of, or even along the whole of, the fibre history for every single fibre. Finally, one is often not interested in the properties of each single fibre, but in how a system containing many fibres behaves.

To analyse the behaviour of an ensemble of many interacting particles, a classical approach is to consider the joint probability density. In the following we consider the evolution of the (probability–) density

$$
f : \mathbb{R}_+ \times \mathbb{M}^d \to \mathbb{R},
$$

where $f(t,x,v)$ can be interpreted as the probability of finding a fibre point with arc–length t, position x and orientation v. We refer to

$$\rho(t,x) = \int_{\mathbb{S}^{d-1}} f(t,x,v) \, \mathrm{d}v,$$

as the *spatial density*. With $\mathrm{d}v$ we denote the normalised surface measure on $\mathbb{S}^{d-1}$

$$\int_{\mathbb{S}^{d-1}} \mathrm{d}v = 1.$$

We assume that the normalisation

$$\int_{\mathbb{M}^d} f(t,x,v) \, \mathrm{d}\mu = \int_{\mathbb{R}^d} \rho(t,x) \, \mathrm{d}x = 1, \tag{4.4}$$

holds, where $\mathrm{d}\mu = \mathrm{d}v \, \mathrm{d}x$, with $\mathrm{d}x$ being the Lebesgue measure on $\mathbb{R}^d$.

We introduce ∇_x, ∇_v and Δ_v to describe the gradient on $\mathbb{R}^d$, the gradient and the Laplace–Beltrami operator on $\mathbb{S}^{d-1}$ respectively. With this notation, the *mean–field equation* (BRAUN and HEPP, 1977; DOBRUSHIN, 1979; GOLSE, 2003; GOLSE, 2016; BOLLEY, CANIZO, *et al.*, 2011) for the general isotropic case can be written as (BORSCHE *et al.*, submitted)

$$\partial_t f + v \cdot \nabla_x f + Sf = \frac{A^2}{2} \Delta_v f, \tag{4.5}$$

with force term $S = S^V + S^U$ defined by

$$S^V f(t,x,v) = -\frac{1}{d-1} \nabla_v \cdot \left(f(t,x,v)\,(I - v \otimes v)\, \nabla_x V \right),$$

$$S^U f(t,x,v) = \tag{4.6}$$

$$-\frac{1}{d-1} \nabla_v \cdot \left(f(t,x,v)\,(I - v \otimes v)\, \frac{1}{h_H(t)} \int_{t-h_H(t)}^{t} \int_{\mathbb{R}^d} \nabla_x U(x-y)\rho(s,y) \, \mathrm{d}y \, \mathrm{d}s \right).$$

In Equation (4.6) the force terms S^V and S^U represent transport due to the external potential V and the interaction potential U respectively. We make the assumption that our initial condition is given by $f_0(x,v) = f(0,x,v)$. We note that, for $c_U = 0$ in the interaction potential U, we obtain the description of non–interacting fibres. See Chapter 2 for the cases in two and three dimensions. The term

$$\frac{1}{h_H(t)} \int_{t-h_H(t)}^{t} \int_{\mathbb{R}^d} \nabla_x U(x-y)\rho(s,y) \, \mathrm{d}y \, \mathrm{d}s, \tag{4.7}$$

in Equation (4.6) can also be interpreted as the convolution $\nabla_x U \star \bar{\rho}(t,x)$ of $\nabla_x U$ and the

time average of ρ which is defined by

$$\bar{\rho}(t,x) := \frac{1}{h_H(t)} \int_{t-h_H(t)}^{t} \rho(s,x) \, \mathrm{d}s.$$

We are particularly interested in the case of long interacting fibres and their spatial distribution which is given by the stationary solution of Equation (4.5) which can be found by considering a time–independent solution. As we are interested in the spatial distribution, we seek solutions independent of the orientation v which leads to

$$\rho \nabla_x (\ln \rho + V + U \star \rho) = 0.$$

This then leads to the integral equation

$$\ln \rho + V + U \star \rho = \mathrm{const},$$

where the constant is determined by the normalisation condition for ρ given in Equation (4.4). The equivalent fixed–point form is given by

$$\rho = \frac{\exp(-V - U \star \rho)}{\displaystyle\int_{\mathbb{R}^d} \exp(-V - U \star \rho) \, \mathrm{d}x}, \tag{4.8}$$

and we see that the stationary solution is only given implicitly. In addition, uniqueness and existence are not guaranteed. Furthermore, Equation (4.8) does not give any information about the evolution of the spatial density ρ and the influence of the parameters involved in the model for the convergence towards a stationary solution.

4.1.2 The diffusion approximation

To obtain an evolution equation for the spatial density ρ, we now derive a simplified version of the mean–field equation given by Equation (4.5). This is done by performing a *large diffusion scaling*. In this case the diffusion with respect to the orientation variable dominates. In terms of the fibre production process, this case corresponds to large turbulences due to the air stream. This leads to the *diffusion approximation*, which describes the evolution of the spatial density ρ independent of the orientation variable v. A clear discussion of different possible scalings, in addition to the large diffusion scaling, can be found in HILLEN and PAINTER (2013) where several scalings and their advantages and disadvantages in different settings are discussed.

We consider large values for the noise amplitude A on a diffusive time scale. Thus, we perform a change of variables $\widetilde{A} = \sqrt{\varepsilon} A$, $\widetilde{t} = \varepsilon t$, where $0 < \varepsilon \ll 1$. Substitution into

Equation (4.5), multiplication by ε and omitting the tilde notation results in

$$\varepsilon^2 \partial_t f + \varepsilon v \cdot \nabla_x f + \varepsilon S f = \frac{A^2}{2} \Delta_v f. \tag{4.9}$$

Substituting the Hilbert expansion $f = f^{(0)} + \varepsilon f^{(1)} + \dots$ (CERCIGNANI, 1990) into Equation (4.9) and examining terms with equal powers of ε gives $f^{(0)}(t,x,v) = \rho(t,x)$ to zero order. To first order in ε we obtain

$$v \cdot \nabla_x f^{(0)} + S f^{(0)} = \frac{A^2}{2} \Delta_v f^{(1)}.$$

This has the solution

$$f^{(1)}(t,x,v) = -\frac{2}{A^2(d-1)} v \cdot f^{(0)}(t,x) \nabla_x \left(\ln f^{(0)}(t,x) + V(x) + U \star \bar{\rho}(t,x) \right). \tag{4.10}$$

As we still have the two unknowns, $f^{(0)}$ and $f^{(1)}$, but only one equation, we integrate Equation (4.9) by $\mathrm{d}v$ to obtain

$$\varepsilon \partial_t \int_{\mathbb{S}^{d-1}} f(t,x,v) \, \mathrm{d}v + \nabla_x \cdot \int_{\mathbb{S}^{d-1}} v f(t,x,v) \, \mathrm{d}v = 0.$$

Substitution of the Hilbert expansion into the latter equation and the comparison of terms of first order in ε yields

$$\partial_t f^{(0)} + \nabla_x \cdot \int_{\mathbb{S}^{d-1}} v f^{(1)} \, \mathrm{d}v = 0.$$

Substitution of $f^{(1)}$ from Equation (4.10) gives

$$\partial_t \rho(t,x) - \nabla_x \cdot \int_{\mathbb{S}^{d-1}} v \otimes v \, \mathrm{d}v \frac{2}{A^2(d-1)} \rho(t,x) \nabla_x \left(\ln \rho(t,x) + V(x) + U \star \bar{\rho}(t,x) \right) = 0.$$

Application of the relationship $\int_{\mathbb{S}^{d-1}} v \otimes v \, \mathrm{d}v = \frac{1}{d} I$, (HILLEN, 2005; HILLEN and PAINTER, 2013) yields

$$\partial_t \rho = \frac{2}{d(d-1)A^2} \nabla_x \cdot \left[\rho \nabla_x \left(\ln \rho + V + U \star \bar{\rho} \right) \right].$$

Note that this equation is purely dependent on time and space and no longer on the orientation v. This equation can be rewritten as

$$\partial_t \rho = \frac{2}{d(d-1)A^2} \left[\Delta_x \rho + \nabla_x \cdot \left(\rho \left[\nabla_x V + \nabla_x U \star \bar{\rho} \right] \right) \right], \tag{4.11}$$

where Δ_x denotes the Laplace operator on $\mathbb{R}^d$. This is an advection–diffusion equation. By introducing a new time scale $\hat{t} = Ct$ with

$$C := \frac{2}{d(d-1)A^2},$$

and dropping the caret notation, we end up with

$$\partial_t \rho = \Delta_x \rho + \nabla_x \cdot (\rho\,[\nabla_x V + \nabla_x U \star \bar{\rho}]). \qquad (4.12)$$

This shows that the case of large noise A plays the role of a time scaling and, therefore, influences the speed of convergence towards the stationary state. In addition, the time scaling depends on the space dimension d.

4.2 Convergence to equilibrium for interacting fibres

Our aim is to perform an analysis of the convergence to equilibrium for the diffusion approximation given by Equation (4.12). This will give us, as in the case without interaction, an important insight into the dependence of the system on the model parameters. The delay length H and the interaction strength represented by c_U are of particular interest for us as they contain the novel additions to the existing fibre models.

Motivated by our interacting fibre model stated in BORSCHE *et al.* (submitted), in KLAR, KREUSSER, *et al.* (in preparation) and KREUSSER (2015), a similar second order system with continuous delay was analysed. In contrast to BORSCHE *et al.* (submitted), in KLAR, KREUSSER, *et al.* (in preparation) and KREUSSER (2015) no projection to the unit sphere for the velocity was applied, but instead an additional friction term was introduced. To analyse the long–time behaviour of the interacting particle system in these studies, the methods introduced in BOLLEY, GUILLIN, *et al.* (2010) were adapted to allow for delay. In the following we will apply the techniques developed in BOLLEY, GUILLIN, *et al.* (2010), KLAR, KREUSSER, *et al.* (in preparation), and KREUSSER (2015) to our model. To apply these techniques, we consider both the particle approximation of Equation (4.12) given by

$$\mathrm{d}x_t^i = \left(-\nabla V(x_t^i) - \frac{1}{N}\sum_{j=1}^{N}\frac{1}{h_H(t)}\int_{t-h_H(t)}^{t}\nabla U(x_t^i - x_s^j)\,\mathrm{d}s\right)\mathrm{d}t + \mathrm{d}W_t^i, \qquad (4.13)$$

which is a first order system, and a mean–field stochastic differential equation with delay

$$\mathrm{d}x_t = -\nabla V(x_t) - \frac{1}{h_H(t)}\int_{t-h_H(t)}^{t}\nabla U \star \rho_s(x_t)\,\mathrm{d}s + \mathrm{d}W_t. \qquad (4.14)$$

In the latter equation we dropped the superscript notation as the particles are indistinguish-

able in this description. Here and in the following we use the notation $\rho_s(x) := \rho(s,x)$, where ρ is the solution of Equation (4.12) and ρ_t is the law of x_t, i.e. x_t is ρ_t–distributed. Therefore, we sometimes also call ρ the solution of Equation (4.14). The difference between Equation (4.13) and Equation (4.14) is that the former describes a whole particle system, whereas the latter is given by one equation and the information about interactions of the fibres is given by the convolution $\nabla U \star \rho$. However, as shown in BOLLEY, GUILLIN, *et al.* (2010) and KREUSSER (2015), for second order models with and without delay, the particle approximation converges to the mean–field stochastic differential equation as $N \to \infty$.

4.2.1 Preliminaries and definitions

To specify what we mean by the convergence to equilibrium for a solution of Equation (4.14), we have to describe which space and which distance we use. Thus, we will use the following definitions (VILLANI, 2003).

Definition 4.1 Let μ be a Borel measure on $\mathbb{R}^d$, i.e. $\mu \in \mathscr{P}(\mathbb{R}^d)$. Then, we denote the set of probability measures on $\mathbb{R}^d$ with finite p–th moment, $p \in \mathbb{N}$, by

$$\mathscr{P}_p\left(\mathbb{R}^d\right) := \left\{ \mu \in \mathscr{P}\left(\mathbb{R}^d\right) \mid \int_{\mathbb{R}^d} \|z\|^p \ \mathrm{d}\mu(z) < \infty \right\}.$$

Definition 4.2 Let $\mu, \nu \in \mathscr{P}(\mathbb{R}^d)$ be two Borel measures on $\mathbb{R}^d$. Then, we define the following set of measures on $\mathbb{R}^d \times \mathbb{R}^d$ by

$$\Pi(\mu, \nu) =$$
$$\left\{ \pi \in \mathscr{P}\left(\mathbb{R}^d \times \mathbb{R}^d\right) \mid \int_{\mathbb{R}^d \times \mathbb{R}^d} (\phi(x) + \psi(y)) \ \mathrm{d}\pi(x,y) = \int_{\mathbb{R}^d} \phi \ \mathrm{d}\mu + \int_{\mathbb{R}^d} \psi \ \mathrm{d}\nu \right\},$$

where ϕ and ψ are integrable, non–negative functions on $\mathbb{R}^d$. The elements $\pi \in \Pi(\mu, \nu)$ are called *transference* or *transfer plans* from μ to ν.

A quite popular and useful distance on the space of probability measures with finite second moments, which we will use for our convergence result, is the 2–*Wasserstein* distance.

Definition 4.3 Let $\mu, \nu \in \mathscr{P}_2(\mathbb{R}^d)$, i.e. Borel probability measures on $\mathbb{R}^d$ with finite second moments. Then, we define the 2–Wasserstein (*Monge–Kantorovich*) distance by

$$W_2(\mu, \nu) = \left(\inf_{\pi \in \Pi(\mu,\nu)} \int_{\mathbb{R}^{2d}} \|x - y\|^2 \ \mathrm{d}\pi(x,y) \right)^{1/2}.$$

The 2–Wasserstein distance may also be written as

$$W_2(\mu, \nu) = \left(\inf \left[\mathbb{E} \left(\|Y - Z\|^2 \right) \right] \right)^{1/2},$$

where the infimum is taken over all pairs of random variables (Y, Z) which are μ and ν distributed respectively, i.e. $\mu = \text{law } Y$ and $\nu = \text{law } Z$.

To actually show convergence to a stationary state, the following two results will be of great importance (HALANAY, 1966).

Theorem 4.4 Let $f : \mathbb{R} \times \mathbb{R} \times \mathbb{R} \to \mathbb{R}$ be a function such that $f(t, u, v)$ is continuous for all (u, v) and all $t_0 \leq t < t_0 + \xi$ for some $\xi > 0$. Furthermore, let $f(t, u, v)$ be increasing with respect to v. Let us suppose that $\dfrac{dy}{dt} \leq f\left(t, y(t), \sup_{s \in [t-H, t]} y(s) \right)$ for $t_0 \leq t < t_0 + \xi$ and some constant $H > 0$. If φ is the solution of the equation

$$\frac{d\varphi}{dt} = f\left(t, \varphi(t), \sup_{s \in [t-H, t]} \varphi(s) \right), \text{ for } t \in [t_0, t_0 + \xi),$$

with the initial condition $\varphi(s) = y(s)$, $s \in [t_0 - H, t_0]$, then

$$y(t) \leq \varphi(t),$$

for $t \in [t_0, t_0 + \xi)$.

From this theorem the following result can be shown.

Lemma 4.5 Let $h : \mathbb{R}_+ \to \mathbb{R}$ denote a non–negative, continuous and bounded function and let $H = \sup_{t \geq 0} h(t) > 0$. In addition let y be a non–negative function satisfying

$$\frac{dy}{dt} \leq -ay(t) + b \sup_{s \in [t-h, t]} y(s), \text{ for } t > t_0,$$

with initial datum $y(s) = y(t_0), s \in [t_0 - H, t_0]$, where a and b are non-negative constants satisfying $a > b \geq 0$. Then, y may be estimated from the above by

$$y(t) \leq y(t_0) \exp(-\lambda (t - t_0)), \text{ for all } t \geq t_0.$$

The decay rate λ is explicitly given by

$$\lambda = a - \frac{1}{H} \mathbb{W}(bH \exp(aH)) > 0,$$

where $\mathbb{W}$ denotes the *product logarithm* function, which is defined by $z = \mathbb{W}(z)\exp(\mathbb{W}(z))$ for all $z \in \mathbb{R}$.

We see that, according to Lemma 4.5, in order to show convergence to equilibrium it is essential to find a function y and constants a and b which relate to Equation (4.14). As a result exponential decay can be shown and a bound for the decay rate can be given.

4.2.2 Decay estimates and convergence

Instead of directly presenting convergence results for Equation (4.14), we first consider a slightly more generalised equation, namely

$$
\mathrm{d}X_t = A(X_t)\mathrm{d}t - \left(\frac{1}{h(t)} \int_{t-h(t)}^{t} \int_{\mathbb{R}^d} B(X_t,x)\rho_s(x)\,\mathrm{d}x\,\mathrm{d}s \right)\mathrm{d}t + \mathrm{d}W_t, \qquad (4.15)
$$

where h denotes a general delay function which fulfils the requirements of Lemma 4.5. Afterwards, in Section 4.2.3, we will show how these results can be applied to Equation (4.14).

Before stating the convergence result in Theorem 4.8, we make the following two assumptions.

Assumptions 4.6 Assume that the function $A : \mathbb{R}^d \to \mathbb{R}^d$ in Equation (4.15) is of the form

$$
A(x) = -\alpha x + g(x),
$$

where $\alpha > 0$ is a constant and g is Lipschitz continuous with the Lipschitzconstant $c_g > 0$, i.e.

$$
\|g(x) - g(y)\| \le c_g \|x - y\|, \text{ for all } x,y \in \mathbb{R}^d.
$$

Assumptions 4.7 Assume that the function $B : \mathbb{R}^d \times \mathbb{R}^d \to \mathbb{R}^d$ in Equation (4.15) satisfies

$$
\|B(x,\hat{x}) - B(y,\hat{x})\| + \|B(x,\hat{x}) - B(x,\hat{y})\| \le c_B \left(\|x - y\| + \|\hat{x} - \hat{y}\| \right),
$$

for some constant $c_B > 0$, independent of $x,\hat{x},y,\hat{y} \in \mathbb{R}^d$.

Theorem 4.8 Under Assumptions 4.6 and 4.7, for any $\alpha,c_g,c_B \ge 0$ with $\alpha - c_g - 2c_B > 0$ and a non–negative, continuous and bounded delay function

$h : \mathbb{R}_+ \to \mathbb{R}$ with $H = \sup_{t \geq 0} h(t) > 0$, there exists a constant λ such that the decay estimate

$$W_2\left(\rho_t, \hat{\rho}_t\right)^2 \leq \exp(-\lambda t) W_2\left(\rho_0, \hat{\rho}_0\right)^2, \quad \text{for } t \geq 0,$$

holds true for the solutions ρ and $\hat{\rho}$ of Equation (4.15) with the corresponding initial conditions $\rho_0, \hat{\rho}_0 \in \mathscr{P}_2\left(\mathbb{R}^d\right)$. In particular, the decay rate λ is explicitly given by

$$\lambda = \lambda_1 - \frac{1}{H} \mathbb{W}(\lambda_2 H \exp(\lambda_1 H)) > 0, \tag{4.16}$$

where $\lambda_1 > \lambda_2 \geq 0$ with

$$\lambda_1 = \alpha - c_g - c_B, \quad \lambda_2 = \frac{c_B^2}{\alpha - c_g - c_B}. \tag{4.17}$$

Proof. Let X_t and $\hat{X}_t$ be solutions of Equation (4.15) with $\rho_t = \text{law}(X_t)$ and $\hat{\rho}_t = \text{law}(\hat{X}_t)$. Suppose that X and $\hat{X}$ fulfil Equation (4.15) with the same Brownian motion. Then, $x_t := X_t - \hat{X}_t \in \mathbb{R}^d$ satisfies

$$\mathrm{d}x_t = \left(A(X_t) - A(\hat{X}_t)\right) \mathrm{d}t - \left(\frac{1}{h(t)} \int_{t-h(t)}^t \int_{\mathbb{R}^d} \left(B(X_t, y)\rho_s(y) - B(\hat{X}_t, y)\hat{\rho}_s(y)\right) \, \mathrm{d}y \, \mathrm{d}s\right) \mathrm{d}t.$$

One can directly compute

$$\frac{\mathrm{d}}{\mathrm{d}t} \|x_t\|^2 = 2 \left\langle x_t, -\alpha x_t + \left(g(X_t) - g(\hat{X}_t)\right)\right\rangle$$
$$- 2\left\langle x_t, \left(\frac{1}{h(t)} \int_{t-h(t)}^t \int_{\mathbb{R}^d} \left(B(X_t, y)\rho_s(y) - B(\hat{X}_t, y)\hat{\rho}_s(y)\right) \, \mathrm{d}y \, \mathrm{d}s\right)\right\rangle, \tag{4.18}$$

where $\langle \cdot, \cdot \rangle$ denotes the scalar product on $\mathbb{R}^d \times \mathbb{R}^d$. Thus, we have

$$\frac{\mathrm{d}}{\mathrm{d}t} \mathbb{E}\left(\|x_t\|^2\right) = 2\mathbb{E}\left(\left\langle x_t, -\alpha x_t + \left(g(X_t) - g(\hat{X}_t)\right)\right\rangle\right)$$
$$- 2\mathbb{E}\left(\left\langle x_t, \left(\frac{1}{h(t)} \int_{t-h(t)}^t \int_{\mathbb{R}^d} \left(B(X_t, y)\rho_s(y) - B(\hat{X}_t, y)\hat{\rho}_s(y)\right) \, \mathrm{d}y \, \mathrm{d}s\right)\right\rangle\right). \tag{4.19}$$

To estimate the first term of this equation, we note that

$$\left\langle x_t, g(X_t) - g(\hat{X}_t)\right\rangle \leq c_g \|x_t\|^2,$$

due to the Lipschitz continuity of g by Assumptions 4.6. We set $\pi_t = \rho_t \otimes \hat{\rho}_t$ where

$\pi_t \in \Pi(\rho_t, \hat{\rho}_t)$ is a transference plan between ρ_t and $\hat{\rho}_t$. Thus, we have the relationship

$$\int_{\mathbb{R}^d} B(X_t, y)\, \rho_s(\mathrm{d}y) - \int_{\mathbb{R}^d} B(\hat{X}_t, \hat{y})\, \hat{\rho}_s(\mathrm{d}\hat{y}) = \int_{\mathbb{R}^d \times \mathbb{R}^d} \left(B(X_t, y) - B(\hat{X}_t, \hat{y})\right)\, \pi_s(\mathrm{d}y, \mathrm{d}\hat{y}).$$

Due to the estimate

$$
\begin{aligned}
-\left\langle x_t, B(X_t, y) - B(\hat{X}_t, \hat{y}) \right\rangle &\leq \|x_t\| \left\| B(X_t, y) - B(\hat{X}_t, \hat{y}) \right\|, \\
&\leq \|x_t\| \left(\|B(X_t, y) - B(X_t, \hat{y})\| + \|B(X_t, \hat{y}) - B(\hat{X}_t, \hat{y})\| \right), \\
&\leq c_B \|x_t\| \left(\|x_t\| + \|y - \hat{y}\| \right),
\end{aligned}
$$

where we used the Cauchy–Schwarz and the triangle inequality, we achieve altogether

$$
\begin{aligned}
\frac{\mathrm{d}}{\mathrm{d}t} \|x_t\|^2 \leq &- 2\alpha \|x_t\|^2 + 2c_g \|x_t\|^2 \\
&- 2\left\langle x_t, \frac{1}{h(t)} \int_{t-h(t)}^t \int_{\mathbb{R}^d} \left(B(X_t, y)\rho_s(y) - B(\hat{X}_t, y)\hat{\rho}_s(y)\right)\, \mathrm{d}y\,\mathrm{d}s \right\rangle, \\
\leq &- 2\alpha \|x_t\|^2 + 2c_g \|x_t\|^2 + 2c_B \frac{\|x_t\|}{h(t)} \int_{t-h(t)}^t \int_{\mathbb{R}^d \times \mathbb{R}^d} \left(\|x_t\| + \|y - \hat{y}\|\right)\, \pi_s(\mathrm{d}y, \mathrm{d}\hat{y})\mathrm{d}s, \\
= &- (2\alpha - 2c_g - 2c_B) \|x_t\|^2 + 2c_B \frac{\|x_t\|}{h(t)} \int_{t-h(t)}^t \int_{\mathbb{R}^d \times \mathbb{R}^d} \|y - \hat{y}\|\, \pi_s(\mathrm{d}y, \mathrm{d}\hat{y})\mathrm{d}s.
\end{aligned}
$$

By applying Young's inequality, i.e. $ab \leq \dfrac{a^2}{2\delta} + \dfrac{\delta b^2}{2}$, for any $\delta > 0$ and $a, b \in \mathbb{R}$, we obtain

$$
\begin{aligned}
\frac{\mathrm{d}}{\mathrm{d}t} \|x_t\|^2 \leq &- (2\alpha - 2c_g - 2c_B) \|x_t\|^2 \\
&+ 2c_B \left(\frac{\delta}{2} \|x_t\|^2 + \frac{1}{2\delta} \frac{1}{h(t)} \int_{t-h(t)}^t \int_{\mathbb{R}^d \times \mathbb{R}^d} \|y - \hat{y}\|^2\, \pi_s(\mathrm{d}y, \mathrm{d}\hat{y})\mathrm{d}s \right), \\
\leq &- (2\alpha - 2c_g - 2c_B) \|x_t\|^2 \\
&+ c_B \delta \|x_t\|^2 + \frac{c_B}{\delta} \sup_{s \in [t-h(t), t]} \int_{\mathbb{R}^d \times \mathbb{R}^d} \|y - \hat{y}\|^2\, \pi_s(\mathrm{d}y, \mathrm{d}\hat{y}), \\
= &- \underbrace{(2\alpha - 2c_g - c_B(2 + \delta))}_{=:\gamma} \|x_t\|^2 + \frac{c_B}{\delta} \sup_{s \in [t-h(t), t]} \int_{\mathbb{R}^d \times \mathbb{R}^d} \|y - \hat{y}\|^2\, \pi_s(\mathrm{d}y, \mathrm{d}\hat{y}), \\
= &- \gamma \|x_t\|^2 + \frac{c_B}{\delta} \sup_{s \in [t-h(t), t]} \mathbb{E}\left(\|x_s\|^2\right).
\end{aligned}
$$

This yields the differential inequality

$$\frac{\mathrm{d}}{\mathrm{d}t} \mathbb{E}\left(\|x_t\|^2\right) \leq -\gamma \mathbb{E}\left(\|x_t\|^2\right) + \frac{c_B}{\delta} \sup_{s \in [t-h(t), t]} \mathbb{E}\left(\|x_s\|^2\right). \tag{4.20}$$

To fulfil the conditions of Lemma 4.5 for $y(t) := \mathbb{E}\left(\|x_t\|^2\right)$, we must have $\gamma = \gamma(\delta) > 0$ as well as $\gamma > \dfrac{c_B}{\delta} \geq 0$. For $c_B = 0$ these conditions are directly fulfilled. Therefore, in the following, we assume that $c_B > 0$. To maximise γ for the estimate given by Equation (4.20) under the given conditions, we aim to maximise the function f defined by

$$f(\delta) := \frac{\gamma(\delta)}{c_B/\delta} - 1 = \frac{2}{c_B}(\alpha - c_g - c_B)\delta - \delta^2 - 1.$$

We solve $f'(\delta_{max}) = 0$ and obtain

$$\delta_{max} = \frac{1}{c_B}(\alpha - c_g - c_B).$$

Furthermore, $f''(\delta_{max}) < 0$ and, thus, δ_{max} actually maximises f. With the assumption $\alpha - c_g - 2c_B > 0$, a short computation shows

$$\delta_{max} > 1,$$
$$f(\delta_{max}) = \delta_{max}^2 - 1 > 0.$$

Substitution of δ_{max} in Equation (4.20) results in

$$\frac{\mathrm{d}}{\mathrm{d}t}\mathbb{E}\left(\|x_t\|^2\right) \leq -(\alpha - c_g - c_B)\mathbb{E}\left(\|x_t\|^2\right) + \frac{c_B^2}{\alpha - c_g - c_B}\sup_{s \in [t-h(t),t]}\mathbb{E}\left(\|x_s\|^2\right),$$
$$= -\lambda_1\mathbb{E}\left(\|x_t\|^2\right) + \lambda_2\sup_{s \in [t-h(t),t]}\mathbb{E}\left(\|x_s\|^2\right).$$

Thus, by Lemma 4.5, we have

$$W_2(\rho_t, \hat{\rho}_t)^2 \leq \mathbb{E}\left(\|x_t\|^2\right) \leq \mathbb{E}\left(\|x_{t_0}\|^2\right)\exp(-\lambda(t - t_0)), \quad \text{for all } t \geq t_0,$$

with

$$\lambda = \lambda_1 - \frac{1}{H}\mathbb{W}(\lambda_2 H \exp(\lambda_1 H)) > 0.$$

Minimising over all joint distributions of X_0 and $\hat{X}_0$ yields the result.   ∎

With this result we can actually guarantee the existence of a unique stationary state and the convergence towards it. As shown in BOLLEY (2008), $\left(\mathscr{P}_2\left(\mathbb{R}^d\right), W_2\right)$ is a complete metric space. Furthermore, $T_t(\rho_0) := \rho_t$ defines a continuous contraction semi–group on $\left(\mathscr{P}_2\left(\mathbb{R}^d\right), W_2\right)$. This guarantees the existence of a unique stationary solution $\rho_\infty \in \mathscr{P}_2\left(\mathbb{R}^d\right)$ (BOLLEY, GUILLIN, *et al.*, 2010; J. A. CARRILLO and TOSCANI, 2007).

Therefore, under the conditions of Theorem 4.8, we have convergence to the stationary state ρ_∞ with the convergence rate

$$W_2\left(\rho_t,\rho_\infty\right)^2 \leq \exp(-\lambda t)W_2\left(\rho_0,\rho_\infty\right)^2, \quad \text{for all } t \geq 0. \tag{4.21}$$

Recalling the original fibre equations, in addition to a finite delay length, the limit $H \to \infty$ should also be considered. However, in this case the results for the convergence to equilibrium shown so far do not hold. In particular, an exponential convergence rate can no longer be guaranteed. Nevertheless, we can give a polynomial convergence rate (SMITH, 1987). This can be done by applying the same method as used in KLAR, KREUSSER, *et al.* (in preparation), to obtain

$$\mathscr{O}\left(t^{-\lambda_\infty}\right), \quad \text{for } t \to \infty, \tag{4.22}$$

where the decay rate λ_∞ is defined as

$$\begin{aligned} \lambda_\infty &:= 1 - \hat{\lambda}, \\ \hat{\lambda} &:= \frac{\lambda_2}{\lambda_1} = \frac{c_B^2}{(\alpha - c_g - c_B)^2} \in [0,1). \end{aligned} \tag{4.23}$$

4.2.3 Application to the diffusion approximation

To apply the theoretical results from Section 4.2.2 to the diffusion approximation given by Equation (4.14), we set $\alpha = 1$ and $c_g = 0$. Under these conditions the parameters λ_1 and λ_2 given in Equation (4.17) are $\lambda_1 = 1 - c_B$ and $\lambda_2 = \dfrac{c_B^2}{1 - c_B}$. For the Lipschitz constant c_B this implies that $c_B < 0.5$ to guarantee convergence. As $H \to \infty$ we obtain only polynomial convergence with $\hat{\lambda} = \dfrac{c_B^2}{(1 - c_B)^2}$. In Figure 4.1 the influence of the parameters c_B and H on the analytical decay rate is illustrated. Figure 4.1(a) shows the dependence of the decay rate $\lambda(c_B, H)$ given by Equation (4.16) on c_B and finite H. For fixed c_B we obtain a monotonically decreasing decay rate for increasing H, with the maximal decay rate at $H = 0$. In addition, as c_B increases for fixed H, the decay rate decreases monotonically. Figure 4.1(b) illustrates the effect of the parameter c_B on the polynomial decay rate λ_∞ given in Equation (4.23), as $H \to \infty$. The decay rate is maximal for $c_B = 0$, and for $c_B \to 0.5$ even the polynomial convergence is lost.

We note that our delay function h_H defined by Equation (3.8) fulfils the requirements of Theorem 4.8. Furthermore, we identify $B(x,y) = \nabla U(x-y)$. Let us denote the Lipschitz constant of ∇U by c, i.e.

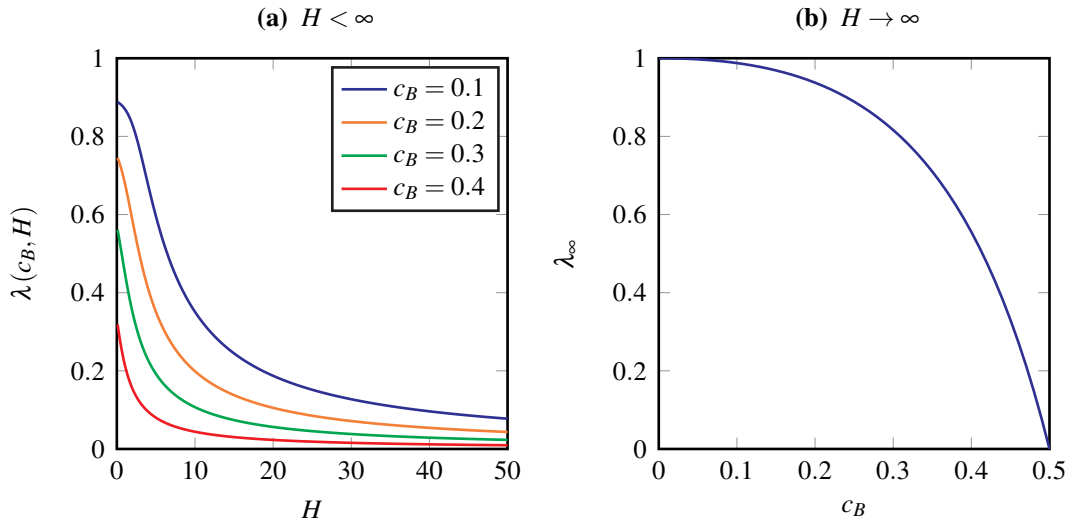$$\|\nabla U(x) - \nabla U(y)\| \leq c \|x - y\|, \quad \text{for all } x, y \in \mathbb{R}^d.$$

Figure 4.1 – The dependence of the decay rates on the parameters c_B and H as $t \to \infty$. Figure 4.1(a) shows the exponential decay rate $\lambda(c_B, H)$ given by Equation (4.16) for finite values of H for four different values c_B. Figure 4.1(b) illustrates how the polynomial decay rate λ_∞ given by Equation (4.23) depends on c_B as $H \to \infty$.

Then, by applying the triangle inequality, we have

$$\|B(x, \hat{x}) - B(y, \hat{x})\| + \|B(x, \hat{x}) - B(x, \hat{y})\|$$
$$= \|\nabla U(x - \hat{x}) - \nabla U(y - \hat{x})\| + \|\nabla U(x - \hat{x}) - \nabla U(x - \hat{y})\|,$$
$$\leq c\|(x - \hat{x}) - (y - \hat{x})\| + c\|(x - \hat{x}) - (x - \hat{y})\|,$$
$$= c\left(\|x - y\| + \|\hat{y} - \hat{x}\|\right).$$

Thus, the Lipschitz constant of B is identical to the Lipschitz constant of ∇U. Depending on this value, either exponential or at least polynomial convergence can be guaranteed or not for solutions of Equation (4.14).

4.3   Numerical results

The conditions for the analytical results presented in Sections 4.2.2 and 4.2.3 are rather restrictive. Nevertheless, we can perform numerical experiments for situations where the analytical conditions no longer hold. In this section we present numerical results for the long–time behaviour of the diffusion approximation given by Equation (4.12). We consider several different parameters and investigate the stationary states and the convergence behaviour. Our particular focus lies in examining the influence of the delay length H and the strength of the interaction potential U, i.e. c_U, on the characteristic behaviour of the solution.

4.3.1 Initial conditions

As the analytical results already suggest, the convergence to equilibrium should not depend on the initial condition as long as the conditions of Assumptions 4.6 and 4.7 are fulfilled. To illustrate that this is actually the case, we consider three different initial conditions in our numerical simulations. Let $\rho_{t,i}$ be the solution of Equation (4.12) at time t with initial conditions corresponding to the index $i \geq 1$

$$\rho_{0,i}(x) = \begin{cases} \left(x_{\mathrm{r},i} - x_{\mathrm{l},i}\right)^{-1}, & \text{for } x \in [x_{\mathrm{l},i}, x_{\mathrm{r},i}], \\ 0, & \text{else,} \end{cases} \tag{4.24}$$

where $x_{\mathrm{l},i} < x_{\mathrm{r},i}$. We set

$$x_{\mathrm{l},i} = x_{\mathrm{l}} + (i-1)x_{\mathrm{shift}},$$
$$x_{\mathrm{r},i} = x_{\mathrm{r}} + (i-1)x_{\mathrm{shift}},$$

where x_{l}, x_{r} and x_{shift} are constants. The initial conditions we use have compact support and fulfil the requirements of Theorem 4.8.

4.3.2 Numerical methods and parameters

For all numerical computations we use a first order splitting method (STRANG, 1968; MCLACHLAN and QUISPEL, 2002). This means that for each time step we solve the following two equations consecutively

$$\partial_t \rho = \nabla_x \cdot \left(\rho \left[\nabla_x V + \nabla_x U \star \bar{\rho}\right]\right), \tag{4.25}$$
$$\partial_t \rho = \Delta_x \rho, \tag{4.26}$$

where the result of one equation after half a time step is used as the initial condition for the other one. For the first part we use the Lax–Friedrichs scheme (LEVEQUE, 1992). The second part is solved implicitly in time using the standard second order finite differences for the Laplace operator Δ_x. For all our computations we use an equidistant spatial grid with step size Δx, as well as a constant time step Δt. Furthermore, we use a finite domain $\Omega \subset \mathbb{R}$ along with zero Neumann boundary conditions. If not indicated otherwise, for all the following numerical simulations of Equation (4.12) we use the parameters as described in Table 4.1.

We checked that the domain considered is sufficiently large and that the step sizes used are sufficiently small. Furthermore, we consider the delay lengths $H \in \{0, 10, 40, \infty\}$, the interaction strengths $c_U \in \{1, 2, 4, 6\}$ and the initial conditions $i \in \{1, 2, 3\}$. In Figure 4.2 the three different initial conditions given by Equation (4.24) in combination with Table 4.1

Symbol	k	Ω	Δx	Δt	x_l	x_r	x_{shift}	t
Value	10	$(-10, 10)$	0.04	$\Delta x / 64$	-3	1	1	100

Table 4.1 – Joint parameters used for all numerical simulations of Equation (4.12).
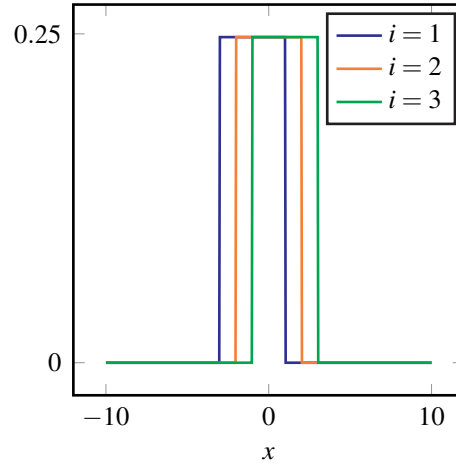

Figure 4.2 – The initial conditions used for the numerical simulations given by Equation (4.24) and Table 4.1.

are illustrated. For k given as in Table 4.1, the Lipschitz constant of ∇U is approximately 1.07 for $c_U = 1$. This means that our numerical analysis is beyond the parameter regime where the analytical results are valid.

For all the numerical simulations we used MATLAB (2015).

4.3.3 The stationary states

The steady states are of particular interest when examining the long–time behaviour of Equation (4.12) as they describe how the long fibres are distributed. In Figure 4.3 we show the solutions for the three different initial conditions $i \in \{1, 2, 3\}$ and the four values of c_U at $t = 100$ for $H \to \infty$. The solutions for the four different non–zero values of c_U shown are symmetric around the origin and bell–shaped, like the reference solution for which $c_U = 0$. As c_U increases the maximal value of the solution at $x = 0$ decreases and the variance increases. In addition, the solutions at $t = 100$ for the three initial conditions and fixed c_U are indistinguishable, which indicates that the stationary state is independent of the initial conditions. Steady state solutions for the other delay lengths $H \in \{0, 10, 40\}$ are indistinguishable and, therefore, not shown. This implies that the steady states are independent of the delay length.
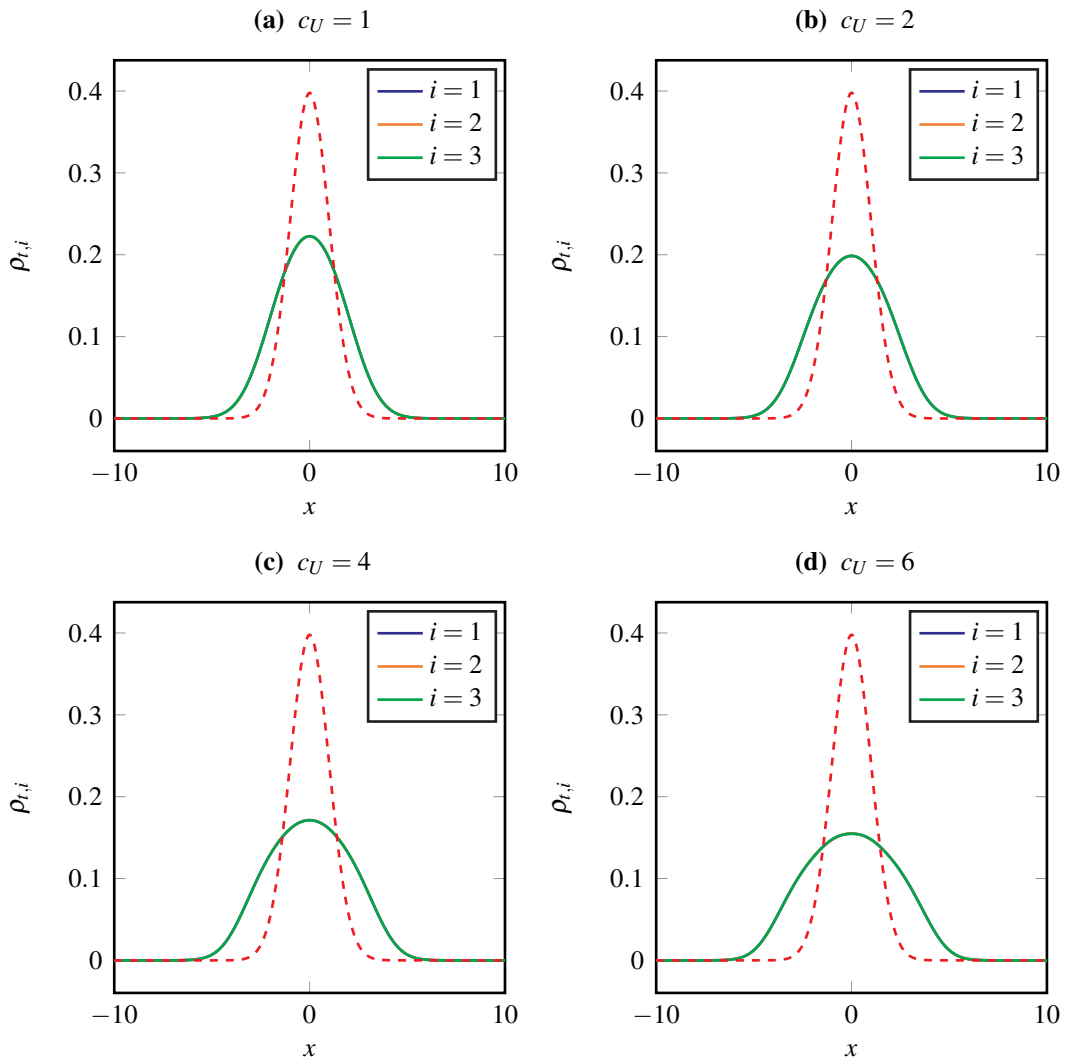
Figure 4.3 – The solutions of Equation (4.12) at $t = 100$ for different values of c_U with the initial conditions as described in Equation (4.24) and $H \to \infty$. The red dashed line represents the stationary reference solution, the case where there is no interaction, $c_U = 0$. The solutions for $i \in \{1, 2, 3\}$ cannot be distinguished in all subfigures. For all numerical simulations the parameters given in Table 4.1 are used.

4.3.4   Convergence to equilibrium

As we have seen in the previous section, in our examples the delay length does not influence the stationary solutions. However, we expect that the delay length influences the dynamics and, therefore, the convergence behaviour towards the stationary state. We begin by investigating the influence of the choice of the initial condition on the evolution of the solution. This is done by analysing

$$\left\| \rho_{t,i} - \rho_{t,j} \right\|_{L_1} = \int_{\mathbb{R}} \left| \rho_{t,i} - \rho_{t,j} \right| \, \mathrm{d}x, \tag{4.27}$$

for $i, j \in \{1, 2, 3\}$, $i \neq j$.

We begin by considering the case $H \to \infty$, which is also the most relevant case as it describes the case of interacting fibres along the whole fibre length. In this case the delay function h_H is given by $h_H(t) = t$. Figure 4.4 shows the convergence to equilibrium in the L_1–norm as defined in Equation (4.27) for the four separate values of c_U. The behaviour in all the graphs is similar: a fast decay towards equilibrium with a small oscillation around $t \approx 5$. As the strength of the interaction increases, the amplitude of this oscillation increases. In all cases we observe that the quantity in Equation (4.27) approaches zero, which shows that the different initial conditions approach the same steady state.

To get a better understanding of how the finite delay lengths $H \in \{0, 10, 40\}$ change the evolution dynamics, we investigate their effect on the convergence to equilibrium. We begin with $H = 40$. In Figure 4.5 we can see the evolution of the differences of the solutions in L_1–norm for the three different initial conditions considered. In all cases convergence to zero, which indicates the convergence to the same stationary state, is observed. Up to $t = 40$ the solutions for $H = 40$ are identical to the ones for $H \to \infty$ due to the delay function which is given by $h_H(t) = t$ for $t \leq H$. Therefore, we can see the same oscillations at the beginning, $t \approx 5$. In contrast to the case $H \to \infty$, when $H = 40$ we can see a small bump at $t = 40$. This is where the delay function switches and is given by $h_H(t) = H$ for $t > H$. We now consider the case $H = 10$ and Figure 4.6 shows the evolution of the difference between the solutions for different initial conditions in the L_1–norm. For all choices of c_U we observe convergence to zero, as for the other values of H considered, which indicates a unique steady state. In Figure 4.6(a) the oscillations are small and a rather fast convergence to equilibrium is observed. As c_U increases, the number and the amplitude of the oscillations increase. In particular, at $t = 10$ a sudden increase in the difference between the solutions can be observed and becomes more obvious for increased c_U. This behaviour can be explained by the structure of the delay function h_H, which changes at $t = H$. Here for $H = 10$, in contrast to $H = 40$, the impact of the delay is rather large. Finally, we consider the case $H \to 0$ and results are shown in Figure 4.7. For

Figure 4.4 – The convergence to a unique steady state for the different initial conditions examined, as $H \to \infty$. In all subfigures the difference between the three separate solutions ρ_1, ρ_2 and ρ_3, with the initial conditions given in Equation (4.24), is shown, where the quantity given in Equation (4.27) is plotted over time. For all numerical simulations the parameters given in Table 4.1 are used.
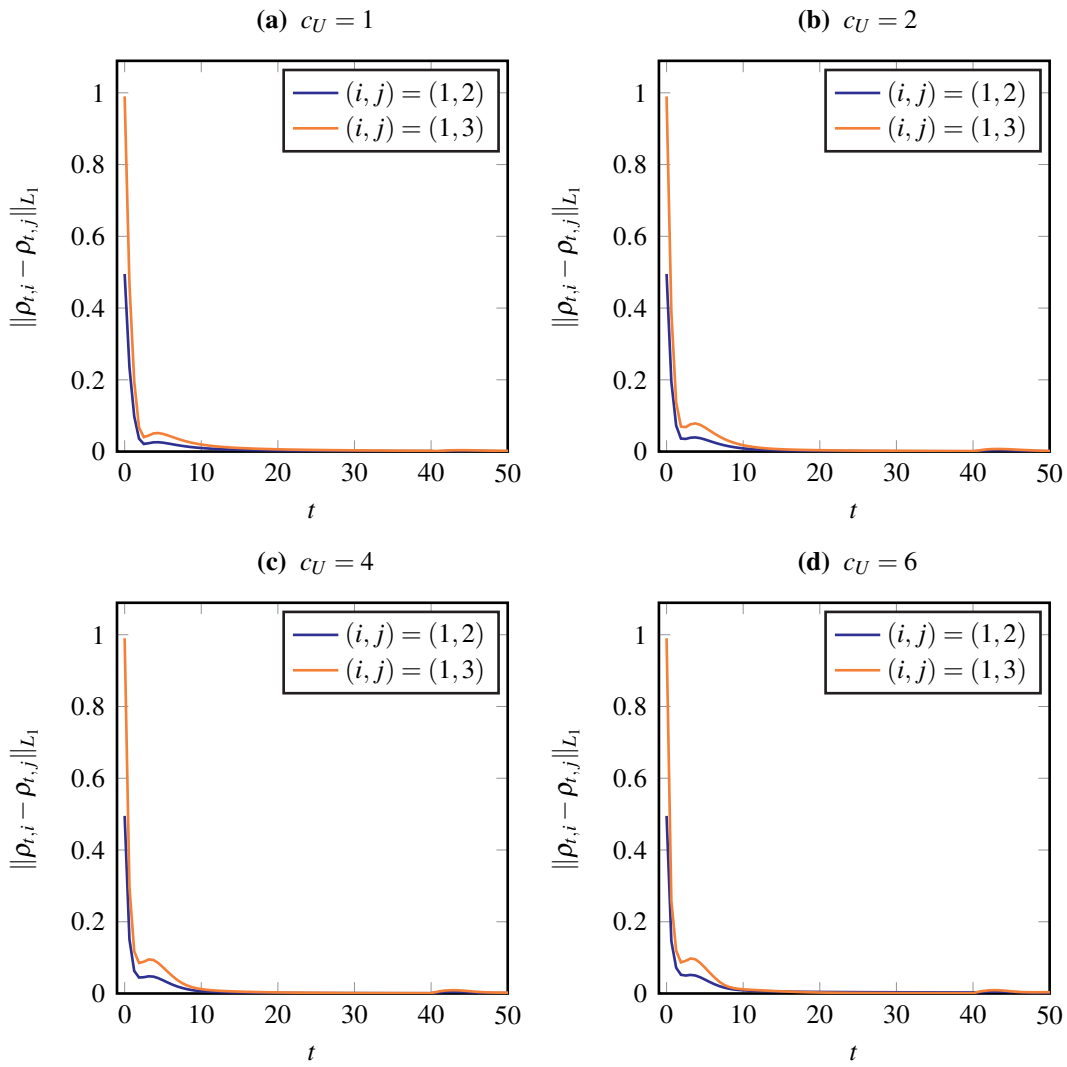
Figure 4.5 – The convergence to a unique steady state for the different initial conditions examined, as $H = 40$. In all subfigures the difference between the three separate solutions ρ_1, ρ_2 and ρ_3, with the initial conditions given in Equation (4.24), is shown, where the quantity given in Equation (4.27) is plotted over time. For all numerical simulations the parameters given in Table 4.1 are used.
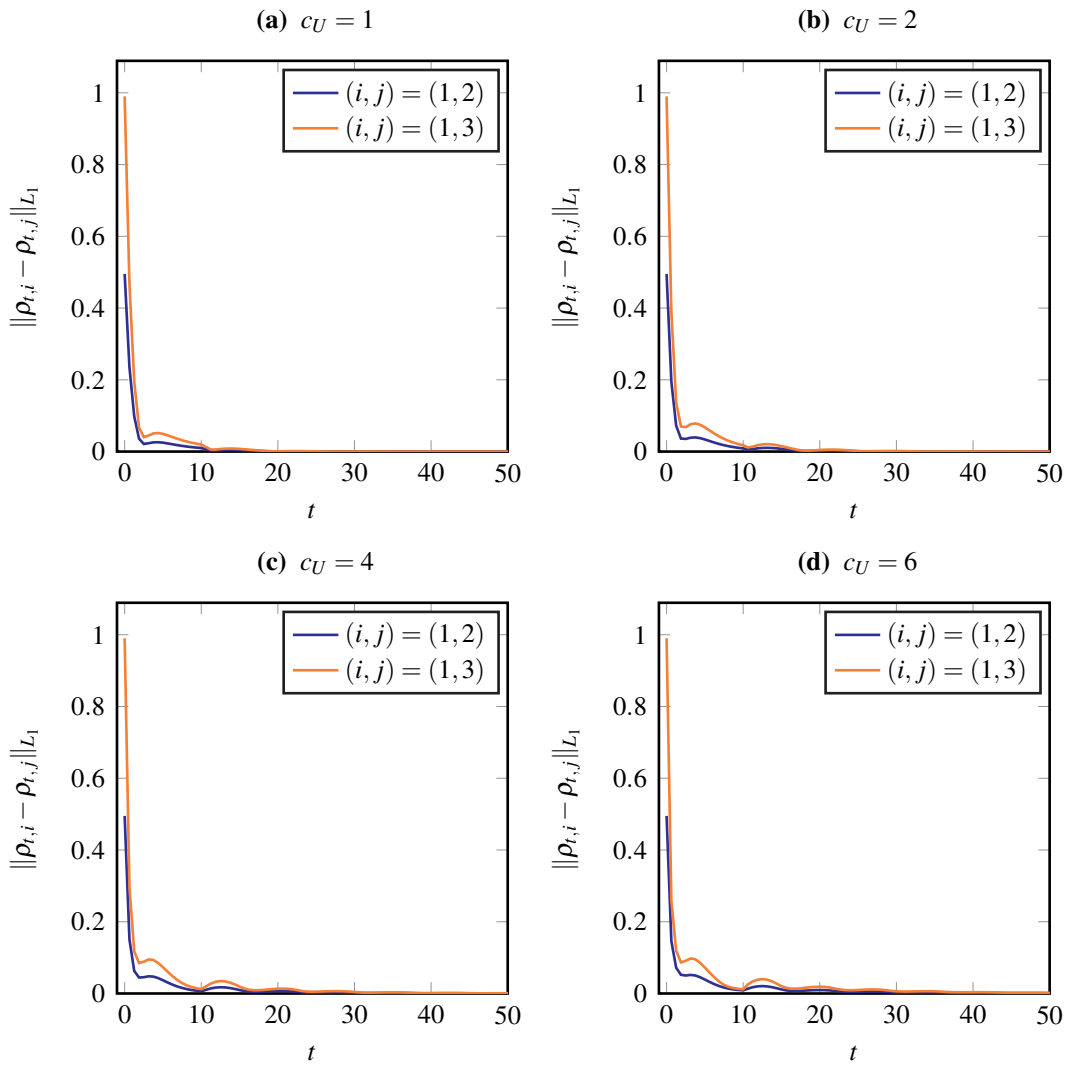
Figure 4.6 – The convergence to a unique steady state for the different initial conditions examined, as $H = 10$. In all subfigures the difference between the three separate solutions ρ_1, ρ_2 and ρ_3, with the initial conditions given in Equation (4.24), is shown, where the quantity given in Equation (4.27) is plotted over time. For all numerical simulations the parameters given in Table 4.1 are used.
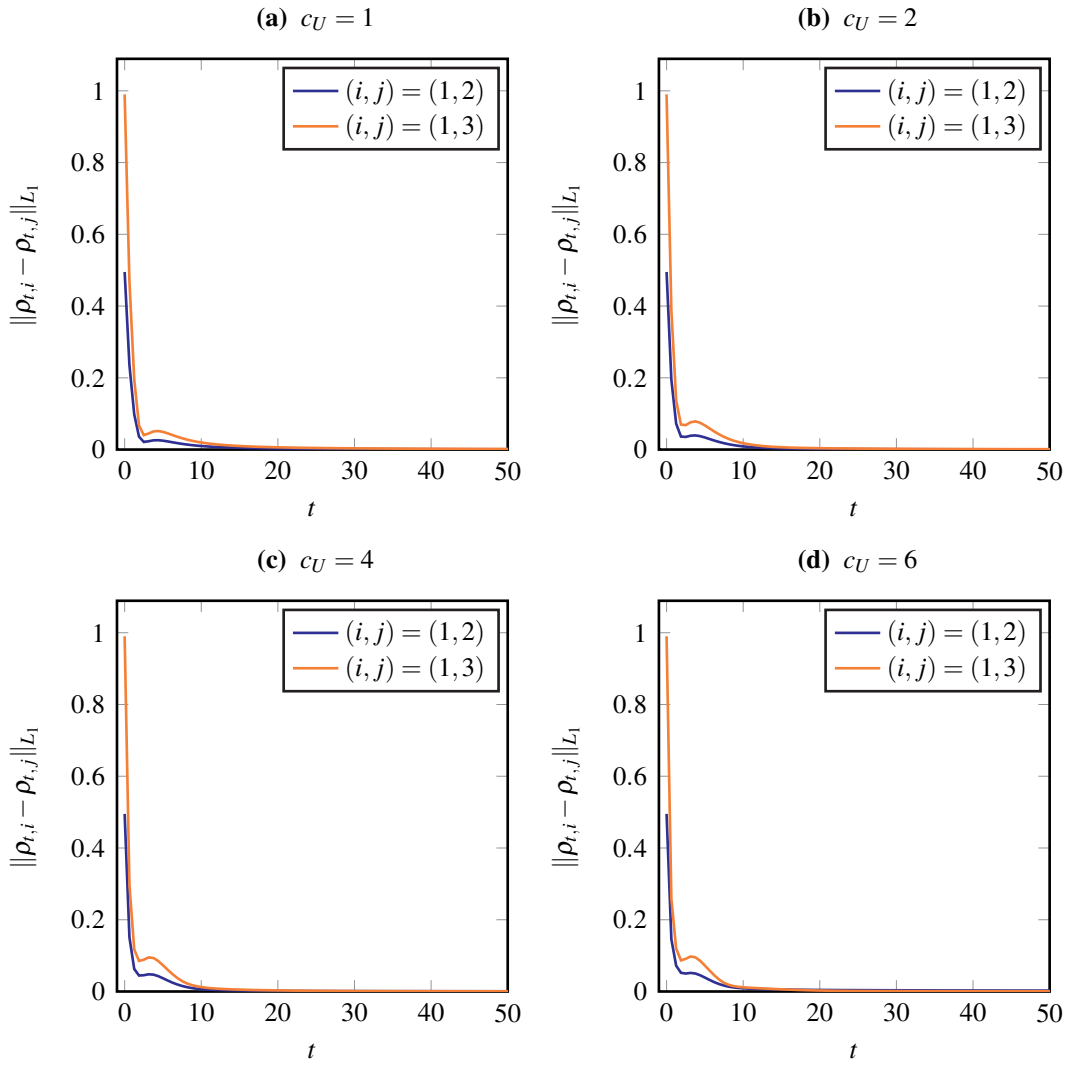
Figure 4.7 – The convergence to a unique steady state for the different initial conditions examined, as $H \to 0$. In all subfigures the difference between the three separate solutions ρ_1, ρ_2 and ρ_3, with the initial conditions given in Equation (4.24), is shown, where the quantity given in Equation (4.27) is plotted over time. For all numerical simulations the parameters given in Table 4.1 are used.
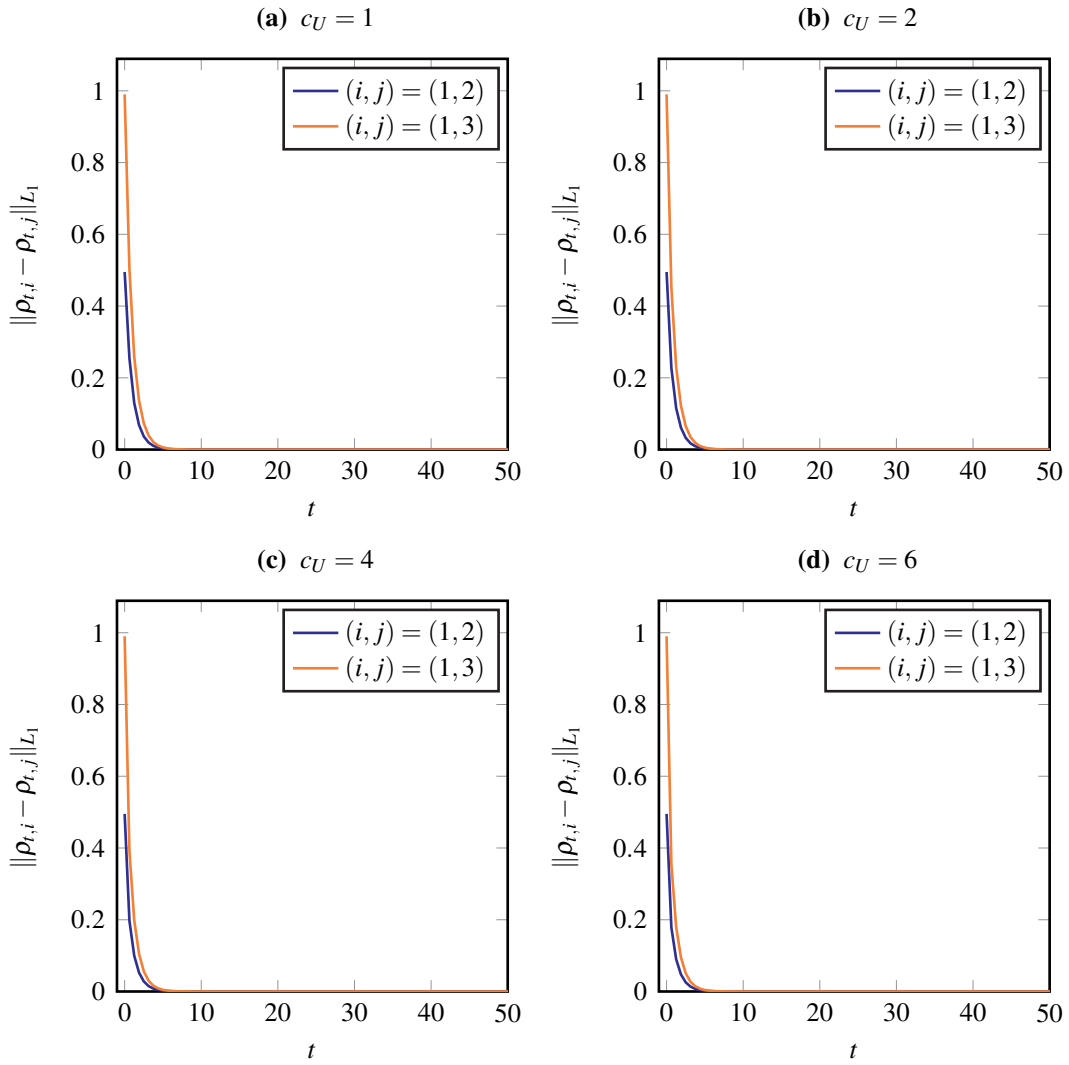
all considered c_U we see a fast monotonic decay towards zero and, therefore, the same stationary state. When compared to the other delay lengths investigated, the convergence to equilibrium is the fastest for $H \to 0$. This matches with the analytical findings from Section 4.2.3. This convergence behaviour is surprising as, so far, we have observed that the number and magnitude of the oscillations increases as H decreases.

As the use of a finite value for H is an approximation to infinite H (see Section 3.3.2 for a discussion) we examine the difference between the solutions in the L_1–norm using infinite H and $H \in \{0, 10, 40\}$. To distinguish between the solutions of Equation (4.12) with different delay lengths, but otherwise identical parameters and initial conditions, we introduce the notation $\rho[H]$. As the numerical results so far have indicated, all solutions, independent of the initial conditions, go to a unique steady state for large time. Thus, we only consider the case $i = 1$. In Figure 4.8 we present the convergence results. In all the cases considered the difference between the solutions converges to zero, as expected from the previous results. This indicates the same stationary state, independent of the delay length H. One can also see that the convergence behaviour is influenced by the interaction strength c_U. As c_U increases the amplitudes of the oscillations also increase. Furthermore, for fixed c_U, the difference between the solutions evolves differently, depending on which cases are considered. Regarding the case $(H, \hat{H}) = (\infty, 40)$, we see that the difference for $t \leq 40$ is zero, as expected, as the delay function h_H is the same in both cases. At $t = 40$ a small bump appears which can be explained in the change of the delay function. A similar result holds true when considering the case $(H, \hat{H}) = (\infty, 10)$. Here the difference is identical to zero for $t \leq 10$ and oscillations are observed for larger values of t. In contrast, a different behaviour is observed for the case $(H, \hat{H}) = (\infty, 0)$. There is one local maximum at a small non–zero value of t followed by a fast monotonic decay to zero. As c_u increases the value of this local maximum increases.

Overall the numerical investigations indicate that large finite H gives a good approximation to the solution as $H \to \infty$. However, when ignoring the initial dynamics for $H \to 0$, this yields a good approximation of $H \to \infty$ as well, which is not expected from the results when we decreased H from 40 to 10.

4.4 Summary

In this chapter we analysed the long–time behaviour of an interacting fibre system with delay both analytically and numerically. We presented the mean–field equation, which is an appropriate description for the interacting fibre system when there are many fibres. We then derived the corresponding diffusion approximation in the case of large turbulences. Considering a more generalised version of this diffusion approximation, we derived an
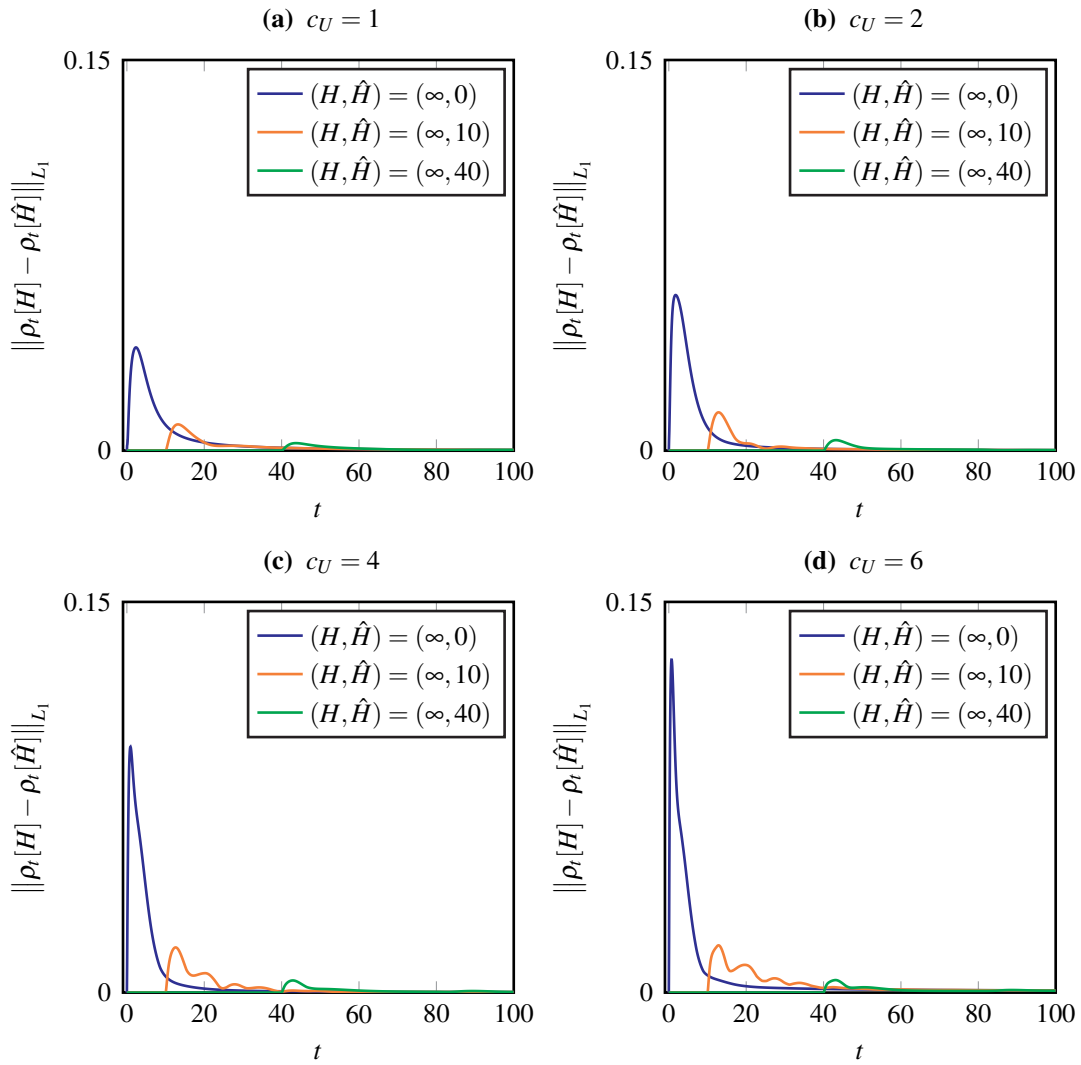
Figure 4.8 – Illustration of the difference of solution of Equation (4.12) for different delay lengths H and interactions c_U with initial conditions as described in Equation (4.24) and parameters given in Table 4.1.

analytical convergence result in arbitrary space dimensions which describes the long–time behaviour and the convergence to equilibrium with restrictions on the various parameters involved in the equation. In particular, we obtained a dependence of the convergence rate on the delay length.

In order to investigate the behaviour of the temporal dynamics of the solution and its convergence behaviour outside the range where our analysis is valid, numerical simulations of the one–dimensional version of the diffusion approximation were presented. In particular, we investigated the influence of the delay length H, the interaction strength c_U and the choice of initial conditions. We observed that the stationary solution was independent of the delay length and initial conditions, but did depend on the interaction strength. However, the delay length did have a qualitative influence on the convergence behaviour.

5 Conclusion

5.1 Summary

In this part of the thesis we presented novel surrogate fibre models describing the fibre lay down in the meltspinning process which includes the fibre thickness. We started by reviewing the existing surrogate fibre models without fibre interaction in Chapter 2 before we stated microscopic interacting fibre models in Chapter 3. In contrast to most existing models of interacting particle systems with time lag, we needed to consider a continuous delay representing the whole fibre length to prevent fibre intersections. Motivated by the effects of belt movement, we additionally presented a modification to our model, where the delay length was truncated. Our modelling approach led to a system of strongly coupled stochastic delay differential equations. After stating the model, we gave illustrative examples of interacting fibre curves in two and three space dimensions, including the case of an anisotropic fibre orientation distribution, as is the case in reality. In particular, we demonstrated the influence of several parameters, most importantly the interaction strength and the fibre radius, and showed that fibre intersections can be prevented. In order to analyse the case of many fibres we continued in Chapter 4 by providing a macroscopic description of the setup in terms of the mean–field equation for the isotropic interacting fibre system. In particular, we considered the case of large air turbulences which led to the corresponding diffusion approximation. In order to gain a better understanding of how many long interacting fibres behave we analysed the diffusion approximation further. We showed that the solution to the diffusion approximation converges to equilibrium in the 2–Wasserstein metric for a range of modelling parameters, and gave explicit decay rates. We demonstrated that the interaction force and the delay length have a notable influence on the speed of convergence to equilibrium. In addition to the analytical results, we performed numerical simulations for the diffusion approximation. The numerical results indicated that convergence to a unique stationary state, independent of the initial condition, holds for a much larger range of parameters than suggested by the theoretical results and that the stationary states are the same for the different delay lengths.

We now discuss areas for future research which could develop and build on the work described above.

5.2　Future work

There are several possible avenues for extending and developing the work on the interacting fibre model presented in this thesis. For example, the interaction could also be incorporated into the smooth models presented in Chapter 2 by adding an additional term for fibre interactions to the external potential which leads to even more detail in the model.

To allow for alignment of the fibres, instead of considering pure repulsion, the model could be extended by including orientation details of the fibres in the interaction term. This could be done by using, for example, the interaction potential introduced in B. J. BERNE and PECHUKAS (1972) or generalised versions thereof (GAY and B. BERNE, 1981; CLEAVER *et al.*, 1996; EVERAERS and EJTEHADI, 2003).

The model for interacting fibres investigated in this part of this thesis has quite a general formulation and could possibly be applied to different areas of research. Pattern formation plays an important role in biology, but in many cases the underlying processes are not completely understood. One could, for example, describe the paths of ants and the patterns they form by replacing the model based on random–walks described in BOISSARD *et al.* (2013) with our model. By describing paths of pheromones, secreted by ants, as particles with continuous delay and the ants as ordinary particles which interact with one another, but are attracted to the pheromones, one could develop a delay system for the trail formation of ants.

Another possible application would be the description of animal swarming patterns, for example of fish or birds. The structure of the models described in J. A. CARRILLO, D'ORSOGNA, *et al.* (2009), J. A. CARRILLO *et al.* (2010), and J. A. CARRILLO, KLAR, *et al.* (2016), where swarming patterns, for example, the formation of flocks and mills (where animals move around in a circular pattern) have been studied, is very similar to that of the surrogate fibre models with and without delay and the model with delay described and analysed in KLAR, KREUSSER, *et al.* (in preparation) and KREUSSER (2015). By including a finite, but continuous, delay in the interaction term, one could test the hypothesis that the movement of animals in a swarm is influenced by the time averaged information of the other participants. Furthermore, using a similar strategy, one could model fish and birds as slender objects with constant length by considering a finite but continuous delay in the interaction term. Due to the constant length, the time delay would vary with the speed of the considered particle. It would be interesting to see if the formation of flocks and mills would still be the same after alterations to the model or if possibly new effects and patterns could be obtained which would represent reality more closely.

5.3   Closing thoughts

Our newly developed fibre model which considers the fibre thickness promises to be a useful extension to the existing surrogate fibre models. Our research showed that non–physical intersections of the fibres can be prevented. This is an important improvement over the existing models. With this work we further the field of surrogate fibre models and, furthermore, provide a novel view on interacting particle systems.

Airlay fabrics

6 The airlay process

In contrast to Part I, where our focus was on the description of an idealised meltspinning production setup, we now focus our attention on the quantitative description of real airlay materials. We start by motivating our research into the production of these materials, before giving an overview of the technology and finally outlining the work presented in this part.

The material presented in this part stems from work developed within the project OPAL 05M13 supported by the German Federal Ministry of Education and Research (BMBF) in collaboration with several project partners. The industrial partners were AUTEFA Solutions[1] and IDEAL Automotive[2]. The academic partners were the groups of the Professors Marheineke, Leugering and Bänsch (the Chair of Applied Mathematics 1, the Chair of Applied Mathematics 2 and the Chair of Applied Mathematics 3 respectively) at the Friedrich–Alexander–Universität Erlangen–Nürnberg (FAU Erlangen) and the Department of Transport Processes at the Fraunhofer Institute for Industrial Mathematics (ITWM) in Kaiserslautern. Several parts of this work have already been published in peer–reviewed journals, see GRAMSCH *et al.* (2016) and KLAR, NESSLER, *et al.* (2016).

OPAL stands for *Optimisation of airlay processes*. The aim of this project was to develop a consistent chain of mathematical models and computer simulations to describe the industrial airlay process with the goal of furthering the understanding of the production process which will act as a basis for the improvement of the technology. Such simulations could, in particular, help to reduce the number of expensive and time consuming experiments and allow for a systematic optimisation of the production process.

6.1 The production process

Airlay fabrics consist of thousands of relatively short fibres, so called *staple fibres*. These fabrics usually consist of a mixture of several fibre types which can vary in weight, size and other physical properties. In many cases the fibres stem from recycled material where the properties of the single components are not known and can vary from batch to batch.

---

[1] `www.autefa.com`
[2] `www.ideal-automotive.com`

(a)

(b)

(c)

(d)
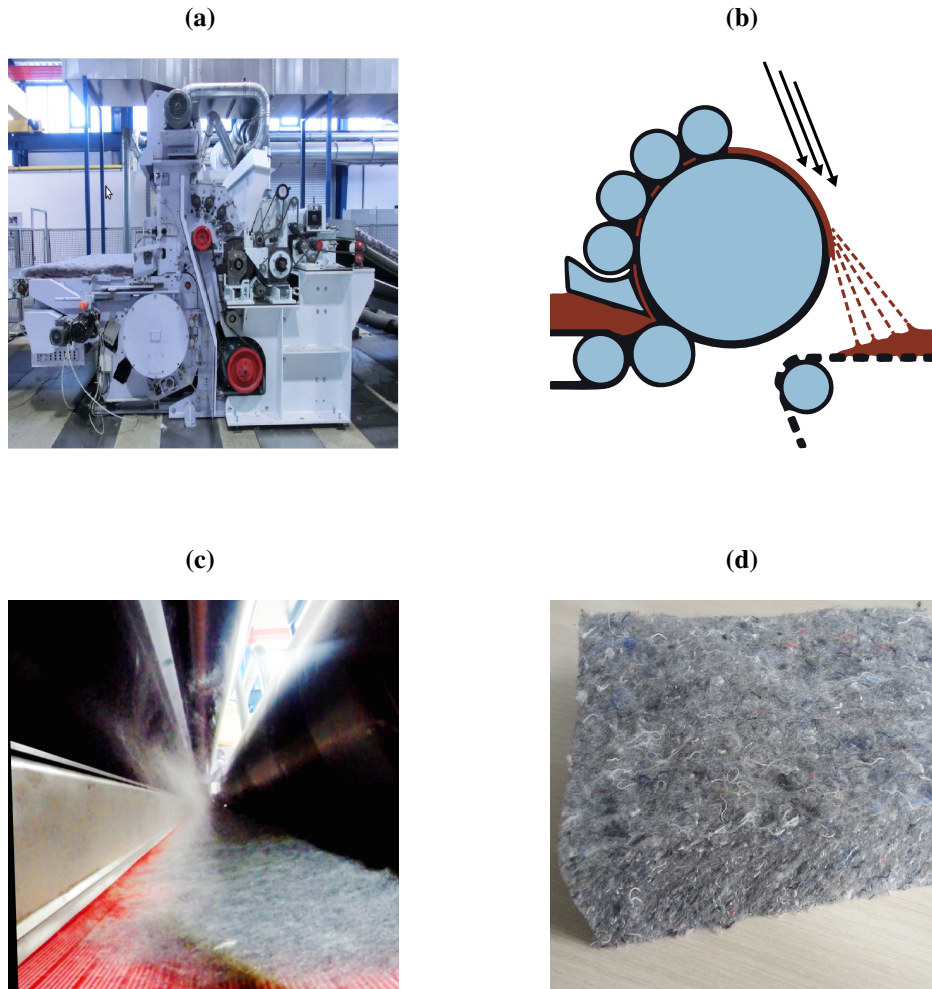
Figure 6.1 – Industrial production process of airlay fabrics. From top left to bottom right: the machine K12 by AUTEFA Solutions, a sketch of the production scenario, the fibre flow and lay down, a finished material after thermo bonding. Images reproduced with the permission from AUTEFA Solutions.

The production of airlay materials involves many steps, which are detailed in Figure 6.1. The machine K12 by AUTEFA Solutions used for the production of airlay fabrics is shown in Figure 6.1(a). In Figure 6.1(b) a sketch of the production process is shown, where the grey and red parts indicate machine parts and fibres respectively. The *rotating card cylinder* (largest circle in the centre) is fed with the incoming fibre mixture from the left. In general, a part of this mixture consists of bicomponent fibres which either melt completely or have a coating which melts upon the application of heat. The single fibres are picked up and then transported by the rotation of the card cylinder. Due to the air stream (indicated by the black arrows) and the cylinder rotation, the single fibres separate and fly towards the moving conveyor belt where they lay down and build layers which constitute the material structure, as may be seen in Figure 6.1(c). The fibres lying on the conveyor belt are only a loose ensemble. Therefore, further post processing is needed to achieve a proper material.

The fibres on the belt are moved into an oven where they are heated so that the bicomponent fibres at least partially melt. As a result of this *thermobonding process*, adhesive joints between the different fibres in the mixture are achieved upon cooling. Figure 6.1(d) shows a sample for a finished product after thermobonding where the different layers resulting from the lay down process are visible.

6.2 The project partners and their roles

The work of the project partners AUTEFA Solutions, IDEAL Automotive, the Department of Transport Processes, Fraunhofer ITWM and the group of Prof. Dr. Leugering at FAU Erlangen facilitated us in our research by providing material specifications, experiments and numerical simulations.

AUTEFA Solutions is a machine producer who is, in particular, involved in the development and improvement of the machines based on the airlay technology. With aerodynamic web forming they want to fulfil the high expectations of their customers to produce high quality materials at a low cost. They provided us with results from experiments and the corresponding machine settings.

IDEAL Automotive is a producer of several fibre based components in the automotive industry. Their focus lies in producing form parts and, in particular, acoustic absorbing parts at different positions with different requirements throughout cars. They provided us with important information about different fibre types and, like AUTEFA Solutions, gave us an interesting insight into the production process.

The project partners at the Department of Transport Processes, Fraunhofer ITWM extended existing and developed new models to describe the complicated flight of the short staple fibres in the air stream. Furthermore, these models were implemented in the fibre simulation tool FIDYST (Fraunhofer ITWM). As the numerical simulation for these models is computationally expensive, only a few hundred fibres can actually be simulated instead of the thousands which would be needed to build a whole airlay fabric. Nevertheless, such simulations can give important insights into how the flight of the fibres depends on various parameters stemming from the machine settings.

The group of Prof. Dr. Leugering at FAU Erlangen developed a mathematical model to perform virtual tensile strength tests on virtual materials. It is hoped that these can replace some of the expensive real experiments in future. For details, see STROHMEYER and LEUGERING (2016) and GRAMSCH *et al.* (2016).

Our role in the project was to bridge the gap between the fibre flight simulations performed by the Department of Transport Processes, Fraunhofer ITWM and the virtual tensile strength tests developed at FAU Erlangen. This was done by using characteristic

information provided by the fibre flight simulations, as well as machine settings and fibre specifications provided by AUTEFA Solutions and IDEAL Automotive to develop a model for a virtual non–woven material.

In contrast to the models developed for paper making (J. HÄMÄLÄINEN, LINDSTRÖM, *et al.*, 2011; J. HÄMÄLÄINEN, T. HÄMÄLÄINEN, *et al.*, 2014) and the models based on stochastic geometry (SCHLADITZ *et al.*, 2006; OHSER and SCHLADITZ, 2009; RE-DENBACH and VECCHIO, 2011; REDENBACH, RACK, *et al.*, 2012; KÄRKKÄINEN *et al.*, 2012; REDENBACH, SCHLADITZ, *et al.*, 2014; VECCHIO, 2014) our particular goal was to develop a three–dimensional model which can be linked to the production process and does not purely rely on the information gained from micro computer tomography (μ–CT). Such a model allows for the inclusion of the effects of the various machine and fibre parameters on the structure of the airlay fabric.

6.3 Structure

The remainder of this part of the thesis is structured as follows. In Chapter 7 we present a material model for the airlay fabric. This includes a description of the fibre placement within the material, as well as of the fibre model we use. Then, in Chapter 8, we describe the parameter estimation of several fibre and material parameters which are *a priori* unknown and have to be determined from computer simulations or experiments. In Chapter 9 we explain how to perform numerical simulations based on the model introduced in Chapter 7 in combination with the parameters determined using the methods introduced in Chapter 8. In particular, we consider three scenarios supported by experiments and discuss the results from the numerical simulations based on this data. Finally, in Chapter 10, we conclude this part of the thesis. We summarise the results obtained, suggest possible applications of the model and the methods developed in this work, and discuss possible areas of future work.

7

A material model

For the accurate description of an airlay material it is essential to include the effects of all the steps of the production process. The novel model presented in this chapter consists of a macroscopic material model coupled to a microscopic model for the individual fibres. The material model is developed by first considering the planar distribution of the fibres on the moving belt. The two–dimensional description is then extended by including the height to give the three–dimensional material. After describing how to correctly account for the orientation and placement of the fibres in the material model, we turn our attention to the microscopic fibre model, which is extended to include additional detail.

7.1 The modelling setup

Before we develop the material model, we first set up a framework. For the lay down area we consider a belt with width $a > 0$. The *machine direction* (md) describes the direction the belt moves and the *cross direction* (cd) describes the direction orthogonal to the belt movement in the plane of the belt. Furthermore, *the thickness direction* describes the direction orthogonal to md and cd in the direction of the material height.

Airlay materials are almost always composed of several different fibre types. Therefore, our model allows for N different types of fibres where each fibre type can have its own specific properties. The fibre type itself is denoted with the index $i \in \{1, \ldots, N\}$ and we assume that there is a large number of each type of fibre.

For the generation of the fibre material, we consider a box–shaped *reference volume* $V \subset \mathbb{R}^3$. We assume that the width in cross direction and the length in machine direction of the reference volume are equal and given by $d > 0$. In addition, we assume that the height of the reference volume coincides with the material height $H > 0$. Therefore, we describe the reference volume V as the set

$$V = \left[-\frac{d}{2}, \frac{d}{2} \right]^2 \times [0, H] \subset \mathbb{R}^3, \tag{7.1}$$

where we assume $d \leq a$ so that the reference volume V is completely placed on the belt. Now that the modelling framework has been setup, we now describe how the airlay material

in the reference volume V can be modelled.

7.2 The planar fibre distribution

The realistic placement of the fibres is essential for the development of an accurate model. In contrast to Section 7.3 where we will describe the fibre distribution in the thickness direction, here the different fibre types can be considered independently, as they do not influence the planar distribution of one another.

7.2.1 The extended reference volume

Fibres with the initial point in V will naturally have at least some portion in V itself. However, we also need to consider fibres with initial points outside V, but have portions inside V. To include these fibres in our model, we consider an *extended reference volume* V_i for each fibre type. We choose V_i in such a way that fibres with initial points outside V_i do not need to be considered as they cannot contribute to the material inside the reference volume V. Thus, for each fibre type i we extend the width d of the reference volume V by the stretched fibre length L_i. The stretched length L_i describes the fibre length when being completely stretched, which in mathematical terms is the arc–length. The extended width d_i is, thus, given by

$$d_i := d + 2L_i.$$

This leads to the extended reference volume V_i for fibre type i with

$$V_i = \left[-\frac{d_i}{2}, \frac{d_i}{2} \right]^2 \times [0, H] \supset V,$$

where we assume $d_i \leq a$ so that the extended reference volume V_i is completely placed on the belt. In Figure 7.1 the belt with both the reference volumes V and V_i and coordinate directions is illustrated.

7.2.2 Fibre distribution densities

To describe the placement of the fibres in the material, it is important to understand how the fibres are distributed on the conveyor belt. We assume that the fibre lay down is uniform in the cross direction and, thus, assume the fibres to be uniformly distributed in cross direction. However, uniformity in the machine direction cannot be assumed. As we assume a large number of fibres, we are not necessarily interested in where each individual fibre is on the belt, but in the distribution densities which we denote by g_i. The value $g_i(x)$ gives the probability that a fibre of type i lays down at $x \in \mathbb{R}$ in machine direction. We expect
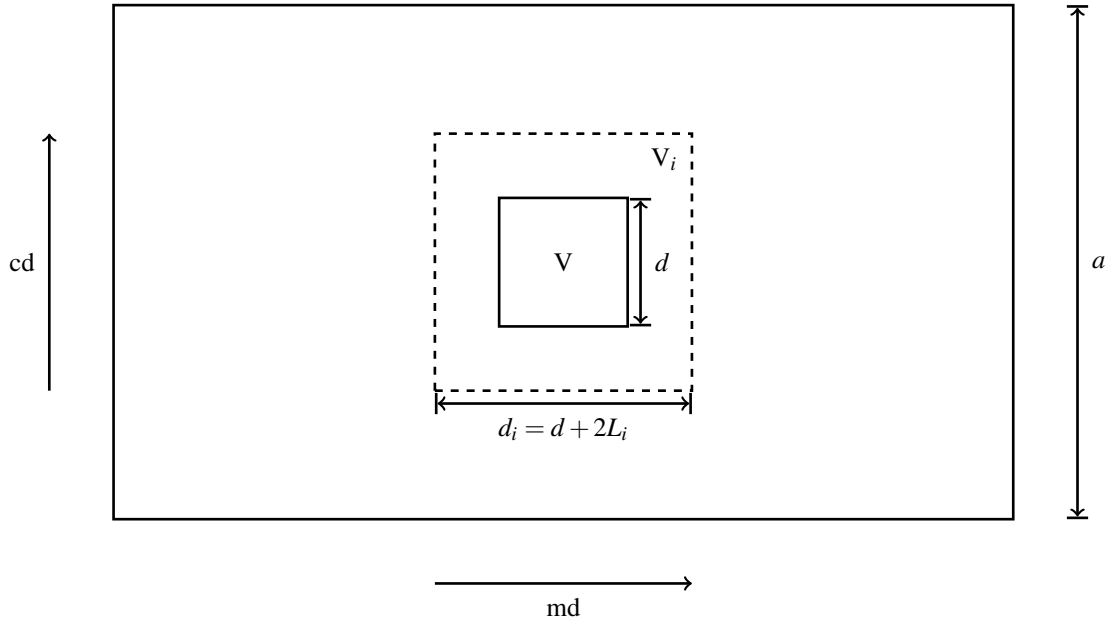
Figure 7.1 – Sketch of the lay down domain, reference volume V and extended reference volume V_i along with dimensions and coordinate directions. The machine direction (the direction of belt movement) and the cross direction are denoted by md and cd respectively.

the densities to be normalised, so that

$$\int_{\mathbb{R}} g_i(x) \, dx = 1. \tag{7.2}$$

Due to the production process, the fibres can only fly a finite distance. This allows us to make the assumption that the fibre distribution densities g_i are compactly supported with support

$$\text{supp}(g_i) = [x_{min,i}, x_{max,i}], \tag{7.3}$$

with $0 \le x_{min,i} < x_{max,i}$. The coordinates for the densities are given in the fixed coordinate system of the machinery and indicate the distance to the card cylinder.

7.2.3 The belt movement

So far we have not allowed for the belt movement in the machine direction. To do so, we denote the function describing the centre of the extended reference volume V_i moving along with the belt over time by χ_i. Like the distribution densities g_i, we assume χ_i to be given in the fixed coordinate system of the machinery. Furthermore, we denote the constant belt speed in the machine direction by $v_{\text{belt}} > 0$. We assume that, at the time $t = 0$, the right–hand boundary of V_i coincides with $x_{min,i}$. This is equivalent to $\chi_i(0) = x_{min,i} - \dfrac{d_i}{2}$. At $t = T_i$ we assume that the left–hand boundary of V_i coincides with $x_{max,i}$. This is
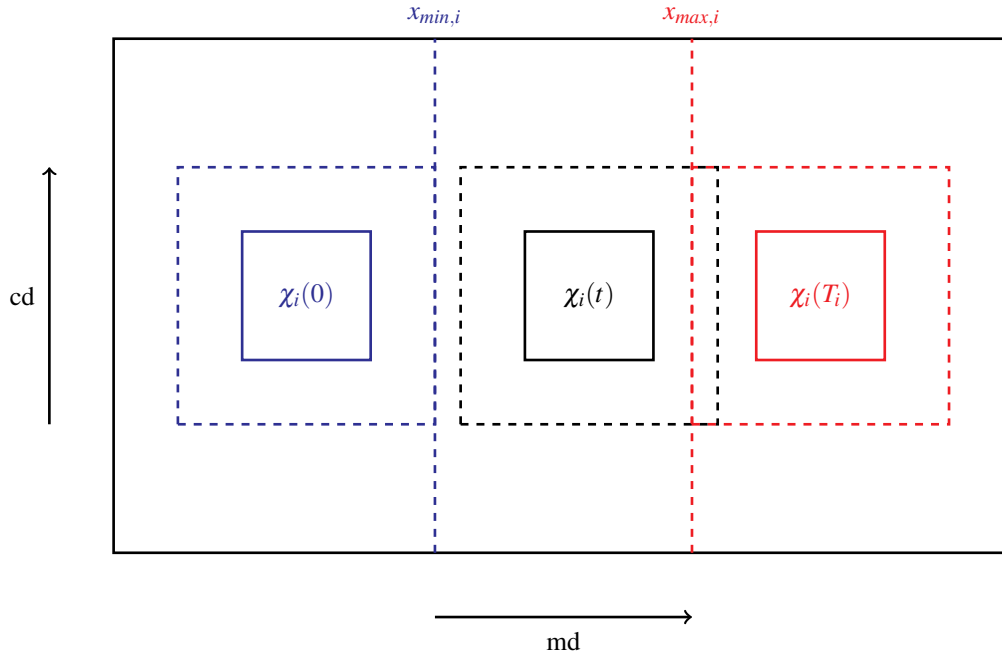
Figure 7.2 – An illustration of the lay down domain and extended reference volume V_i for fibre type $i \in \{1, \ldots, N\}$ as it is transported due to the belt movement. The centre of V_i at time t is indicated by $\chi_i(t)$. The maximal lower and the minimal upper bound for the support of the fibre distribution densities g_i are denoted by $x_{min,i}$ and $x_{max,i}$ respectively. At $t = 0$, the position of the right–hand boundary in the machine direction (md) of V_i is $x_{min,i}$. At $t = T_i$, the position of the left–hand boundary of V_i is $x_{max,i}$. For $t > T_i$, any fibres laid down cannot contribute to the reference volume, whereas fibres laid down for $0 < t < T_i$ could have portions in the reference volume V.

equivalent to $\chi_i(T_i) = x_{max,i} + \dfrac{d_i}{2}$. Thus, T_i is the time we have to consider to account for all the fibres of type i contributing to the reference volume V. As we assume a constant belt speed, we define χ_i by

$$\chi_i : [0, T_i] \to \mathbb{R},$$
$$\chi_i(t) = x_{min,i} - \frac{d_i}{2} + t v_{\text{belt}}, \tag{7.4}$$
$$T_i = \frac{1}{v_{\text{belt}}} \left(x_{max,i} - x_{min,i} + d_i \right).$$

In Figure 7.2 the lay down domain along with the moving reference volumes due to the belt movement is illustrated.

Now we need to extend this two–dimensional description to a three–dimensional one by allowing for the height.

7.3   The height distribution

To give a realistic description of an airlay fabric, it is essential to derive a three–dimensional model which includes the height of the material. Instead of modelling the effect of every individual fibre on one another, we consider a statistical description for the distribution of the fibres in the thickness direction. We begin with a simplified case, considering a single fibre type, $N = 1$. To find out where a fibre should be laid down, we have to consider the existing height of the material surrounding the fibre dropping point $x^* \in \mathbb{R}$. Assuming a continuous production process and belt movement, we can imagine that the fibre material is composed as a superposition of the lay down density in the machine direction. This can be expressed as

$$G_1(x^*) = \int_{-\infty}^{x^*} g_1(x) \, \mathrm{d}x.$$

Scaled with the material height H, this gives the height distribution

$$R(x^*) = HG_1(x^*).$$

Thus, for a given dropping point x^* one can determine the position in the thickness direction for a new fibre. For $x^* > x_{max,1}$ we have $R(x^*) = H$ as g_1 is compactly supported and fulfils the normalisation given by Equation (7.2). This means that the fibres lay down at the maximal material height. For $x^* < x_{min,1}$ we have $R(x^*) = 0$ and, thus, the fibres lay down on the belt itself.

For several fibre types, i.e. $N > 1$, the situation is no longer so simple. Following the strategy for a single fibre type and constructing height distributions for each fibre type independently would not represent reality very well as all types jointly contribute to the material height. Fibres of the different types build the laid down material and, therefore, influence the shape of the material and the height for the lay down of a new fibre. We make the assumption that there exists a joint fibre distribution density g which is given as a convex combination of all the fibre distribution densities g_i:

$$g(x) = \sum_{i=1}^{N} \beta_i \, g_i(x), \tag{7.5}$$

with

$$\mathrm{supp}(g) = [x_{min}, x_{max}], \tag{7.6}$$

where

$$x_{min} := \min\left\{x_{min,i} \,\middle|\, i \in \{1,\ldots,N\}, \beta_i > 0\right\},$$
$$x_{max} := \max\left\{x_{max,i} \,\middle|\, i \in \{1,\ldots,N\}, \beta_i > 0\right\}, \tag{7.7}$$

and so

$$\mathrm{supp}(g_i) \subseteq \mathrm{supp}(g).$$

The variables $0 \le \beta_i \le 1$ in Equation (7.5) with $\sum_{i=1}^{N}\beta_i = 1$ are weights. We assume that there exists $i \in \{1,\ldots,N\}$ such that $\beta_i > 0$. If $\beta_j = 1$ and $\beta_i = 0$ for all $i \ne j$, with $i, j \in \{1,\ldots,N\}$, we retrieve the simplified case where the material height only depends on a single fibre type. In the general case for arbitrary N, as in the simplified case $N = 1$, we introduce the cumulative distribution functions

$$G_i(x^*) = \int_{-\infty}^{x^*} g_i(x) \, dx.$$

The function

$$G(x^*) = \sum_{i=1}^{N} \beta_i \, G_i(x^*),$$

is the convex combination of the cumulative distribution functions G_i. The general height distribution is then given by

$$R(x^*) = HG(x^*). \tag{7.8}$$

So far we have not specified the weights β_i. We make the assumption that the more fibres of one type laid down, the more this fibre type contributes to the total material height H. Thus, we set $\beta_i := \beta_{n,i}$ where the number based ratio $\beta_{n,i}$ is defined as

$$\beta_{n,i} = \frac{\frac{M_i}{m_i}}{\sum_{j=1}^{N} \frac{M_j}{m_j}}. \tag{7.9}$$

Here the parameter M_i denotes the overall mass of fibres of type i in the material and m_i the mass of a single fibre of type i.

7.4   Accounting for the material weight

In practice, one of the important properties of an airlay fabric is the base weight W of the material, i.e. the weight per surface area. To account for this property we have to use the correct number of fibres $n_i \in \mathbb{N}$ in our model to fill the reference volume V. This number depends on the mass rate $\dot{m}$, the weight of each fibre m_i, the time T_i, the ratio of the width of the reference volume d_i to the belt width a and the mass ratio $\beta_{m,i}$ of the considered fibre type, which is defined by

$$\beta_{m,i} = \frac{M_i}{\sum_{j=1}^{N} M_j}.$$

The mass rate describes how much fibre mass per time unit is produced. The ratio of the mass rate $\dot{m}$ to the fibre mass m_i multiplied by the mass ratio $\beta_{m,i}$ gives the overall number of fibres per time unit. This, in combination with the ratio of the width of the reference volume d_i to the belt width a multiplied by time T_i, gives

$$n_i = \left[\beta_{m,i} \frac{\dot{m}}{m_i} \frac{d_i}{a} T_i \right], \tag{7.10}$$

where $[\cdot]$ indicates rounding to the nearest integer. Using this we have the correct amount of fibres for the extended reference volume V_i for each i and, thus, for the reference volume V itself. We now describe how these fibres are placed and oriented in the reference volume.

7.5   The fibre orientation and placement

So far we have regarded the fibres as single points and considered their distribution within the material. However, to develop a model for the whole material, we have to describe how the complete fibres are placed and oriented. Intuitively, we can assume that a dropping fibre would nestle against the existing material structure. Locally, the material structure can be described by an orientation matrix $S : \mathbb{R} \to \mathrm{SO}(\mathbb{R}^3)$, where $\mathrm{SO}(\mathbb{R}^3)$ denotes the special orthogonal group in three dimensions. This rotation matrix describes the local orientation of the local (tangential) surface and contains information of how a fibre is oriented within the material. As the fibres are assumed to be uniformly distributed in the cross direction of the material, and the position in thickness direction is given by $R(x)$ where $x \in \mathbb{R}$ is the coordinate in machine direction (see Equation (7.8)), we obtain the following orientation

matrix

$$S(x) = \frac{1}{1 + (R'(x))^2} \begin{pmatrix} 1 & 0 & -R'(x) \\ 0 & 1 & 0 \\ R'(x) & 0 & 1 \end{pmatrix}.$$

We see that the columns of this matrix build an orthogonal basis, where the first two columns locally span the contour surface of the material.

With l_i we denote the cut length of the fibre which is the distance from one end of the fibre to the other end. Considering a general fibre of type i as a parametrised curve with respect to the fibre's cut length

$$\zeta_i : [0, l_i] \to \mathbb{R}^3,$$

with arc–length L_i

$$L_i = \int_0^{l_i} \left\| \frac{\mathrm{d}\zeta_i}{\mathrm{d}s}(s) \right\| \mathrm{d}s, \tag{7.11}$$

we can prescribe the position and orientation of the fibre within the material. In the following, ζ_i has to be specified further. For simplicity, we assume that the main fibre orientation coincides with the orientation of the initial point of the fibre $\zeta_i(0)$ and lies in the md–cd plane. After rotating and shifting, the fibre in the virtual material can be described by the parametrised curve

$$\phi_s[x, y, \cdot] : [0, T_i] \to \mathbb{R}^3,$$

$$\phi_s[x, y, t] = S(x) \left(\zeta_i(s) - \zeta_i(0) \right) + \begin{pmatrix} x - \chi_i(t) \\ y \\ R(x) \end{pmatrix}, \tag{7.12}$$

where $x \in \mathrm{supp}(g_i)$ and $y \in [-d_i/2, d_i/2]$ denote the coordinates in the machine and the cross direction respectively. The parameter t is related to the belt movement and, therefore, to the position of the reference volume on the belt. The parameter s, however, corresponds to the parametrisation of the fibre curve. Due to the spatial shift in machine direction by $\chi_i(t)$, we obtain a fibre description with respect to the local coordinate system of the reference volume V introduced in Equation (7.1). The fibre can contribute to the reference volume V only for $x - \chi_i(t) \in [-d_i/2, d_i/2]$. Note that the shift $\zeta_i(0)$ in Equation (7.12) is necessary to obtain the correct fibre placement independent of the description of ζ_i itself and, in particular, independent of the initial value $\zeta_i(0)$.

7.6   The fibre model

So far we have described a material model without specifying the actual fibre model to be used for the fibre ζ_i. The correct description of the fibres themselves is essential for a realistic material model. Our main objective is to use a model which describes the main characteristics of the real fibres and which can be parametrised by a few parameters related to the fibre properties and possible to determine experientially. As in the case for long fibres in the application of meltspinning, see Part I, we aim to model a single fibre by a parametrised curve which describes the centre line of the fibre. Therefore, we use the anisotropic fibre model given by Equation (2.26) to describe a single fibre ζ_i. Including the anisotropic fibre orientation, represented by the anisotropy parameter B, not only allows for fast numerical computations, but enables us to include an anisotropic orientation of the fibres in our model.

We have to choose appropriate parameters for the model. Apart from the anisotropic parameter B, which describes an overall material property, these parameters are all dependent on the fibre type used. Details on the parameter estimation methods used will be given in Chapter 8.

The anisotropic model already describes many important features of a real fibre. However, we include a more detailed representation by adding crimps which are characteristic for the fibres used in airlay products. We describe these crimps by a *crimp function* γ_i. As for the fibre curve ζ_i, we require that the crimp function is a parametrised curve given on the interval $[0, l_i]$. As the crimps usually have a regular structure, we choose

$$\gamma_i : [0, l_i] \rightarrow \mathbb{R}^3,$$

$$\gamma_i(s) = \begin{pmatrix} s \\ c_i \sin(C_i \pi s) \\ 0 \end{pmatrix}. \tag{7.13}$$

This describes a sinusoidal crimp structure, where C_i and $c_i > 0$ are parameters which relate to the crimp, i.e. the number of arcs and the difference between the cut and the stretched fibre length l_i and L_i respectively. Other crimp functions are possible, in particular rotated versions of Equation (7.13) or other periodic functions. If one does not want to add crimps, then one can scale the fibre length by choosing

$$\gamma_i(s) = \begin{pmatrix} c_i \\ 0 \\ 0 \end{pmatrix}, \tag{7.14}$$

to obtain the correct stretched fibre length L_i. Given an arc length parametrised fibre curve $\zeta_i : [0, l_i] \to \mathbb{R}^3$ with the right hand orientation tripod

$$Q_i : [0, l_i] \mapsto \mathrm{SO}(\mathbb{R}^3),$$
$$Q_i(s) = (v_i(s), n_{1,i}(s), n_{2,i}(s)),$$

where v_i, $n_{1,i}$ and $n_{2,i}$ are the orientation, the normal and the binormal of the fibre respectively, we can describe the crimped fibre curve ξ_i by

$$\xi_i(s) = \int_0^s Q(\tilde{s}) \frac{\mathrm{d}\gamma}{\mathrm{d}s}(\tilde{s}) \mathrm{d}\tilde{s}.$$

As we know the specific stretched fibre length L_i, in combination with Equation (7.11) we have the condition

$$L_i = \int_0^{l_i} \left\| \frac{\mathrm{d}\xi_i}{\mathrm{d}s}(s) \right\| \mathrm{d}s = \int_0^{l_i} \left\| \frac{\mathrm{d}\gamma_i}{\mathrm{d}s}(s) \right\| \mathrm{d}s.$$

Here we used the fact that $Q \in \mathrm{SO}(\mathbb{R}^3)$ defines a rotation matrix and, therefore, the norm is invariant. The crimp amplitude c_i in Equation (7.13) may be evaluated by solving

$$f(c_i) = L_i,$$

with

$$f(c) = \int_0^{l_i} \sqrt{1 + c^2 (C_i \pi)^2 \cos^2(C_i \pi s)} \, \mathrm{d}s.$$

We see that f is monotonically increasing with $f(0) = l_i < L_i$ and

$$f(c) > \int_0^{l_i} c(C_i \pi) |\cos(C_i \pi s)| \mathrm{d}s > L_i,$$

for some c large enough. Thus, by the mean value theorem, there exists a unique c_i with $f(c_i) = L_i$. Figure 7.3 shows the effect of the crimp function in Equation (7.13) on an illustrative fibre curve.

7.7 Summary

In this chapter we have presented a model for the production of an airlay material. This model contains important characteristic properties of the production process and of the material itself and allows for several different fibre types, each with their own material properties. In particular, the fibre crimp is included in the fibre model.
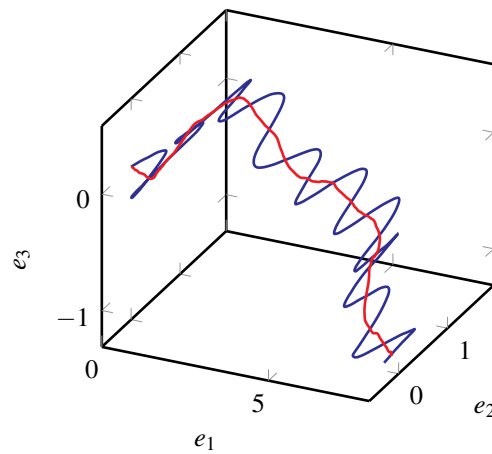
Figure 7.3 – Illustrative example for the effect of added crimp on a single fibre as described in Equation (7.13). The red curve shows a fibre curve without crimp, whereas the blue fibre curve has crimps included.

Several parameters, characterising either the fibres or the material itself, are present in the model. However, not all of them can be directly measured or determined. In the following chapter we describe how the unknown parameters can be estimated from experiments or computer simulations, before we apply the model to real data in Chapter 9.

8

Parameter identification

As we will see in Chapter 9, some of the parameters in the model presented in Chapter 7 can be determined directly from physical measurements. Accurately estimating the remaining parameters, which cannot be directly determined from measurements, is essential for a realistic virtual material model. We first present the methods used for the identification of the fibre parameters. Then, we show how to estimate the anisotropy parameter for a given set of angles describing the fibre orientation.

8.1   Identification of fibre parameters

In this section we consider a general data set consisting of discretised fibre positions, which can be interpreted as measurements of two–dimensional laid down fibres. Several different parameter identification methods for models of the meltspinning process, in combination with the standard two–dimensional model introduced in Section 2.1.1, have been developed. For example, in BOCK *et al.* (2014) a method considering occupation times and white noise analysis was developed and used to determine the parameters in the model. For our method, we first assume that we have a given step size $\tilde{\Delta}_i$ for the discretisation of a fibre curve for the given data set containing the discretised fibre positions. Furthermore, for simplicity, we make the assumption that each fibre type has the same number of simulated fibres K and the same number of discretisation points J. In the following we denote the position of the i–th fibre type, k–th fibre and j–th discretisation point along a fibre curve for the data by $\tilde{r}_{i,k}^{j}$. Furthermore, we denote all discretisation points for the position of the i–th fibre type and the k–th fibre by $\tilde{r}_{i,k}$ and denote all the positions for the i–th fibre type by $\tilde{r}_i = (\tilde{r}_{i,1}, \ldots \tilde{r}_{i,K})$. In addition to the fibre positions, fibre orientations are also needed for the parameter estimation. We denote the orientation angle of the vector $\tilde{r}_{i,k}^{j+1} - \tilde{r}_{i,k}^{j}, j \in \{1, \ldots, J-1\}$ by $\tilde{\alpha}_{i,k}^{j}$. Additionally, all orientations of the i–th fibre type and the k–th fibre are denoted by $\tilde{\alpha}_{i,k}$ and we denote all the orientations for the i–th fibre type by $\tilde{\alpha}_i = (\tilde{\alpha}_{i,1}, \ldots \tilde{\alpha}_{i,K})$.

In the fibre model described in Section 7.6, there are several parameters which have to be identified and directly relate to the data $\tilde{r}_i$ and $\tilde{\alpha}_i$. The noise amplitude A^i relates to the change of fibre orientation whereas the standard deviations $\sigma_{1,i}$ and $\sigma_{2,i}$ relate to the deviation of the fibre end point from the fibre origin. To calculate these parameters, we

proceed in a similar manner to KLAR, MARHEINEKE, *et al.* (2009) and MARINGER (2013) and compute

$$
(\sigma_{1,i}, \sigma_{2,i}) = \left(\sqrt{\sum_{k=1}^{K} \frac{\left(\left(\tilde{r}_{i,k}^{1} - \tilde{r}_{i,k}^{J} \right) \cdot e_1 \right)^2}{K}}, \sqrt{\sum_{k=1}^{K} \frac{\left(\left(\tilde{r}_{i,k}^{j} - \tilde{r}_{i,k}^{J} \right) \cdot e_2 \right)^2}{K}} \right),
$$

$$
A^{i} = \max_{1 \le h \le J} \sqrt{\sum_{k=1}^{K} \sum_{j=1}^{J-1-h} \frac{\left(\tilde{\alpha}_{i,k}^{j+h} - \tilde{\alpha}_{i,k}^{j} \right)^2}{K(J-h)h\tilde{\Delta}_i}}.
$$

(8.1)

From Section 2.1 we know that the spatial stationary solution for the two–dimensional fibre model is given by $\rho_\infty(x) = Ce^{-V(x)} = Ce^{-x^T\Sigma^{-1}x}$, see Equation (2.5). Here C is a normalisation constant for the density ρ_∞ and the covariance matrix is given by $\Sigma = \mathrm{diag}\left\{\sigma_1^2, \sigma_2^2\right\} \in \mathbb{R}^{2\times 2}$. By choosing the initial points for the fibres in our model to be ρ_∞ – distributed, in contrast to MARINGER (2013), no parameter optimisation is needed. We do not have enough information at hand to estimate $\sigma_{3,i}$, as the data sets $\tilde{r}_i$ only contain two–dimensional information. Therefore, it has to be chosen.

8.2 The orientation distribution

In this section we describe a method to identify the characteristic orientation distribution, necessary for the material model introduced in Chapter 7. In particular, we show possible methods of identifying the anisotropy parameter B for the material model introduced in Chapter 7. We first review an existing method based on a variance estimator. Then, we develop a new method based on a maximum likelihood estimator. Finally, in Section 8.2.3, we compare both methods.

Similarly to the case of the parameter $\sigma_{3,i}$, the anisotropy parameter B cannot be determined from the data sets $\tilde{r}_i$ and $\tilde{\alpha}_i$. This is due to the fact that these data sets only provide two–dimensional data in the lay down regime. In contrast to $\sigma_{3,i}$, the value of B is linked to information for the spatial orientation of the fibres which, in practice, is available as we will see in Chapter 9.

We assume that there exits a *main orientation plane* in which most fibre parts are oriented. The deviation angles of the fibre parts from this main orientation plane are denoted by $\Theta = (\theta_1, \ldots, \theta_{N_\Theta})$ with $\theta_j \in [0, \pi), j \in \{1, \ldots N_\Theta\}$. The value $\theta_j = 0$ corresponds to an orientation orthogonal to a main orientation plane and $\theta_j = \pi/2$ to a fibre orientation within the main orientation plane. In general a distinction between the different fibre types in the orientation angle data is not possible. Therefore, we assume that the anisotropy parameter B is the same for all fibre types. In addition, we assume that the expectation for

Θ is $\pi/2$ and coincides with the orientation of the main orientation plane. As the fibre geometry is given as described in Section 7.6, the stationary orientation distribution is given by

$$\rho_B(\theta) = C(B)(\sin\theta)^{\frac{1}{B}},$$
$$C(B) = \left(\int_0^\pi (\sin\theta)^{1/B} \, d\theta\right)^{-1}, \tag{8.2}$$

which can be obtained by integrating Equation (2.28) with respect to the space variable.

8.2.1 The variance estimation

To determine the anisotropy parameter B, in KLAR *et al.* (2012a) and MARINGER (2013) a variance estimator was used. Due to the symmetry of ρ_B, a simple computation yields the expectation

$$\mu = \int_0^\pi \rho_B(\theta)\theta \, d\theta = \frac{\pi}{2}, \tag{8.3}$$

for all $B \in (0,1]$. This corresponds to a fibre orientation in the main orientation plane. Thus, the variance of ρ_B is given by

$$\sigma_B^2 = \int_0^\pi \rho_B(\theta)\left(\theta - \frac{\pi}{2}\right)^2 \, d\theta. \tag{8.4}$$

We assume that a density ρ_Θ is associated to the data set Θ. By the assumption on the expectation of the data set Θ, the variance for ρ_Θ is given by

$$\sigma_\Theta^2 = \int_0^\pi \rho_\Theta(\theta)\left(\theta - \frac{\pi}{2}\right)^2 \, d\theta. \tag{8.5}$$

Then, a variance estimator for B with respect to the given data Θ is given by

$$B_{\mathrm{var}} = \mathrm{argmin}_{B\in(0,1]}\left(\sigma_B^2 - \sigma_\Theta^2\right)^2. \tag{8.6}$$

8.2.2 A likelihood estimator

Although we have seen how the anisotropy parameter B can be estimated by a variance estimator, we now pursue a different method by using a classical approach for parameter estimation in statistics, namely the maximum likelihood method. A general introduction can be found, for example, in GEORGII (2009). This method has the advantage over the variance method, described in the previous section, in that one can directly work on the measured data set Θ and does not need to approximate the angular distribution ρ_Θ. For the

angles Θ, we define the likelihood function as

$$f(B|\Theta) = \prod_{i=1}^{N_\Theta} C(B) \left(\sin\theta_i\right)^{1/B}. \tag{8.7}$$

In general it is more convenient to work with the log–likelihood function which we define as

$$
\begin{aligned}
lf(B|\Theta) &= N_\Theta \log\left(C(B)\right) + \sum_{i=1}^{N_\Theta} \log\left(\left(\sin\theta_i\right)^{1/B}\right), \\
&= N_\Theta \log\left(C(B)\right) + \frac{1}{B}\sum_{i=1}^{N_\Theta} \log\left(\sin\theta_i\right).
\end{aligned}
\tag{8.8}
$$

Then, the log–likelihood estimator B_{mlh} is given by

$$B_{\mathrm{mlh}} = \mathrm{argmax}_{B\in(0,1]} \, lf(B|\Theta). \tag{8.9}$$

One can easily see that a maximiser of Equation (8.7) is also a maximiser of Equation (8.8) and vice versa. To find a maximiser, we consider the derivative of $lf(\cdot|\Theta)$ and solve

$$\frac{\mathrm{d}lf}{\mathrm{d}B}(B|\Theta) = N_\Theta \frac{C(B)}{B^2} \int_0^\pi \log(\sin\theta)\,(\sin\theta)^{1/B}\,\mathrm{d}\theta - \sum_{i=1}^{n} \frac{\log(\sin\theta_i)}{B^2} = 0,$$

or equivalently

$$\int_0^\pi \log(\sin\theta)\rho_B(\theta)\mathrm{d}\theta = \frac{1}{N_\Theta}\sum_{i=1}^{N_\Theta} \log(\sin\theta_i). \tag{8.10}$$

This can be done numerically by choosing an appropriate quadrature rule for the integral on the left hand side of Equation (8.10). Unlike the variance estimator, no approximation for ρ_Θ is needed for the likelihood estimator. Instead the measurements Θ are directly used.

8.2.3   Comparison

We present an example using the parameter estimation methods presented in Sections 8.2.1 and 8.2.2 in order to compare both methods. We use the case $n_B := \dfrac{1}{B} \in \mathbb{N}$ as in this case the primitive function for $(\sin\theta)^{n_B}$ is explicitly known. Thus, we can generate random orientations $\widetilde{\Theta} = \left(\theta_1,\ldots,\theta_{N_{\widetilde{\Theta}}}\right)$ with $\theta_j \in [0,\pi)$, $j \in \{1,\ldots,N_{\widetilde{\Theta}}\}$ with respect to the density ρ_B, which we can use as a sample for testing both methods. For n_B we obtain (BRONSTEIN

B	B_{var}	B_{mlh}	σ_B^2	$\sigma_{\widetilde{\Theta}}^2$
1	1.0000	1.0000	0.4674	0.4631
0.5000	0.5169	0.5034	0.3225	0.3225
0.3333	0.3671	0.3618	0.2452	0.2479
0.2500	0.2397	0.2402	0.1975	0.1953

Table 8.1 – Comparison of the results for both the variance and the maximum likelihood estimators.

et al., 2005)

$$\int_0^{\pi/2} (\sin\theta)^{n_B}\, d\theta = \begin{cases} \dfrac{\pi}{2} \displaystyle\prod_{i=1}^{\frac{n_B}{2}} \dfrac{2i-1}{2i}, & n_B \text{ even}, \\[2em] \displaystyle\prod_{i=1}^{\frac{n_B-1}{2}} \dfrac{2i}{2i+1}, & n_B \text{ odd}. \end{cases} \tag{8.11}$$

So we are able directly to compute the normalization constant $C(B)$ for ρ_B in Equation (8.2). In this case a closed expression for the variance σ_B exists and is given by (KLAR *et al.*, 2012b; MARINGER, 2013)

$$\sigma_B^2 = \begin{cases} \dfrac{\pi^2}{12} - \dfrac{1}{2} \displaystyle\sum_{j=1}^{\frac{n_B}{2}} \dfrac{1}{j^2}, & n_B \text{ even}, \\[2em] \dfrac{\pi^2}{4} - 2 \displaystyle\sum_{j=1}^{\frac{n_B+1}{2}} \dfrac{1}{(2j-1)^2}, & n_B \text{ odd}. \end{cases} \tag{8.12}$$

Both methods, the likelihood estimation and the variance estimator, show good results, see Table 8.1. The first column contains the values B used to generate the angular data $\widetilde{\Theta} = \left(\widetilde{\theta}_1, \ldots, \widetilde{\theta}_{N_{\widetilde{\Theta}}} \right)$ with $N_{\widetilde{\Theta}} = 1000$ using the exact integration formula given by Equation (8.11). The second column shows the estimated parameter B_{var} computed with the variance method. Here the variance $\sigma_{\widetilde{\Theta}}^2$ was computed by representing $\rho_{\widetilde{\Theta}}$ as a histogram and computing the integral given by Equation (8.5) explicitly. The third column is the result of using the likelihood estimator and the fourth column shows the exact variance σ_B^2 given by Equation (8.12) for the chosen B from the first column. The final column shows the result for B_{var} from the variance estimator. Comparing the values in the second and third columns with those in the first column, we see a good agreement of both estimated values B_{var} and B_{mlh} with B. The values in the final two columns, σ_B^2 and $\sigma_{\widetilde{\Theta}}^2$, also show good agreement for a variety of values of B. These results indicate that the maximum

likelihood estimator method is, in addition to the variance method, is a valid method.

8.3   Summary

In this chapter we introduced methods to estimate several parameters for the fibre and material model introduced in Chapter 7 which are not directly available or measurable. In Section 8.1 we began by describing a method for estimating the parameters for the fibre model. Then, in Section 8.2 we developed a maximum likelihood method to estimate the anisotropy parameter B for a given set of angles and compared this method to an existing variance estimator. Comparison showed that both methods are accurate. In contrast to the variance estimator, the maximum likelihood method works directly with the given data set. Thus, we use this method in the remainder of the thesis.

In the next chapter we will apply the methods presented in this chapter to different industrial scenarios and present examples for the generation of virtual fibrous materials.

9 Numerical results

Simulations of virtual airlay fabrics can act as a basis for virtual tensile strength tests or other test scenarios, which can give a further insight into the material properties and help further improve the materials produced or the production process. Having detailed how the unknown parameters in the model presented in Chapter 7 can be determined, we now turn our attention to virtually simulating airlay materials. Our aim is to reproduce three different example materials produced by AUTEFA Solutions. We start by specifying and estimating the model parameters, using information and data provided by our collaborators, before presenting simulation results. Validation and further testing of these virtual materials are performed by Prof. Dr. Leugering, and preliminary results along with details on the complete modelling and simulation chain within the OPAL project can be found in GRAMSCH *et al.* (2016).

The production of airlay fabrics is a complex process. Several different fibre types are normally used which are usually sourced from recycled materials. To gain a better understanding of the process, we consider an idealised scenario supported by three separate experiments performed by AUTEFA Solutions, where the material contains only two fibre types. The first fibre type is a *bicomponent fibre*, which has a melting coating. The second fibre type does not have this property, and, thus, we refer to it as a *solid fibre*. Upon heating the bicomponent fibres melt, forming one structure once cool as discussed in Chapter 6. To distinguish between the two fibre types, we indicate the bicomponent and the solid fibres, as well as their corresponding properties, with index $i = 1$ and $i = 2$ respectively. Using the notation of Chapter 7, we have $N = 2$. We call the three different material samples, produced by AUTEFA Solutions by altering the machine settings which resulted in different macroscopic properties, V1, V2 and V3.

Now we detail the fibre properties and machine settings for the three experiments considered.

9.1 Fibre properties and machine settings

Several fibre parameters for both fibre types were provided by IDEAL Automotive, where both the mean value and the variance were given. However, for simplicity we only use the averaged quantities. Table 9.1 details all the fibre parameters of interest for our model.

Symbol	Unit	$i = 1$	$i = 2$
$(\rho\,A)_i$	kg/m	$4.4 \cdot 10^{-7}$	$6.7 \cdot 10^{-7}$
l_i	m	$5.1 \cdot 10^{-2}$	$5.1 \cdot 10^{-2}$
L_i	m	$6 \cdot 10^{-2}$	$6 \cdot 10^{-2}$
C_i	arcs/m	$7 \cdot 10^{2}$	$5 \cdot 10^{2}$
$\beta_{m,i}$	-	0.3	0.7

Table 9.1 – Mean values for the fibre parameters, provided by IDEAL Automotive, used in all numerical simulations.

Symbol	Unit	V1	V2	V3
v_{belt}	m/min	9.9	2	1
a	m	2.4	2.4	2.4
$\dot{m}$	kg/h	288	173	259

Table 9.2 – Machine parameters, provided by AUTEFA Solutions, used in all numerical simulations.

The two fibre types have the same fibre length, but differ in the line density $(\rho\,A)_i$ and the crimp number C_i. Different machine settings lead to different materials with different properties. The machine settings used for the three experiments V1 – V3 are summarised in Table 9.2. The belt width a is the same for all three experiments, whereas all the other values vary.

9.2 Parameters from fibre flight simulations

Not only do the fibre properties and machine settings have a large influence on the resulting material, but the fibre flight and the resulting lay down positions also play an important role. In particular, the distribution densities for the lay down positions and several fibre parameters depend strongly on the fibre flight. The Department of Transport Processes, Fraunhofer ITWM provided fibre flight data for the three separate scenarios under consideration. The method used is described in detail in GRAMSCH *et al.* (2016) for the experiment V2 and the same method was also used for the experiments V1 and V3. Fibre flight simulations for each experiment were performed in FIDYST (Fraunhofer ITWM) using $K = 1000$ fibres of each kind where each fibre is represented by $J = 51$ discretisation points.

9.2.1 The estimation of distribution densities

Accurate fibre distribution densities g_i are essential to give the correct fibre placement in the reference volume for the mathematical model of an airlay fabric, introduced in
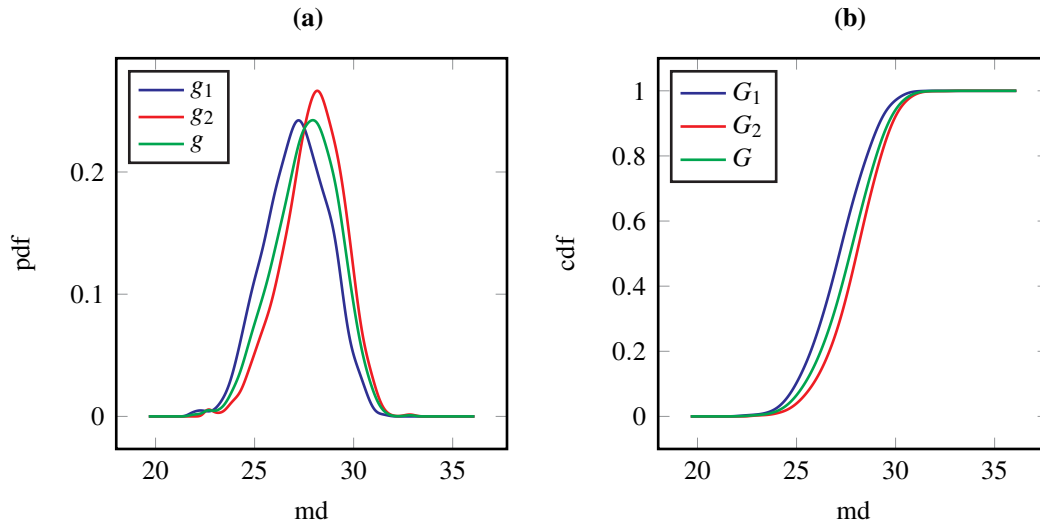
Figure 9.1 – The probability and cumulative distribution functions for the experiment V1, denoted by pdf and cdf respectively. The coordinate axis in the machine direction is indicated by md. The graphs corresponding to the bicomponent fibres are indicated in blue, whereas the ones for the solid fibres are indicated in red. The convex combinations of both fibre types are displayed in green.

Chapter 7. However, FIDYST simulation results for the fibre flight consist of coordinates for every single fibre instead of distribution densities. To obtain the distribution densities g_i we only consider the coordinates in the machine direction. In particular, we only consider the initial points of the fibres as reference points for each fibre and then compute an estimator for g_i with the MATLAB (2015) built–in function fitdist using a kernel density estimation on compact support. In Figures 9.1, 9.2 and 9.3 we can see the distributions for the experiments V1–V3. Figures 9.1(a), 9.2(a) and 9.3(a) show the probability distribution functions, whereas in Figures 9.1(b), 9.2(b) and 9.3(b) the cumulative distribution functions are shown. We can see that the bicomponent fibre distribution sits to the left of the solid fibre distribution. This means that the solid fibres have a tendency to fly further away from their leaving point at the card cylinder than the bicomponent fibres. Thus, one may assume that there are more bicomponent than solid fibres at the base of the material. For positions further up in the material we expect this ratio to change until, at the top of the material, there should be mainly solid fibres.

In addition to the functions corresponding to the bicomponent and solid fibres, the convex combinations with respect to the number ratios $\beta_{n,1} = 0.4011$, $\beta_{n,2} = 0.5989$ (see Equation (7.9)) are also shown.

9.2.2 Estimating fibre parameters

As we have seen in Chapter 7.6, several parameters need to be estimated using the methods introduced in Section 8.1 either from experimental data or other numerical simulations.
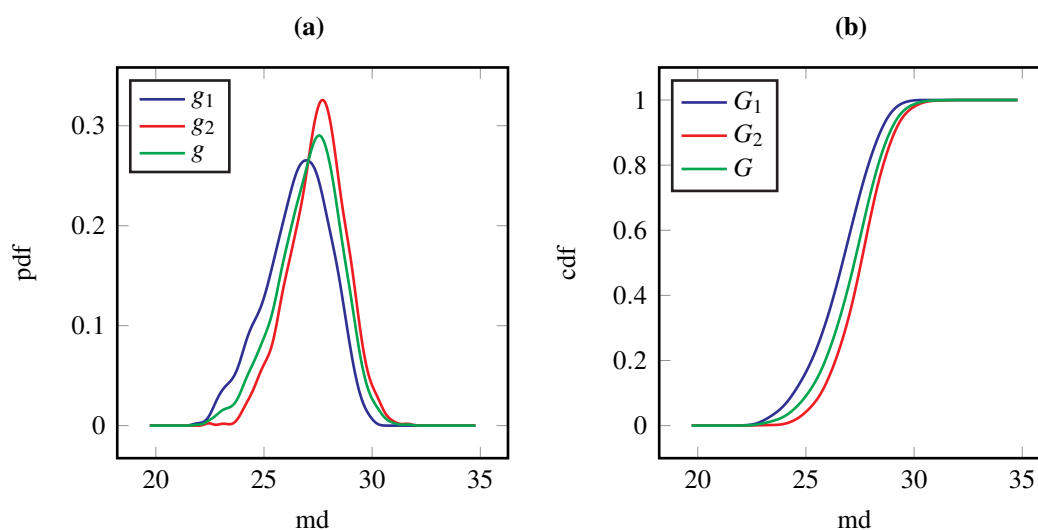
(a)   **(b)**

Figure 9.2 – The probability and cumulative distribution functions for the experiment V2, denoted by pdf and cdf respectively. The coordinate axis in the machine direction is indicated by md. The graphs corresponding to the bicomponent fibres are indicated in blue, whereas the ones for the solid fibres are indicated in red. The convex combinations of both fibre types are displayed in green.

(a)   **(b)**
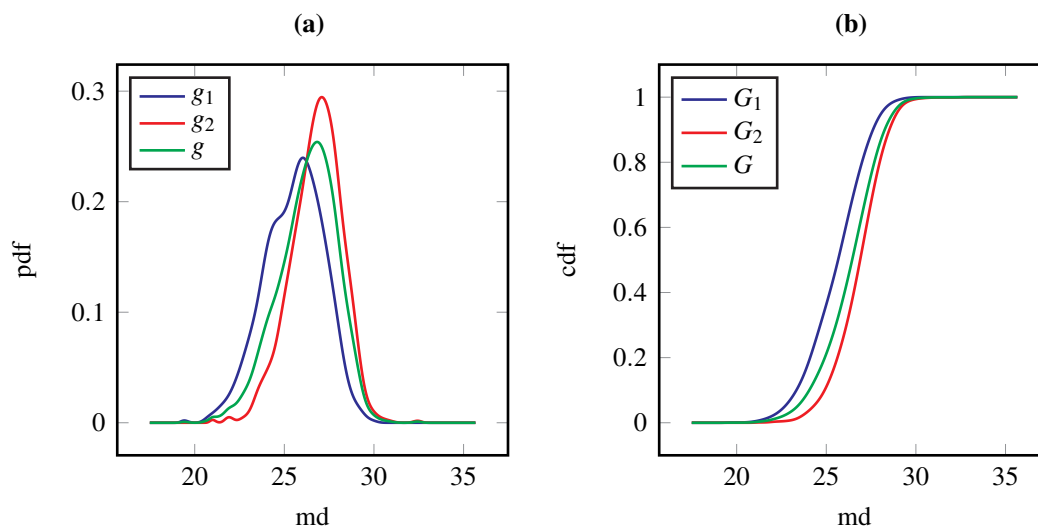
Figure 9.3 – The probability and cumulative distribution functions for the experiment V3, denoted by pdf and cdf respectively. The coordinate axis in the machine direction is indicated by md. The graphs corresponding to the bicomponent fibres are indicated in blue, whereas the ones for the solid fibres are indicated in red. The convex combinations of both fibre types are displayed in green.

Symbol	Unit	$i = 1$			$i = 2$		
		V1	V2	V3	V1	V2	V3
$\sigma_{1,i}$	cm	1.0941	0.9992	1	1.2106	1.0812	1
$\sigma_{2,i}$	cm	1.0388	1.022	1	1.1957	1.1967	1
A^i	cm$^{-1/2}$	2.9380	2.8550	3.5002	2.2771	2.3445	2.6003

Table 9.3 – Estimated fibre parameters for all settings determined from the FIDYST simulation data using the methods detailed in Chapter 8.

The parameters which can be directly estimated from FIDYST data are the noise amplitudes A^i and the throwing ranges $\sigma_{1,i}$ and $\sigma_{2,i}$, where we use the data of fibres already laid down on the belt. The values of these parameters are summarised in Table 9.3.

9.3   The fibre orientation distribution

In contrast to the fibre parameters described in Section 9.2.2, the anisotropy parameter B cannot be obtained from the FIDYST simulation results as it only gives two–dimensional laid down fibres. Therefore, to estimate B, we need additional information about the three–dimensional structure of the material. Fibre orientations within the material can be determined from μ–CT scans and image analysis. Methods for the analysis of μ–CT data of fibrous materials have previously been developed. Several papers deal with the image processing of fibrous materials (SCHLADITZ *et al.*, 2006; PEYREGA *et al.*, 2009; ALTENDORF and JEULIN, 2009; REDENBACH and VECCHIO, 2011; REDENBACH, RACK, *et al.*, 2012; REDENBACH, SCHLADITZ, *et al.*, 2014; VECCHIO, 2014). A good review of the methods used in image processing, as well as the statistical description of material structures up to the year 2009 can be found in OHSER and SCHLADITZ (2009). Many of the methods developed and the results reported in these publications have been included in the software tool MAVI (Fraunhofer ITWM) which was developed and used by the Department of Image Processing, Fraunhofer ITWM for the analysis of the μ–CT data of our material sample.

Before applying the maximum likelihood estimator developed in Chapter 8, we first, in Section 9.3.1, explain how the information from the μ–CT scan was obtained and then, in Section 9.3.2, how this information is evaluated to determine the anisotropy parameter B.

9.3.1   Micro computer tomography data

Micro computer tomography is needed to gain information about the fibre orientation in the material. For the μ–CT analysis, a material sample of height 8.67 mm was taken from

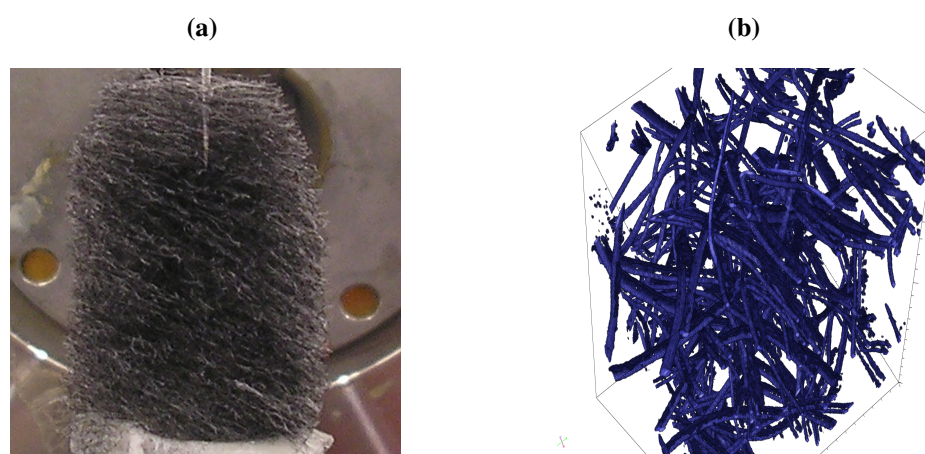**(a)**   **(b)**

Figure 9.4 – Illustration of the image processing: in Figure 9.4(a) one can see the material sample V2 prepared for micro computer tomography. Figure 9.4(b) shows a small sample of the processed and visualised fibre data. Images reproduced with the permission from the Department of Image Processing, Fraunhofer ITWM.

0.87 mm under the surface of the material to prevent boundary effects. Each pixel has an edge length of 4.66 μm in the processed image and a tuple of orientation angles is associated with each pixel. In total, the sample has a size of $2500 \times 2300 \times 1860$ pixels. It was not possible to distinguish the different fibre types within the scan, and so it was not possible to judge the influence of each fibre type on the fibre orientation distribution. Thus, we assume the evaluated anisotropy parameter B to be the same for all the fibre types which compose the material. The anisotropy parameter, therefore, should be seen as a material rather than a fibre parameter. In Figure 9.4 we can see images of the material sample prepared for μ–CT and the processed and visualised fibre data, both provided by the Department of Image Processing, Fraunhofer ITWM. In Figure 9.4(a) the single layers are visible. Note that the part where the μ–CT data is actually obtained from is much smaller than the sample in the image. The additional material is only needed for technical purposes.

9.3.2 The data evaluation

After the image processing of the μ–CT data we obtained a large data set containing the information of the fibre orientation for every single pixel. To make it feasible to process the data, we divide the data set into 241 subsets with a million entries each. This way we can also see if there are differences in different parts of the sample. We assume that the material sample used for the μ–CT analysis contains a single material layer, which is not necessarily parallel to the belt. This assumption is motivated by the small size of the material sample. In order to ensure that the data fulfils the conditions in Section 8.2, we perform a sequence of post processing steps. In contrast to the measurements, two
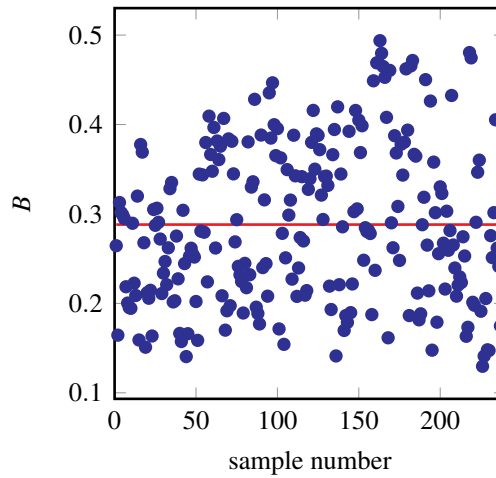
Figure 9.5 – Visualisation of estimated values of B for different sample sets of V2 (blue dots). The red dashed line indicates the average value $B = 0.288$ which we use for the simulations.

orientations at each point are possible for a real fibre. Thus, in addition to the orientation given for each pixel, we also consider the opposite orientation. Furthermore, we identify the main lay down plane. As the material layer and, thus, the main lay down plane is not necessarily parallel to the belt, we rotate the orientation vectors of each pixel so that an angle $\theta = \pi/2$ is identical to an orientation in the main lay down plane. Once the data is in the appropriate form, we perform a parameter estimation based on the likelihood method introduced in Section 8.2.2 on each subset. From all the results we take the average to obtain an estimator for the anisotropy parameter B. The results for each subset and the resulting averaged value of $B = 0.288$ can be seen in Figure 9.5. As we only have the data from a single μ–CT of the material sample V2, we use this data for all the simulations.

9.4 Numerical simulations

Before proceeding to discussing the numerical methods employed and presenting results, we need to prescribe the initial conditions and discuss the choice of numerical parameters.

9.4.1 The initial lay down positions

To account for all the different possibilities for the initial lay down positions in the machine and the cross direction, we replace $x \in \mathbb{R}^3$ and $y \in \mathbb{R}^3$ in Equation (7.12) by the random variables X_i and Y_i, and choose them to be g_i– and uniformly–distributed on $[-d_i/2, d_i/2]$ respectively. Then, each fibre is described by

$$\phi_s[X_i, Y_i, t] = S(X_i)\left(\zeta_i(s) - \zeta_i(0)\right) + \begin{pmatrix} X_i - \chi_i(t) \\ Y_i \\ R(X_i) \end{pmatrix}.$$

9.4.2 Numerical parameters

Before we can proceed to performing numerical simulations we first have to specify several additional parameters in material model introduced in Chapter 7. We have to discretise the time interval of the production process $[0, T_i]$ for the i–th fibre type. This is done by introducing the constant simulation time step $\Delta t_i \in \mathbb{R}$ which should be small with respect to T_i to obtain a regular fibre distribution in the whole material due to the belt movement.

As the lay down positions are given by the random variables X_i and Y_i, we perform $p_i \in \mathbb{N}$ realisations for each of the random variables per time step Δt_i. Therefore, the simulation time step Δt_i has to be chosen with respect to the number of realisations p_i, the simulation time T_i and the total number of fibres n_i. This is achieved by setting

$$\Delta t_i = p_i \frac{T_i}{n_i}.$$

For simplicity, in Equations (7.4) and (7.10) we replace $x_{min,i}$ and $x_{max,i}$ by x_{min} and x_{max} respectively. Therefore, the considered time T_i and the position of the centre of the reference volume χ_i become independent of the fibre type without changing the numerical results.

As the standard deviation $\sigma_{3,i}$ cannot be determined from either the FIDYST simulations or the μ–CT data, we have to choose a value. We assume that the value of $\sigma_{3,i}$ is rather small in comparison to $\sigma_{1,i}$ and $\sigma_{2,i}$ and make the assumption $\sigma_{3,i} = 0.1\ \sigma_{2,i}$. In addition, we have to specify the simulation step size for the fibre generation Δ_{micro} and the number of realisations per time step p_i. In general, the step size Δ_{micro} has to be small and the number of realisations large enough to obtain accurate results. Furthermore, we have to choose the size of the reference volume V. On the one hand it needs to be large enough to be representative for further tests and to include enough parts of both fibre types so that adhesive joints exist. On the other hand, if it is too large numerical simulation becomes very computationally expensive. In particular, the reference volume needs to be small enough that the computationally expensive virtual tensile strength tests are still feasible in a reasonable amount of time. All the parameters used in our simulations, additional to those given in Tables 9.1 and 9.2, are summarised in Table 9.4.

Symbol	Unit	$i = 1$			$i = 2$		
		V1	V2	V3	V1	V2	V3
B	-	0.288					
Δ_{micro}	cm	0.01					
Δt_i	-	0.0021	0.0035	0.0023	0.0014	0.0023	0.0015
H	cm	1.5	6	10	1.5	6	10
p_i	-	100			100		
d	cm	0.5					
T_i	s	1.4083	6.6593	12.2889	1.4083	6.6593	12.2889
$x_{min,i}$	cm	19.6599	19.7231	17.4945	20.3527	20.2099	18.9105
$x_{max,i}$	cm	34.5546	32.8646	32.8858	36.0981	34.7733	35.6618
$\beta_{n,i}$	-	0.4011			0.5989		
n_i	-	67676	192225	660714	101063	287056	986666

Table 9.4 – Estimated parameters for the three different materials V1–V3

9.4.3 Numerical results

Using the parameters given in Tables 9.1 – 9.4, we now present numerical results for the three virtual materials V1, V2 and V3 in Figure 9.6, performed using MATLAB (2015) The bicomponent fibres are shown in blue while the solid fibres are shown in red. In the first row of figures, the full reference volumes of the three virtual materials are shown with a maximal height of 10 cm, which is the full height of the material V3. The material in Figure 9.6(a) appears to be rather homogeneous. However, as the height H increases, we see that the material appears more heterogeneous, see Figures 9.6(b) and 9.6(c). We note that the base of the virtual material V3 is mostly blue and, therefore, mainly consists of bicomponent fibres. This can particularly be seen by examining Figures 9.6(d)–9.6(f), which show the base portion of Figures 9.6(a) – 9.6(c) respectively. The material V1 has predominately red fibres at the base of the material, whereas the material V2 has predominately blue fibres. This effect is due to the difference in the distribution densities as shown in Figures 9.1–9.3 and explained in Section 9.2.1.

9.5 Summary

In this chapter we presented details on the numerical implementation and application of the material model developed in Chapter 7 to three different scenarios. We described how to obtain several parameters from experiments and further computer simulations, before we presented some numerical results for the three different scenarios considered.
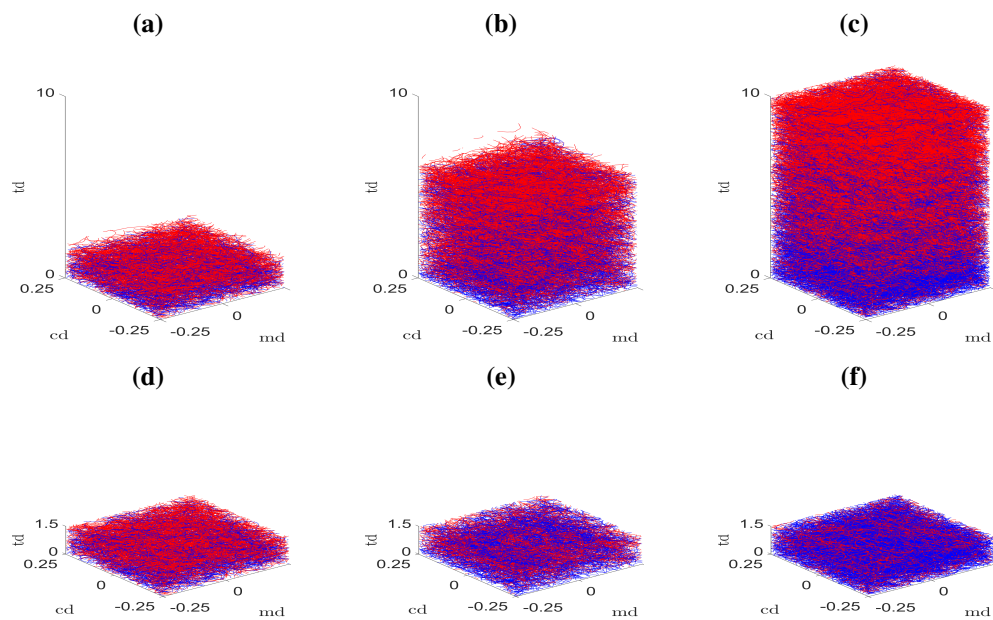
Figure 9.6 – The simulated material structure for the experiments V1–V3, where the bicomponent fibres are shown in blue and the solid fibres in red. Figures 9.6(a) and 9.6(d) show the experiment V1, Figures 9.6(b) and 9.6(e) show the experiment V2, and Figures 9.6(c) and 9.6(f) show the experiment V3. The first row, Figures 9.6(a)–9.6(c), shows the complete material columns where the maximal value of the td axis is 10 cm. The second row, Figures 9.6(d)–9.6(f), shows the bottom portions of the materials up to a height of 1.5 cm.

10 Conclusion

10.1 Summary

Although several models describing fibrous materials exist, to our knowledge there are no models specifically designed for the airlay production process. In this part of the thesis we developed a novel material model tailored to the specific requirements of the airlay production process. The collaboration with industry experts meant that we had access both to information on the material settings and results from experiments performed on the samples. By using a microscopic description, where each individual fibre in the material is described, the specific fibre properties could be built into our model. Furthermore, information about the fibre orientation, stemming from μ–CT could be included. By using a new maximum likelihood estimator, as opposed to the existing variance estimator, we were able to identify the anisotropy parameter describing the distribution of the fibre orientation directly from μ–CT data. A specific challenge in modelling the airlay process is that, due to the fibre flight, the single fibres are distributed on the belt. This effect was accounted for by coupling our material model to the FIDYST simulation package. This allowed us to develop a realistic material model, which was then used to simulate three virtual material samples with the aim of quantitatively reproducing three materials produced by our industrial partners. Such virtual materials allow for virtual tensile strength tests, performed by our collaborators.

10.2 Future work

There are several possible avenues for extending and developing the work on airlay materials presented in this thesis. We first discuss possible improvements and extensions to the model itself in Section 10.2.1. Then, in Section 10.2.2, we discuss several possibilities for the verification and application of the material model developed.

10.2.1 Modelling improvements

The measurements of the fibre properties provided by IDEAL Automotive consisted of a mean value and variance. In Chapter 9, for simplicity, we just used the mean value provided. The model could be improved by replacing the mean parameters with random variables drawn from corresponding parameter distributions. This would allow for an

examination of the effect of this variation on the material properties. However, one would need to make assumptions on the parameter distributions and, thus, significant further testing and analysis of the fibre material would need to be performed.

It was neither possible to identify the parameter $\sigma_{3,i}$ from the fibre data nor from the μ–CT data, as explained in Chapter 8. Therefore, in Chapter 9 we chose a value for $\sigma_{3,i}$ which seemed reasonable. An option to overcome this problem would be to use additional information from the μ–CT data. By applying fibre segmentation algorithms to the μ–CT data as described in ALTENDORF (2011), it may be possible to describe the spatial fibre distribution.

As described in Chapter 9 the anisotropy parameter B for the material sample V2 was obtained from the μ–CT data and also used for the simulation of the materials V1 and V3, too. This method has two main drawbacks. Firstly, μ–CT is expensive and can only be performed on small samples. Secondly, information obtained from μ–CT only holds for a given sample, and so the parameter B estimated may not be accurate for a different sample of the same or a different material. To overcome this issue, one could neglect the μ–CT data and use a two–dimensional fibre model. Of course, this would lead to the loss of the third space dimension in the model. However, despite these drawbacks, the information obtained from μ–CT in combination with computer simulations can be a very important tool in the design of airlay fabrics. For example, keeping the anisotropy parameter B constant, one could vary the other parameters describing the fibres or machine setup, and analyse the effect of these parameter variations on the properties of the simulated material.

In our model we made the assumption that all the fibres of the same type had the same thickness and length, provided *a priori* by collaborators. However, these properties can change during the production process and vary within the material. In particular, the fibre diameter of bicomponent fibres can change due to the melting of the coating during the thermobonding process. In addition, due to the melting, fibres have a tendency to stick together not only at single points but also along their fibre length. These fibre bundles are common in fibrous materials and have been observed by the Department of Image Processing, Fraunhofer ITWM in the analysed μ–CT data from the material sample V2. Furthermore, it cannot be guaranteed that the fibre length remains the same during the whole production process as the fibres could break. Such effects have already been analysed in different settings. In TALBOT *et al.* (2000) methods for measuring the diameter and the length of insulation mineral fibres based on electron microscopy images were discussed. Furthermore, a method with which the fibre length can be determined from μ–CT data

was introduced in KUHLMANN and REDENBACH (2015). In general, due to the length of the fibres and the small size of samples, it is rare that a full fibre is captured in the μ–CT data. Furthermore, the sample volume is, in general, densely packed. Therefore, a direct approach by fibre segmentation (ALTENDORF, 2011) is probably not sufficient. However, methods have recently been developed which could be used in future. For example, in KUHLMANN and REDENBACH (2015) a new approach was introduced, considering the fibre end point distribution from which the fibre length distribution is estimated. In addition, a method for automatic fibre thickness measurement and a model for fibre generation including fibre bundles was developed in EASWARAN *et al.* (2016).

Although several improvements to the model have been suggested, the addition of further details and the development of a more complex model needs justification to ensure that additions contribute to the behaviour of the material and any additional parameters can be identified.

10.2.2 Model verification and applications

With our model we are able to simulate an airlay material composed of different fibre types with different properties using different machine settings. As detailed in GRAMSCH *et al.* (2016), a preliminary validation was performed by our project partners, the group of Prof. Dr. Leugering at FAU Erlangen, using virtual tensile strength tests as part of the remit of the OPAL project. The methods for such tensile strength tests are described in GRAMSCH *et al.* (2016) and STROHMEYER and LEUGERING (2016). Such tests are based on a graph structure of the material consisting of nodes and edges, where the fibres themselves build the edges of the graph. In the jointly developed method (KLAR, NESSLER, *et al.*, 2016; GRAMSCH *et al.*, 2016), the adhesive joints between the fibres in the virtual material are identified as the nodes of the graph. However, further validation is needed. Other material tests based on computer simulations also could be performed, either for further model verification or as a direct application of our material model. For example, simulations of fluid flow through the material, possible in a software package such as GEODICT (2016), or the measurement of acoustic properties as presented in SCHLADITZ *et al.* (2006) for several different materials, would be useful. A comparison of the results with real life experiments could give further insight into our material model.

10.3 Closing thoughts

The novel material model developed allows for an unlimited number of fibre types and includes various parameters describing fibre properties and machine settings. We showed

that it is possible to connect simulation results from detailed fibre flight simulations with our model which can then be used for further applications.

Overall, by developing the first material model specifically for airlay fabrics, we hope to improve the understanding of such materials in the future and to give a basis for further improvements and developments.

Summary

11 Summary

In this thesis we developed new mathematical models for non–woven materials based on two different production processes. We extended the existing surrogate fibre models for the meltspinning process in Part I and in Part II we developed a new material model for airlay fabrics. As the contents of the two parts have been summarised in detail in Chapters 5 and 10, we only briefly outline the main results here.

We started off this thesis by improving the existing surrogate fibre models by including the thickness of each fibre in Part I. This led to a strongly coupled system of stochastic delay differential equations. The analysis of this system and the corresponding diffusion approximation showed that the interaction strength and the delay length have a big influence on the characteristic behaviour of the system and its convergence to equilibrium. The modelling strategy with continuous delay in the interaction term could further the development of existing models of interacting particle systems for several applications.

In Part II we developed a novel model which describes non–woven materials producing using the airlay process. This model allows for the inclusion of experimental data from the industrial process and μ–CT data through parameter identification. In particular, we were able to couple other simulation tools to our numerical simulations. We are confident that such simulations can facilitate the future development of the production process and the quality of airlay fabrics.

Bibliography

ALTENDORF, H. (2011) *3D morphological analysis and modeling of random fiber networks: applied on glass fiber reinforced composites*. PhD thesis École normale supérieure des Mines de Paris, France and Technische Universität Kaiserslautern, Germany (see pp. 114, 115)

ALTENDORF, H. and D. JEULIN (2009) 3D directional mathematical morphology for analysis of fiber orientations in: *Image Analysis and Stereology*, **28**:3, 143–153 (see p. 107)

ARNOLD, L. (1973) *Stochastische Differentialgleichungen* R. Oldenbourg Verlag (see pp. 7, 8)

BERNE, B. J. and P. PECHUKAS (1972) Gaussian Model Potentials for Molecular Interactions in: *The Journal of Chemical Physics*, **56**:8, 4213–4216 (see p. 76)

BOCK, W., T. GÖTZ, M. GROTHAUS, and U. P. LIYANAGE (2014) Parameter estimation from occupation times – a white noise approach in: *Communications on Stochastic Analysis*, **8**:4, 489–499 (see pp. 5, 97)

BOISSARD, E., P. DEGOND, and S. MOTSCH (2013) Trail formation based on directed pheromone deposition in: *Journal of Mathematical Biology*, **66**:6, 1267–1301 (see p. 76)

BOLLEY, F. (2008) Separability and completeness for the Wasserstein distance in: *Lecture Notes in Mathematics*, **1934**: 371–377 (see p. 60)

BOLLEY, F., J. CANIZO, and J. A. CARRILLO (2011) Stochastic Mean-Field Limit : Non-Lipschitz Forces & Swarming in: *Mathematical Models and Methods in Applied Sciences*, **21**:11, 2179–2210 (see p. 51)

BOLLEY, F., A. GUILLIN, and F. MALRIEU (2010) Trend to equilibrium and particle approximation for a weakly selfconsistent Vlasov-Fokker-Planck equation in: *ESAIM: Mathematical Modelling and Numerical Analysis*, **44**:5, 867–884 (see pp. 49, 54, 55, 60)

BONILLA, L. L. (2000) Chapman-Enskog method and synchronization of globally coupled oscillators in: *Physical Review E*, **62**:4, 4862–4868 (see p. 11)

BONILLA, L. L., T. GÖTZ, A. KLAR, N. MARHEINEKE, and R. WEGENER (2007) Hydrodynamic Limit of a Fokker-Planck Equation Describing Fiber Lay-down Processes in: *SIAM Journal on Applied Mathematics*, **68**:3, pp. 648–665 (see pp. 5, 10, 11)

BORSCHE, R., A. KLAR, C. NESSLER, A. ROTH, and O. TSE (submitted) A Retarded Mean-Field Approach for Interacting Fiber Structures in: *SIAM Journal on Multiscale Modeling and Simulation*, http://arxiv.org/abs/1501.06465 (see pp. 51, 54)

BOUIN, E., F. HOFFMANN, and C. MOUHOT (2016) Exponential decay to equilibrium for a fibre lay-down process on a moving conveyor belt (see p. 11)

BRAUN, W. and K. HEPP (1977) The Vlasov Dynamics and Its Fluctuations in the 1/N Limit of Interacting Classical Particles in: *Communications in Mathematical Physics*, **56**:2, 101–113 (see pp. 49, 51)

BRONSTEIN, I., K. SEMENDJAJEW, G. MUSIOL, and H. MÜHLIG (2005) *Taschenbuch der Mathematik* 6th edition Verlag Harri Deutsch (see p. 100)

CARRILLO, J. A., M. D'ORSOGNA, and V. PANFEROV (2009) Double milling in self-propelled swarms from kinetic theory in: *Kinetic and Related Models*, **2**:2, 363–378 (see pp. 49, 76)

CARRILLO, J. A., A. KLAR, and A. ROTH (2016) Single to Double Mill Small Noise Transitions via Semi-Lagrangian Finite Volume Methods in: *Communications in Mathematical Sciences*, **14**:4, 1111–1136 (see p. 76)

CARRILLO, J. A., A. KLAR, S. MARTIN, and S. TIWARI (2010) Self-Propelled Interacting Particle Systems With Roosting Force in: *Mathematical Models and Methods in Applied Sciences*, **20**:supp01, 1533–1552 (see p. 76)

CARRILLO, J. A. and G. TOSCANI (2007) Contractive Probability Metrics and Asymptotic Behavior of Dissipative Kinetic Equations in: *Notes of the 2006 Porto Ercole Summer School* vol. 6 75-198 (see p. 60)

CERCIGNANI, C. (1990) *Mathematical Methods in Kinetic Theory* 2nd edition Plenum Press (see pp. 11, 31, 53)

CLEAVER, D. J., C. M. CARE, M. P. ALLEN, and M. P. NEAL (1996) Extension and generalization of the Gay-Berne potential in: *Physical Review E*, **54**:1, 559–567 (see p. 76)

CUCKER, F. and S. SMALE (2007) Emergent behavior in flocks in: *IEEE Transactions on Automatic Control*, **52**:5, 852–862 (see p. 32)

DOBRUSHIN, R. (1979) Vlasov equations in: *Functional Analysis and Its Applications*, **13**:2, 115–123 (see pp. 49, 51)

DOLBEAULT, J., A. KLAR, C. MOUHOT, and C. SCHMEISER (2013) Exponential Rate of Convergence to Equilibrium for a Model Describing Fiber Lay-Down Processes in: *Applied Mathematics Research eXpress*, **2**: 165–175 (see p. 10)

EASWARAN, P., M. J. LEHMANN, O. WIRJADI, T. PRILL, S. DIDAS, and C. REDENBACH (2016) Automatic Fiber Thickness Measurement in Scanning Electron Microscopy Images Validated Using Synthetic Data in: *Chemical Engineering & Technology*, **39**:3, 395–402 (see p. 115)

ERBAN, R., J. HASKOVEC, and Y. SUN (2016) A Cucker-Smale model with noise and delay in: *SIAM Journal on Applied Mathematics*, **76**:4, 1535–1557 (see p. 32)

EVANS, L. C. (2013) *An Introduction to Stochastic Differential Equations* American Mathematical Society (see p. 7)

EVERAERS, R. and M. R. EJTEHADI (2003) Interaction potentials for soft and hard ellipsoids in: *Physical review. E, Statistical, nonlinear, and soft matter physics*, **67**:4, 041710– (see p. 76)

FIDYST *Fiber Dynamics Simulation Tool (FIDYST)* `https://www.itwm.fraunhofer.de / en / departments / transport - processes / products / fidyst - fiber - dynamics-simulation-tool.html` Department of Transport Processes, Fraunhofer Institute for Industrial Mathematics (ITWM), Kaiserslautern, Germany (see pp. 83, 104)

GARD, T. (1988) *Introduction to Stochastic Differential Equations* Marcel Dekker Inc (see pp. 7, 8)

GAY, J. G. and B. BERNE (1981) Modification of the overlap potential to mimic a linear site–site potential in: *The Journal of Chemical Physics*, **74**:6, 3316–3319 (see p. 76)

GEODICT (2016) *Math2Market GmbH, Kaiserslautern, Germany* `http : / / www . math2market.de` (see p. 115)

GEORGII, H. (2009) *Stochastik* 4th edition Walter de Gruyter (see p. 99)

GOLSE, F. (2003) The Mean-Field Limit for the Dynamics of Large Particle Systems in: *Journées Équations aux Dérivées Partielles*, 1–47 (see pp. 49, 51)

GOLSE, F. (2012) The Mean-Field Limit for a Regularized Vlasov-Maxwell Dynamics in: *Communications in Mathematical Physics*, **310**:3, 789–816 (see p. 32)

GOLSE, F. (2016) On the Dynamics of Large Particle Systems in the Mean Field Limit in: *Macroscopic and Large Scale Phenomena: Coarse Graining, Mean Field Limits and Ergodicity* ed. by A. MUNTEAN, J. RADEMACHER, and A. ZAGARIS Springer International Publishing, 1–144 (see pp. 49, 51)

GÖTZ, T., A. KLAR, N. MARHEINEKE, and R. WEGENER (2007) A Stochastic Model and Associated Fokker–Planck Equation for the Fiber Lay-Down Process in Nonwoven Production Processes in: *SIAM Journal on Applied Mathematics*, **67**:6, 1704–1717 (see pp. 3, 5, 7, 10, 28)

GRAMSCH, S., A. KLAR, G. LEUGERING, N. MARHEINEKE, C. NESSLER, C. STROHMEYER, and R. WEGENER (2016) Aerodynamic web forming: process simulation and material properties in: *Journal of Mathematics in Industry*, **6**:13, 1–23 (see pp. 81, 83, 103, 104, 115)

GROTHAUS, M. and A. KLAR (2008) Ergodicity and Rate of Convergence for a Non-sectorial Fiber Lay-Down Process in: *SIAM Journal on Mathematical Analysis*, **40**:3, 968–983 (see p. 10)

GROTHAUS, M. and P. STILGENBAUER (2014) Hypocoercivity for Kolmogorov backward evolution equations and applications in: *Journal of Functional Analysis*, **267**:10, 3515–3556 (see p. 10)

GROTHAUS, M. and P. STILGENBAUER (2015) A Hypocoercivity Related Ergodicity Method for Singularly Distorted Non-Symmetric Diffusions in: *Integral Equations and Operator Theory*, **83**:3, 331–379 (see p. 10)

HALANAY, A. (1966) *Differential Equations: Stability, Oscillations, Time Lags* Academic Press (see p. 56)

HÄMÄLÄINEN, J., S. B. LINDSTRÖM, T. HÄMÄLÄINEN, and H. NISKANEN (2011) Papermaking fibre-suspension flow simulations at multiple scales in: *Journal of Engineering Mathematics*, **71**:1, 55–79 (see p. 84)

HÄMÄLÄINEN, J., T. HÄMÄLÄINEN, T. LEPPÄNEN, H. NISKANEN, and J. SORVARI (2014) Mathematics in paper - from fiber suspension fluid dynamics to solid state paper mechanics in: *Journal of Mathematics in Industry*, **4**:1, 14 (see p. 84)

HERTY, M., A. KLAR, S. MOTSCH, and F. OLAWSKY (2009) A smooth model for fiber lay-down processes and its diffusion approximations in: *Kinetic and Related Models*, **2**:3, 489–502 (see pp. 5, 15)

HIETEL, D., M. GÜNTHER, and F. OLAWSKY (2008) Technologiesprung durch Simulation von Fadendynamiken in: *23. Hofer Vliesstofftage*, 1–8 (see p. 4)

HILLEN, T. (2005) On the L^2-Moment Closure of Transport Equations: the General Case in: *Discrete and Continuous Dynamical Systems*, **5**:2, 299–318 (see p. 53)

HILLEN, T. and K. J. PAINTER (2013) Transport and anisotropic diffusion models for movement in oriented habitats in: *Dispersal, Individual Movement and Spatial Ecology: A Mathematical Perspective* ed. by M. A. LEWIS, P. K. MAINI, and S. V. PETROVSKII Springer, 177–222 (see pp. 52, 53)

JØRGENSEN, E. (1978) Construction of the Brownian Motion and the Ornstein-Uhlenbeck Processin a Riemannian Manifold on Basis of the Gangolli-Mc.Kean Injection Scheme in: *Zeitschrift für Wahrscheinlichkeitstheorie und Verwandte Gebiete*, **44**:1, 71–87 (see p. 13)

KÄRKKÄINEN, S., A. MIETTINEN, T. TURPEINEN, J. NYBLOM, P. PÖTSCHKE, and J. TIMONEN (2012) A stochastic shape and orientation model for fibres with an application to carbon nanotubes in: *Image Analysis and Stereology*, **31**:1, 17–26 (see p. 84)

KLAR, A., L. KREUSSER, and O. TSE (in preparation) Trend to equilibrium for a delay Vlasov-Fokker-Planck equation and explicit decay estimates in: *http://arxiv.org/abs/1512.01074*, 1–16 (see pp. 54, 61, 76)

KLAR, A., N. MARHEINEKE, and R. WEGENER (2009) Hierarchy of mathematical models for production processes of technical textiles in: *ZAMM Zeitschrift fur Angewandte Mathematik und Mechanik*, **89**:12, 941–961 (see pp. 3, 5, 7, 98)

KLAR, A., J. MARINGER, and R. WEGENER (2012a) A 3D Model for Fiber Lay-Down in Nonwoven Production Processes in: *Mathematical Models and Methods in Applied Sciences*, **22**:09, 1250020 (see pp. 3, 5, 15, 16, 20–22, 99)

KLAR, A., J. MARINGER, and R. WEGENER (2012b) A smooth 3D model for fiber lay-down in nonwoven production processes in: *Kinetic and Related Models*, **5**:1, 97–112 (see pp. 3, 5, 13, 23, 24, 26, 28, 101)

KLAR, A., C. NESSLER, and C. STROHMEYER (2016) Construction of virtual non-wovens in: *Progress in Industrial Mathematics at ECMI 2014* ed. by G. RUSSO, V. CAPASSO, G. NICOSIA, and V. ROMANO Springer International Publishing (see pp. 81, 115)

KLOEDEN, P. E. and E. PLATEN (1999) *Numerical Solution of Stochastic Differential Equations* Springer (see p. 35)

KOLB, M., M. SAVOV, and A. WUEBKER (2012) (Non-)Ergodicity of a degenerate diffusion modeling the fiber lay down process in: *Applied Mathematics Research eXpress*, **45**:1, 1–13 (see pp. 10, 11)

KREUSSER, L. (2015) *Particle approximation and trend to equilibrium for a delay mean-field equation*. Masters thesis Technische Universität Kaiserlautern (see pp. 54, 55, 76)

KUHLMANN, M. and C. REDENBACH (2015) Estimation of Fibre Length Distributions from Fibre Endpoints in: *Scandinavian Journal of Statistics*, **42**:4, 1010–1022 (see p. 115)

LEITHÄUSER, C. and R. FESSLER (2012) Characterizing the image space of a shape-dependent operator for a potential flow problem in: *Applied Mathematics Letters*, **25**:11, 1959–1963 (see p. 3)

LEITHÄUSER, C., R. FESSLER, and R. PINNAU (2012) An Approach to Shape Optimization with State Constraints in: *Proceedings in Applied Mathematics and Mechanics*, **12**:1, 685–686 (see p. 3)

LEITHÄUSER, C., R. PINNAU, and R. FESSLER (accepted) Approximate Controllability of Linearized Shape-Dependent Operators for Flow Problems in: *ESAIM: Control, Optimisation and Calculus of Variations*, (see p. 3)

LEVEQUE, R. J. (1992) *Numerical Methods for Conservation Laws* Birkhäuser (see p. 63)

LIU, Y. and J. WU (2014) Flocking and asymptotic velocity of the Cucker-Smale model with processing delay in: *Journal of Mathematical Analysis and Applications*, **415**:1, 53–61 (see p. 32)

MARHEINEKE, N. and R. WEGENER (2006) Fiber Dynamics in Turbulent Flows: General Modeling Framework in: *SIAM Journal on Applied Mathematics*, **66**:5, 1703–1726 (see p. 3)

MARHEINEKE, N. and R. WEGENER (2007) Fiber dynamics in turbulent flows: Specific Taylor drag in: *SIAM Journal on Applied Mathematics*, **68**:1, 1–23 (see p. 3)

MARINGER, J. (2013) *Stochastic and Deterministic Models for Fiber Lay-down*. PhD thesis Technische Universität Kaiserlautern (see pp. 5, 13, 15, 16, 22, 23, 28, 98, 99, 101)

MARINGER, J., A. KLAR, and R. WEGENER (2010) A Three-Dimensional Model for Fiber Lay-Down Processes in: *Proceedings in Applied Mathematics and Mechanics*, **10**:1, 701–702 (see pp. 3, 5)

MATLAB (2015) *Version R2015b* The MathWorks Inc. (see pp. 64, 105, 111)

MAVI (2005) *Modular Algorithms for Volume Images (MAVI)* `http://www.itwm.fraunhofer.de/en/departments/image-processing/microstructure-analysis/mavi.html` Department of Image Processing, Fraunhofer Institute for Industrial Mathematics (ITWM), Kaiserslautern, Germany (see p. 107)

MCLACHLAN, R. I. and G. R. W. QUISPEL (2002) Splitting methods in: *Acta Numerica*, **11**:2002, 341–434 (see p. 63)

NESSLER, C. H. (2013) *Interacting Fiber Equations*. Diploma thesis Technische Universität Kaiserlautern (see p. 3)

OHSER, J. and K. SCHLADITZ (2009) *3D Images of Material Structures* Wiley-VCH (see pp. 84, 107)

ØKSENDAL, B. (2003) *Stochastic Differential Equations* Springer (see pp. 7, 8, 15, 35)

PEYREGA, C., D. JEULIN, C. DELISÉE, and J. MALVESTIO (2009) 3D Morphological modelling of a random fibrous network in: *Image Analysis and Stereology*, **28**:3, 129–141 (see p. 107)

REDENBACH, C., A. RACK, K. SCHLADITZ, O. WIRJADI, and M. GODEHARDT (2012) Beyond imaging: on the quantitative analysis of tomographic volume data in: *International Journal of Materials Research (formerly Zeitschrift für Metallkunde)*, **103**:02, 217–227 (see pp. 84, 107)

REDENBACH, C., K. SCHLADITZ, I. VECCHIO, and O. WIRJADI (2014) Image analysis for microstructures based on stochastic models in: *GAMM (Gesellschaft für Angewandte Mathematik und Mechanik)-Mitteilungen*, **37**:2, 281–305 (see pp. 84, 107)

REDENBACH, C. and I. VECCHIO (2011) Statistical analysis and stochastic modelling of fibre composites in: *Composites Science and Technology*, **71**:2, 107–112 (see pp. 84, 107)

RISKEN, H. (1996) *The Fokker-Planck Equation* 2nd edition Springer (see p. 8)

SCHLADITZ, K., S. PETERS, D. REINEL-BITZER, A. WIEGMANN, and J. OHSER (2006) Design of acoustic trim based on geometric modeling and flow simulation for non-woven in: *Computational Materials Science*, **38**:1, 56–66 (see pp. 84, 107, 115)

SMITH, H. (1987) Monotone semiflows generated by functional differential equations in: *Journal of Differential Equations*, **66**:3, 420–442 (see p. 61)

SPOHN, H. (1991) *Large scale dynamics of interacting particles* Springer (see p. 49)

STILGENBAUER, P. (2014) *The Stochastic Analysis of Fiber Lay-Down Models*. PhD thesis Technische Universität Kaiserslautern (see pp. 15, 16)

STRANG, G. (1968) On the construction and comparison of difference schemes in: *SIAM Journal on Numerical Analysis*, **5**:3, 506–517 (see p. 63)

STROHMEYER, C. and G. LEUGERING (2016) Effective Mechanical Properties of Nonwovens Produced by Airlay Processes in: *Progress in Industrial Mathematics at ECMI 2014* ed. by G. RUSSO, V. CAPASSO, G. NICOSIA, and V. ROMANO Springer International Publishing (see pp. 83, 115)

SUN, Y., W. LIN, and R. ERBAN (2014) Time delay can facilitate coherence in self-driven interacting-particle systems in: *Physical Review E - Statistical, Nonlinear, and Soft Matter Physics*, **90**:6, 062708 (see p. 32)

TALBOT, H., T. LEE, D. JEULIN, D. HANTON, and L. W. HOBBS (2000) Image analysis of insulation mineral fibres in: *Journal of Microscopy*, **200**:3, 251–268 (see p. 114)

TAYLOR-KING, J. P., B. FRANZ, C. A. YATES, and R. ERBAN (2015) Mathematical modelling of turning delays in swarm robotics in: *IMA Journal of Applied Mathematics (Institute of Mathematics and Its Applications)*, **80**:5, 1454–1474 (see p. 32)

VECCHIO, I. (2014) *Image based characterization and geometric modeling of 3d materials microstructures*. PhD thesis Technische Universität Kaiserslautern (see pp. 84, 107)

VILLANI, C. (2003) *Topics in Optimal Transportation (Graduate Studies in Mathematics, Vol. 58)* American Mathematical Society (see p. 55)

Akademischer Lebenslauf

Name: Christian Helmut Neßler

2013 — 2017   Doktorand in Technomathematik, Fachbereich Mathematik, Technische Universität Kaiserslautern, Deutschland.

2008 — 2013   Diplom in Technomathematik, Fachbereich Mathematik, Technische Universität Kaiserslautern, Deutschland; Nebenfächer: Physik und Informatik.

- Diplomarbeit „Interacting Fiber Equations".
- Auslandsaufenthalt als Erasmus–Student, Università degli Studi di Firenze, Florenz, Italien.

1999 — 2008   Abitur am Hugo–Ball Gymnasium, Pirmasens, Deutschland.

Academic curriculum vitae

Name: Christian Helmut Neßler

2013 — 2017   Doctoral studies in Technomathematics at the Department of Mathematics, University of Kaiserslautern, Germany.

2008 — 2013   Diploma in Technomathematics at the University of Kaiserslautern, Germany; second subjects: physics and computer science.

- Diploma Thesis "Interacting Fiber Equations".
- Semester abroad as an Erasmus exchange student at Università degli Studi di Firenze, Florence, Italy.

1999 — 2008   Abitur at Hugo–Ball Gymnasium, Pirmasens, Germany.